Evidence for πK-atoms with DIRAC-II

Dissertation

zur

Erlangung der naturwissenschaftlichen Doktorwürde
(Dr. sc. nat.)

vorgelegt der

Mathematisch-naturwissenschaftlichen Fakultät

der

Universität Zürich

von

Yves Allkofer

aus

Ergisch, VS

Promotionskomitee

Prof. Dr. C. Amsler (Vorsitz)
Dr. S. Horikawa
Dr. C. Regenfus

Zürich, 2008

Zusammenfassung

DIRAC-II ist ein Fixtarget-Experiment am Proton-Synchrotron (PS) des CERN, das zum Ziel hat πK-Atome, elektromagnetisch gebundene Zustände aus $\pi^{\pm}K^{\mp}$-Paaren, zu entdecken und ihre Lebensdauer zu messen. Diese Atome wurden in den beiden Spektrometerarmen des Experiments als kleiner Überschuss von $\pi^{\pm}K^{\mp}$ Ereignissen mit sehr kleinen Relativimpulsen gemessen. Genauer betrachtet entsteht dieser Überschuss durch das Aufbrechen von πK-Atomen noch innerhalb der dünnen Targetfolie, kurz nach ihrer dortigen Produktion. Die gemessene Anzahl der Atome lässt auf ihre Lebensdauer schliessen, woraus man wiederum die Kombination der πK S-Wellen Streulängen $|a_{1/2} - a_{3/2}|$ (für Isospin $1/2$ und $3/2$) bestimmen kann. Hierbei will das DIRAC-II Experiment eine Genauigkeit von 10% erreichen.

Das ursprüngliche DIRAC Experiment war für die Messung der Streulängen von $\pi\pi$-Atomen konstruiert. Bisher wurden 15 000 Atome identifiziert, die zu einer Messpräzision von 5% für den Wert von $|a_0 - a_2|$ führen.

Niederenergetisch stark wechselwirkende Teilchen können mittels der so genannten Chiralen Störungstheorie (ChPT) beschrieben werden, die es auch erlaubt diese Streulängenkombinationen auszurechnen. Die Streulängen von $\pi\pi$-Atomen, $|a_0 - a_2|$, wurden mit einer Genauigkeit von 2% berechnet wobei man eine sehr gute Übereinstimmung von Theorie und Experiment findet, motivierend für die Theoretiker das Model auf das s-Quark zu erweitern und eine Berechnung der πK-Streulängenkombination durchzuführten. Die Messung dieser Grösse durch das DIRAC-II Experiment stellt hierbei die einzige modellfreie Methode da. Bestehende Messungen dieser Streulängenkombination stammen aus Streuexperimenten der 70'er Jahre, welche intrinsisch grossen Fehlern durch ihre Modellabhängigkeit unterlagen. πK-Atome wurden bisher noch nicht beobachtet.

Das Thema der vorliegenden Arbeit war die Entwicklung und Konstruktion eines Aerogel Čerenkov Zähler zur Identifikationen von Kaonen und Protonen im Impulsbereich zwischen 4 und 8 GeV/c. Eine gute Teilchenerkennung ist entscheidend für die Entdeckung von πK-Atomen. Wegen des relativ grossen Impulsbereichs musste Aerogel mit zwei verschiedenen Brechungsindizen verwendet werden, nämlich $n = 1.008$ und $n = 1.015$. Wegen der kleinen Lichtausbeute und der kurzwelligen Natur der Čerenkov Strahlung, die stark den Absorptionseffekten im Aerogelmaterial unterliegt, wurde das Design der Lichtauslese sorgfältig optimiert, u.a. durch die Verwendung von Wellenlängenschiebern.

Die zweite Hälfte der vorliegenden Arbeit beschreibt die Analyse der Daten,

die in 2007 unter Verwendung dieses Čerenkov Zählers genommen wurden. Hauptsächlich wird hier die Suche nach den bisher noch unentdeckten πK-Atomen beschrieben. Dafür war eine neue Methode der Spurrekonstruktion vonöten, da nur Detektoren nach dem Spektrometermagneten benutzt werden konnten. Diese Methode wurde auch an den gut erforschten 2001 Daten getestet. Eine neue Monte-Carlo-Beschreibung des Experiments ist ebenfalls Teil dieser Arbeit.

Aus der Anzahl von 1137 ± 257 entdeckten Coulomb-Paaren im Signalbereich erwartet man, dass auch πK-Atome produziert wurden. Trotz der kleinen Statistik, konnten 173 ± 54 πK-Atome in den 2007 Daten nachgewiesen werden, entsprechend einem Signal von 3.2 σ. Diese Zahl stimmt sehr gut mit der erwarteten überein. Damit wurde eine Untergrenze der Lebensdauer von πK-Atomen von 1.5 fs ermittelt bei einem Vertrauensniveau von 84.1%.

Abstract

DIRAC-II is a fixed-target experiment at the CERN Proton Synchroton (PS) which has been designed to search for πK-atoms, a bound state of a $\pi^{\pm}K^{\mp}$ pair, and measure their lifetime. These atoms are observed through an excess of low energetic $\pi^{\pm}K^{\mp}$-pairs over the background, detected in the two spectrometer arms. This excess comes from the ionization of πK-atoms in the target and can be related to their mean life. The πK S-wave scattering length combination $|a_{1/2} - a_{3/2}|$ (for isospin $1/2$ and $3/2$) can be related to the latter. The aim of the upgraded DIRAC-II experiment is a measurement of the scattering length combination $|a_{1/2} - a_{3/2}|$ with a precision of 5%. πK-atoms have not been observed so far.

The original DIRAC experiment was designed to measure the scattering lengths of $\pi\pi$-atoms. So far, close to 15 000 atoms have been detected, leading to a precision on $|a_0 - a_2|$ which is better than 10%.

In chiral perturbation theories (ChPT) the $\pi\pi$-scattering lengths have been calculated with 2% precision and are in good agreement with the DIRAC-II measurements. Predictions for the πK ones, which involve the s-quarks are obtained. DIRAC-II data will be very important to check ChPT extended to the s-quark. Previous measurements of $a_{1/2}$ and $a_{3/2}$ suffer from very large errors as they are extrapolated from high energy πK-scattering.

My first contribution was the development and construction of a Čerenkov threshold counter for the separation of kaons from pions, which is crucial for the detection of πK-atoms. The momentum range (4-8 GeV/c) requires aerogel with refractive index $n = 1.008$ and $n = 1.015$ as Čerenkov radiator. Because of the strong light absorption in aerogel, the low indices and the very large size of the active area needed in the DIRAC-II experiment, new designs had to be invented and investigated. In this work new concepts of aerogel counters are presented e.g. introducing wavelength shifters in order to avoid the strong light absorption in aerogel.

The second contribution was the analysis of the first run in 2007 and the search for πK-atoms. A new tracking had to be developed to optimize the reconstruction of tracks using only detectors downstream of the spectrometer magnet, since no upstream detectors were operational at that time. This new method was carefully tested on the already published $\pi\pi$ 2001 data sample.

From the 1137 ± 257 observed πK Coulomb pairs in the signal region where atoms are expected, one predicts that πK-atoms must have been produced. Despite the low statistic collected during the first data run in 2007, we have already evidence for 173 ± 54 πK-atoms with a significance of 3.2 σ, which is in good agreement with

expectation from the number of observed Coulomb-pairs. A lower limit of 1.5 fs could be given for their mean life at 84.1% confidence level.

Acknowledgments

I gratefully acknowledge the support and help I received from the University of Zurich group of Prof. C Amsler: I. Johnson and S. Horikawa for their collaboration on the development of the aerogel Čerenkov detector, J. Rochet for the technical realization, C. Regenfus for his help in hardware and statistics and all the others for the great working atmosphere. Special thanks go to my adviser Prof. C. Amsler for his permanent support, the interesting discussions on the blackboard and the vast amount of knowledge received during my thesis.

I also benefited significantly from the guidance of the DIRAC-II collaboration, specially A. Benelli, L. Tauscher, L. Nemenov, A. Kuptsov, V. Yazkov and M. Zhabitsky.

And last but not least, I received an important support from my family and from my girlfriend Cindy.

To Ludivine

Contents

Zusammenfassung **i**

Abstract **iii**

Acknowledgments **v**

Summary **1**

1 Theoretical background **3**
1.1 Introduction 3
1.2 Productions in proton-target interactions and the k-factor 5
1.3 Evolution of πK-atoms inside the target 8

2 Experimental setup **12**
2.1 DIRAC-II spectrometer: generalities 12
2.2 Upstream detectors 14
2.2.1 Micro drift chambers 14
2.2.2 Scintillating fiber detector 15
2.2.3 Ionization hodoscope 15
2.3 Downstream detectors 16
2.3.1 Drift chambers 16
2.3.2 Vertical and horizontal hodoscopes 17
2.3.3 Čerenkov counters 19
2.3.4 Preshower detector 22
2.3.5 Muon detector 22
2.4 The trigger 23
2.5 The software 24

3 The aerogel Čerenkov counter **26**
3.1 History and properties of Čerenkov radiation 26
3.2 Aerogel 29
3.2.1 Production 29
3.2.2 Properties of the aerogel 30
3.2.3 Measurement of the refractive index 31

3.3 Cosmic ray test setup . . . 32
3.4 Direct and diffusion box design . . . 35
3.5 Detailed study of the dimensions and of the refractive index . . . 39
3.6 The photomultipliers . . . 43
3.7 New designs . . . 45
3.7.1 Pyramid design . . . 45
3.7.2 Sandwich design . . . 47
3.8 Assembly of the final design . . . 49

4 Performance of the aerogel Čerenkov detector 53
4.1 Test with cosmic rays . . . 53
4.2 Test with beam . . . 55
4.3 The 2007 DIRAC-II run . . . 56
4.3.1 Calibration using electron-trigger . . . 56
4.3.2 Pion-trigger . . . 58
4.3.3 Minimum bias trigger . . . 59
4.3.4 Mixed trigger . . . 61
4.4 TDC analysis . . . 64
4.5 Digitization of the detector response . . . 66

5 Data analysis: Search for $\pi\pi$-atoms 68
5.1 Downstream tracking . . . 68
5.1.1 Procedure . . . 68
5.1.2 Quality of the downstream tracking . . . 70
5.2 Signal extraction . . . 73
5.2.1 Overview . . . 73
5.2.2 Event selection . . . 74
5.2.3 Fit function and background description . . . 75
5.3 Measurement of the mean life of $\pi\pi$-atoms . . . 81
5.4 Analysis of the 2007 data sample . . . 83

6 Data analysis: Search for πK-atoms 86
6.1 Kinematics of πK-atoms . . . 86
6.2 Event selection . . . 87
6.3 $\pi^- K^+$ analysis . . . 88
6.3.1 Overview . . . 88
6.3.2 Monte-Carlo simulation and k^{exp} measurement . . . 88
6.3.3 Background description . . . 92
6.3.4 Detection of Coulomb-pairs . . . 95
6.3.5 Fit function and results . . . 95
6.4 $\pi^+ K^-$ analysis . . . 98
6.5 $\pi^- K^+ + \pi^+ K^-$ analysis and mean life measurement . . . 100

Conclusions 102

A Theoretical background **104**
A.1 Theory of scattering 104
A.2 Scattering length a 105
A.3 Transition probability and cross section 106
A.4 $|U|^2$ and the Born approximation 108
A.5 πK-atoms 109
A.6 Isospin 109

B PM specifications **111**

C Mechanical structure of the aerogel Čerenkov counter **113**

Summary

The aim of the DIRAC experiment was the detection of $\pi\pi$-atoms and the measurement of their mean life which is related to the S-wave scattering length difference $|a_2 - a_0|$ (for isospin 2 and 0, respectively). The scattering length is a physical quantity which can be predicted with a precision of 2% in the framework of chiral perturbation theory (ChPT), an effective theory based on QCD below the chiral symmetry breaking scale. The measurement of the mean life is a model independent way to crosscheck ChPT. A first measurement has been published in [1] and is in good agreement with theory [2]. These results were the motivation for an upgrade of the spectrometer [3] in order to improve the collection efficiency, to reduce the background and to measure simultaneously the mean life of $\pi\pi$-atoms within a precision better than 6% (or 3% on the scattering length) and the mean life of πK-atoms with a precision at the level of 20% (or 10% on the scattering length). The topic of this thesis is the detection of πK-atoms, which have not been observed so far; details on $\pi\pi$-atoms have been discussed elsewhere [1] [4] [5].

However, in the experimental area a 24 GeV/c proton beam from the PS accelerator at CERN interacts with a thin target. Among other particles pions and kaons are produced from proton-nuclei interactions, partly through short- or long-lived intermediate states. Direct πK-pairs or from short-lived resonances can have a Coulomb interaction in the final state. While most of them are unbound (Coulomb-pairs), some of them create a bound state (πK-atoms). Long-lived intermediate states create time-correlated pairs without Coulomb interaction because the pion and the kaon are too far from one another. Accidentals-pairs are produced from two incident protons leading to time uncorrelated πK-pairs. In chapter 1 the production cross section of the different types of pairs are discussed as well as the evolution of πK-atoms inside the target. A fraction of the πK-atoms annihilate into $\pi^0 K^{0}_{(-)}$ and another fraction interacts with the target; either they are excited to a higher bound state or they are ionized (breakup) into pairs of oppositely charged particles ($\pi^{\pm} K^{\mp}$) with low relative momentum. The total number of produced atoms and the number of ionized ones give the breakup probability P_{br} which can then be related to their mean life.

To detect $\pi^{\pm} K^{\mp}$ and hence to measure the mean life, several detectors had to be upgraded and some new detectors had to be installed for the identification of kaons: a heavy gas Čerenkov threshold counter for pion-kaon separation and an aerogel

Čerenkov threshold counter for kaon-proton separation. The upgraded DIRAC-II spectrometer is discussed in chapter 2.

The design and construction of the aerogel Čerenkov counter is one of the main topics of this work and is described in chapter 3. The DIRAC-II experiment requires very low indices of refraction in the order of $n = 1.01$. The number of Čerenkov photons produced in a radiator is proportional to $(1 - 1/n^2)$ and is hence very low. Furthermore, the distance between the photomultipliers has to be very large (around half a meter) to cover the whole kaon spatial distribution. Because of the short absorption length in aerogel, the probability to detect the UV photons is dramatically reduced. To fulfill these requirements new designs had to be developed. In this work a new design is presented using pyramidical structures for the radiator, and wavelength shifters to avoid absorption which is much stronger for short wavelengths.

After the construction and installation in the spectrometer, the performances of the aerogel detector were tested (chapter 5). Much effort was invested to disentangle the kaon from the proton response in order to estimate their distributions and identification efficiencies.

Finally, first beam data could be taken in summer-autumn 2007 with this detector. Only detectors downstream of the spectrometer magnet were operational at that time. For the search of πK-atoms, a new tracking method optimizing the track reconstruction without upstream detectors was therefore written. This method has been tested and trained with the well known 2001 data sample extracting $\pi\pi$-atoms. Chapter 5 explains all details and leads to the detection of 12 000 $\pi\pi$-atoms. The main difficulties with the "downstream only" tracking are multiple scattering affecting especially in the transverse plane. Thus, for the 2007 πK-analysis, only the longitudinal components have been used. Finally chapter 6 describes this analysis which results in the first observation of 143 ± 53 $\pi^- K^+$- and 29 ± 15 $\pi^+ K^-$-atoms.

The development of the aerogel counters was published in ref. [6][7][8] and the πK data analysis presented at the International Conference on Exotic Atoms (EXA08).

Chapter 1

Theoretical background

1.1 Introduction

Quantum Chromodynamics (QCD) describes strong interactions at high and low energies. At high energy the interactions of quarks and gluons become weak and can be treated as a perturbation. At low energy, QCD perturbation theory cannot be used anymore, but an effective field theory has been developed. This theory introduced an effective Lagrangian split into a Chiral symmetric term and an explicitly chiral symmetry breaking term. In the framework of the 2-flavor (including the u and d quark) chiral perturbation theory (ChPT) [9] precise prediction on the low energy hadronic processes can be obtained. The S-wave $\pi\pi$-scattering lengths a_0 and a_2 (for isospin $I = 0$ respectively $I = 2$) have been calculated [2]:

$$a_0 = 0.220 \pm 0.005\ m_{\pi^+}^{-1},\quad a_2 = 0.0444 \pm 0.0010\ m_{\pi^+}^{-1},\quad a_0 - a_2 = 0.265 \pm 0.004\ m_{\pi^+}^{-1}. \tag{1.1}$$

The first observation of 270 ± 50 $\pi\pi$-atoms has been achieved at the U-70 synchrotron of Serpukhov [10]. These atoms decay mainly[1] (99.6%) into uncharged pions. The decay width $\Gamma_{n=1,\ell=0}$ of this channel and therefore the mean life of these atoms in the 1S-state[2] $\tau_{n=1,\ell=0}$ can be written as a function of the $\pi\pi$-scattering length difference $a_0 - a_2$ [12]:

$$\Gamma_{1S}(\pi^{\pm}\pi^{\mp} \to \pi^0\pi^0) = \frac{1}{\tau_{1S}} = \frac{2}{9}\alpha^3 p^* |a_0 - a_2|^2 (1 + \delta_\Gamma), \tag{1.2}$$

with $\delta_\Gamma = (5.8 \pm 1.2) \times 10^{-2}$ a correction term, p^* the momentum of the outgoing π^0 in the $\pi\pi$-atomic system and $\alpha = 1/137$ the fine structure constant. A first

[1] The decay channel into two photons ($\approx 0.3\%$) is neglected here [11].

[2] "1" stands for quantum number $n = 1$ and "S" ("P") for $\ell = 0$ ($\ell = 1$) respectively. Atoms in the P-state cannot decay into two pions due to the conservation of the angular momentum and the decay into an uncharged pion and a photon is strongly suppressed. For quantum number n exits the following relation: $\tau_n = \tau_1 \cdot n^3$.

measurement of the mean life and hence the $\pi\pi$-scattering length difference has been published by DIRAC [1] and is in good agreement with ChPT:

$$\tau_{1S}(\pi\pi) = 2.91^{+0.49}_{-0.62} \cdot 10^{-15}\text{s}; \quad \text{a}_0 - \text{a}_2 = 0.264^{+0.033}_{-0.020}\ \text{m}^{-1}_{\pi^+}. \tag{1.3}$$

Following the success of the 2-flavor ChPT, the s-quark was introduced leading to the 3-flavor chiral perturbation theory. This theory makes predictions on the πK-scattering lengths $a_{1/2}$ and $a_{3/2}$ (for isospin $I = 1/2$ respectively $I = 3/2$). In next-to-leading order calculations the following values are obtained [13]:

$$a_{1/2} = 0.19 \pm 0.02\ m^{-1}_{\pi^+}; \quad a_{3/2} = -0.05 \pm 0.02\ m^{-1}_{\pi^+}. \tag{1.4}$$

Alternatively, a new approach based on dispersion relation [14] gives some prediction on the πK-scattering lengths and leads to the scattering length difference of

$$a_{1/2} - a_{3/2} = 0.269 \pm 0.015\ m^{-1}_{\pi^+}. \tag{1.5}$$

Similarly to $\pi\pi$-atoms, πK-atoms ($A_{\pi^\pm K^\mp}$) are decaying dominantly as follows:

$$A_{\pi^- K^+} \rightarrow \pi^0 K^0, \tag{1.6}$$
$$A_{\pi^+ K^-} \rightarrow \pi^0 \bar{K}^0. \tag{1.7}$$

Therefore one can relate the mean life of πK-atoms in the 1S-state to the width Γ_{1S} and to the πK-scattering lengths (for a derivation based only on quantum mechanics see Appendix A and for a more precise study based on ChPT at the next-to-leading order see [15]):

$$\Gamma_{1S}(\pi^\pm K^\mp \rightarrow \pi^0 \overset{(-)}{K^0}) = \frac{1}{\tau_{1S}} = \frac{8}{9} p^* \mu^2 \alpha^3 |a_{1/2} - a_{3/2}|^2 (1 + \delta_\Gamma), \tag{1.8}$$

with the correction term $\delta_\Gamma = 0.040 \pm 0.022$, $\mu = \frac{M_\pi M_K}{M_\pi + M_K}$ and $p^* = 11.252$ MeV/c the momentum of the outgoing π^0 or $\overset{(-)}{K^0}$ in the πK-atomic system. The mean life in the 1S-wave τ_{1S} has been predicted to be $\tau_{1S} = 3.7 \pm 0.4$ fs [15]. DIRAC-II aims to measure this mean life of πK-atoms with a precision of 20% leading to a 10% measurement for the scattering lengths difference.

More difficult, is the measurement of the atomic level shift ΔE_n induced by the strong interactions and by the electromagnetic vacuum polarization effects leading to a splitting of the energy levels and therefore to a difference ΔE_{ns-np} of the energy levels ns and np. The electromagnetic part is well known from QED and the strong interacting shift is proportional to $2a_{1/2} + a_{3/2}$ [15]. Measuring simultaneously, the energy shift ΔE_{ns-np} and the width Γ_{1S} enables the extraction of $a_{1/2}$ and $a_{3/2}$ separately.

It has been proposed in [16] to take advantage of the Stark effect using an external magnetic field in order to measure the ΔE_{ns-np}. Furthermore, for $n = 2$ calculations have been performed [15] leading to $\Delta E_{2s-2p} = -1.4 \pm 0.1$ eV.

However, in the past many experiments have been performed to study the πK-scattering amplitude. Especially, the inelastic scattering of kaons on protons or neutrons was analyzed. The differential cross section can be related to the scattering amplitude and to the phase shift, see Appendix A. The most reliable data are for a mass $m(\pi K)$ above the chiral symmetry breaking scale (≈ 1 GeV/c). It is difficult to extrapolate these results to lower energies and to determine the scattering lengths. A complete list of the experiments and results are given in [3] and for some of them the results are shown in table 1.1 and 1.2. Inconsistencies are evident. The results are not compatible between theory and experiment. What makes this enterprise particularly exciting is that by measuring the mean life with the DIRAC-II spectrometer, it is possible to measure the scattering lengths in a model independent way and to clarify the situation.

reference	[17]	[18]	[19]	[20]
$a_{1/2}$	0.168	0.220 ± 0.035	0.280 ± 0.056	0.335 ± 0.006

Table 1.1: Measured S-wave πK-scattering length for isospin $I = 1/2$ in units of $m_{\pi^+}^{-1}$.

reference	[21]	[22]	[23]	[24]	[25]	[20]
$a_{3/2}$	-0.085	-0.092	-0.078	0.096	-0.072	-0.14 ± 0.07

Table 1.2: Measured S-wave πK-scattering length for isospin $I = 3/2$ in units of $m_{\pi^+}^{-1}$.

Furthermore, a low mass enhancement has been observed recently in the πK invariant mass spectrum corresponding to a very broad scalar resonance around 850 MeV/c called $K_0^*(800)$ or κ. The $\bar{K}^*(892)^0 K^+\pi^- \to K^+K^-\pi^+\pi^-$ channel has been studied [26]. The desintegration of the D meson into $K^-\pi^+\pi^+$ and $K^-\pi^+\mu^+\nu$ has been analyzed [27] [28]. These experiments and many others [29] have reported evidence for this resonance. However, the existence of the κ remains controversial [30].

It has been suggested that the κ is a 4-quark states [31] similarly to the σ, $a_0(980)$ and $f_0(980)$ mesons. However, each resonance, provided that the width is large enough, influences the phase shift in the scattering amplitude and therefore the scattering lengths. Measuring the latter could help to answer the questions about this hot topic which is the κ resonance.

1.2 Productions in proton-target interactions and the k-factor

In the DIRAC-II experiment a proton beam interacts with a target. Four different production mechanisms are important for the πK-analysis. Their diagrams are shown in fig. 1.1 and a short description is given in table 1.3.

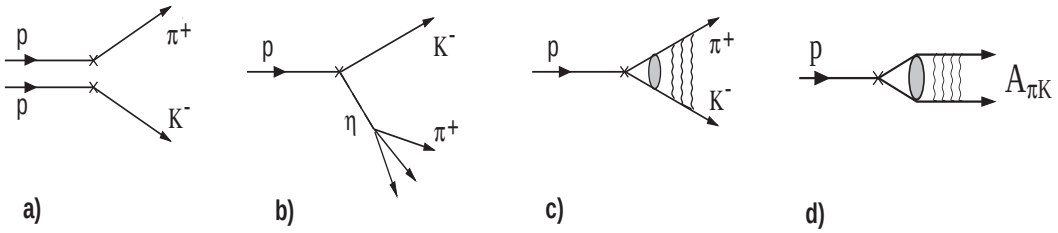

Figure 1.1: Diagram of the production of πK-pairs: a) accidental-pairs from two protons, b) non-Coulomb-pairs from a long-lived intermediate state like the η-meson, c) Coulomb-pairs from direct production or short-lived intermediate states and d) πK-atoms.

Type of πK pair	Description
Accidental-pairs, N^{acc}	Uncorrelated particles from two different protons crossing the target at the same moment
non-Coulomb pair, N^{nC}	From long-lived sources (η, K^0, ...) without any interaction between the two particles of the pair
Coulomb pair, N^{C}	From direct production or short-lived intermediate resonances (ω, ρ, ...) and in a final unbound state
πK-atoms, N^{A}	From direct production or short-lived intermediate resonances (ω, ρ, ...) and in a final bound state

Table 1.3: The various possible πK-pairs and their observed numbers N.

Pion and kaons from direct production or from short-lived intermediate states (Coulomb-pairs (fig. 1.1c) and atoms (fig. 1.1d)) which are close in space to each other interact electromagnetically in the final state, while decays of long-lived intermediate states (non-Coulomb-pairs (fig. 1.1b)) lead to pairs that are too far to have any interaction in the final state.

The yield of non-Coulomb-pairs is described by the double inclusive cross section [32]:

$$\frac{d\sigma^0}{d\vec{p}_\pi d\vec{p}_K} \equiv \frac{1}{\sigma_{in}} \frac{d\sigma}{d\vec{p}_\pi} \frac{d\sigma}{d\vec{p}_K} R(\vec{p}_\pi \vec{p}_K), \tag{1.9}$$

where the suffix 0 means that Coulomb interaction in the final state has been ignored. Here σ_{in} is the inelastic cross section for hadron production, R the correlation function due to the strong interaction and p_π (p_K) are the momentum of the pion (kaon) in the laboratory system. $d\sigma/dp_\pi$ and $d\sigma/dp_K$ are their inclusive production cross sections. Accidental-pairs are produced from two protons and hence are not correlated $R \equiv 1$. The corresponding cross section is:

$$\frac{1}{\sigma_{in}} \frac{d\sigma}{d\vec{p}_\pi} \frac{d\sigma}{d\vec{p}_K}. \tag{1.10}$$

An important step has been achieved [33], relating the production cross sec-

tion for πK-atoms to the double inclusive cross section $\frac{d\sigma^0}{d\vec{p}_\pi d\vec{p}_K}$ without Coulomb interactions in the final state.

$$\frac{d\sigma_n^A}{d\vec{p}_A} = (2\pi)^3 \frac{E_A}{M_A} |\Psi_n(0)|^2 \frac{d\sigma^0}{d\vec{p}_1 d\vec{p}_2}\bigg|_{\vec{p}_1 \approx \frac{M_\pi}{M_A}\vec{p}_A;\ \vec{p}_2 \approx \frac{M_K}{M_A}\vec{p}_A}, \tag{1.11}$$

where $\vec{p}_A$, E_A and M_A are the momentum, energy and mass of the atom in the laboratory system. The strong interaction in the final state is neglected and the Coulomb interaction is described by $|\Psi_n(0)|^2 = p_B^3/\pi n^3$ the square of the Bohr atomic S-wave function calculated at the origin where p_B is the Bohr momentum defined as the inverse of the Bohr radius.[3]

Coulomb-pairs and πK-atoms have the same production mechanism and hence the analogue of equ.(1.11) for Coulomb-pairs which are not bound states is given by [34],

$$\frac{d\sigma^C}{d\vec{P}d\vec{Q}} = (2\pi)^3 \frac{E_A}{M_A} |\Psi_{\vec{Q}}^{(+)}(0)|^2 \frac{d\sigma^0}{d\vec{p}_1 d\vec{p}_2}\bigg|_{\vec{p}_1 \approx \frac{M_\pi}{M_A}\vec{p}_A;\vec{p}_2 \approx \frac{M_K}{M_A}\vec{p}_A}, \tag{1.12}$$

where $\vec{P}$ is the total momentum, $\vec{Q}$ the relative momentum, $\Psi_{\vec{Q}}^{(+)}$ is a continuous set of solutions which are asymptotically free plane wave functions with relative momentum $\vec{Q}$. These wave functions are sometimes called Sommerfeld wave functions.

Dividing equ.(1.11) by (1.12) and summing up the different wave functions in phase space Ω, we obtain a constant k^{th} so-called *theoretical k-factor* relating the yield of atoms to the rate of Coulomb-pairs:

$$k^{th} = \frac{N^A}{N^{\mathrm{C}}(\vec{Q} \in \Omega)} = \frac{\sum_n \frac{d\sigma_n^A}{d\vec{P}}}{\int_{\vec{Q}\in\Omega} \frac{d\sigma^C}{d\vec{P}d\vec{Q}} d\vec{Q}} = \frac{\sum_n |\Psi_n(0)|^2}{\int_{\vec{Q}\in\Omega} |\Psi_{\vec{Q}}^{(0)}|^2 d\vec{Q}} \tag{1.13}$$

The theoretical k-factor has been calculated [35] [36] for $\Omega = \{Q < 4 \cdot p_B\}$ where the reconstruction efficiency of Coulomb and atomic-pairs is the same with the DIRAC-II setup. One obtains the following relation:

$$k^{th} = \frac{N^A}{N^{\mathrm{C}}(\vec{Q} \in \Omega)} = 0.615. \tag{1.14}$$

Therefore, by measuring the number N^C of produced Coulomb-pairs, we obtain the number produced atoms N^A according to equ.(1.14).

[3] The cross section $\frac{d\sigma_n^A}{d\vec{p}_A}$ does not depend on quantum number ℓ since $\Psi_n(0)$ is set to 0 for $\ell \neq 0$. The atoms are produced only in the S-state.

1.3 Evolution of πK-atoms inside the target

After production, the πK-atoms are moving inside the target interacting with ordinary target atoms. The πK-atoms are mainly interacting through the electric field of the target atoms and hence the strong cross sections are neglected. Also the Coulomb interactions with the atomic shell electrons from the target are negligible. Therefore only electromagnetic interactions between the πK-atoms and the target nuclei are relevant. The latter interactions have been described for $\pi\pi$-atoms in a 94, 98 μm Ni-target using the one-photon exchange Born approximation and the Glauber approximation taken into account multi-photon exchanges [38] [37]. However, so far only the Born approximation is available for the calculations of interaction between πK-atoms and the target nuclei of the 28 μm Pt-target used in 2007.

Three different evolutions inside the target are possible: annihilation, (de)-excitation and breakup (ionization). DIRAC-II detects charged $\pi^{\pm}K^{\mp}$-pairs and hence is only sensitive to the latter contribution: the breakup pairs or so-called *atomic-pairs*. These pairs have the advantage that they exhibit some specific kinematical features which allow to identify them experimentally [33], namely very low relative momentum at production in the center of mass system of the atom (fig. 1.2). The πK distributions are wider than the $\pi\pi$ ones due to higher Bohr momenta. After breakup the pairs are affected by multiple scattering while traveling through the target, especially in the transverse plane. The longitudinal component Q_L remains almost unchanged. Fig. 1.3 shows an estimation of the atomic-pairs Q (a) and Q_L (b) distributions after track reconstruction.

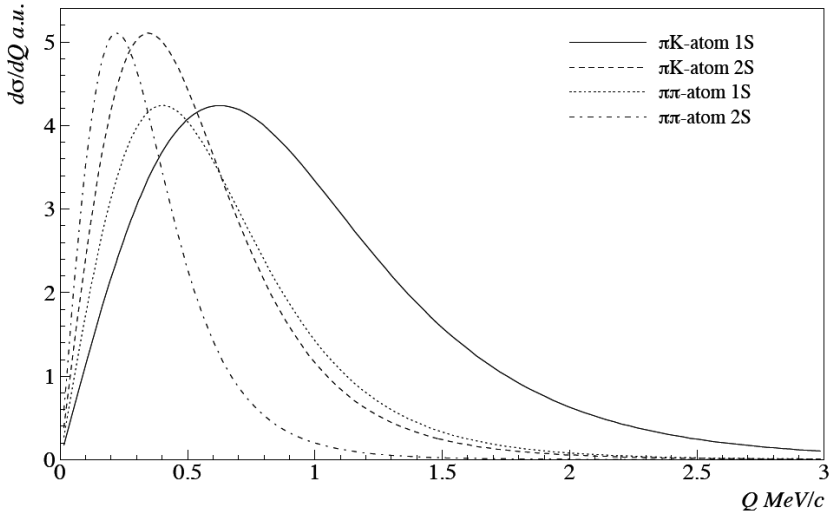

Figure 1.2: Relative momentum distribution for breakup-pairs from $\pi\pi$- and πK-atoms in their rest frame being initially in a 1S and 2S-states [3].

Since the only possible evolution scenarios are annihilation, (de)-excitation and

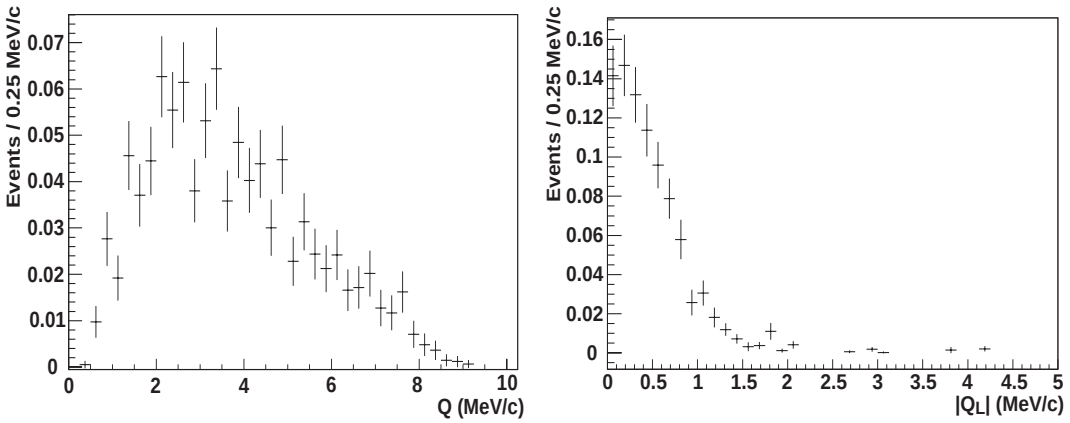

(a) (b)

Figure 1.3: Simulated relative momentum distribution Q (a) and its longitudinal projection along the beam axis Q_L (b) for breakup pairs from πK-atoms after track reconstruction. Multiple scattering, acceptance and inefficiencies of the DIRAC-II setup are taking into account.

breakup, one obtains for the breakup probability $P_{\rm br}$:

$$P_{\rm br} = 1 - P_{\rm anh} - P_{\rm (de)-exc}, \tag{1.15}$$

where $P_{\rm (de)-exc}$ is the (de)-excitation probability and $P_{\rm anh}$ the annihilation probability. Moreover, by definition of the breakup probability one obtains

$$P_{\rm br} = \frac{n^A}{N^A}, \tag{1.16}$$

where n^A is the number of atomic-pairs. This relation is used to determine experimentally the breakup probability. In order to illustrate that the latter depends on the mean life τ_{nS} of the atom, one can write:

$$P_{\rm anh} = \frac{1}{\lambda_n^{\rm anh}} = \frac{1}{\beta \cdot \tau_{nS}} \tag{1.17}$$

where $\lambda_n^{\rm anh}$ is the mean free path before annihilation, β the velocity of the atom and τ_{nS} the mean life of the atom in the state n. Since only S-wave atoms are decaying for $\ell \neq 0$ the annihilation probability is set to 0. Joining equ.(1.15) and (1.17) one obtains a relation between the mean life of πK-atoms and the breakup probability.

Details on the numerical calculations of the breakup probability and its accuracy are given in [38]. Fig. 1.4 shows the obtained function for different thicknesses of the target and different nucleus charges. For the calculations an average momentum for the πK-atoms of 6.5 GeV/c has been assumed. One concludes that for the observation of πK-atoms, where the number of atomic-pairs and hence the breakup probability has to be optimized, the most suitable target is made of platinum ($Z =$

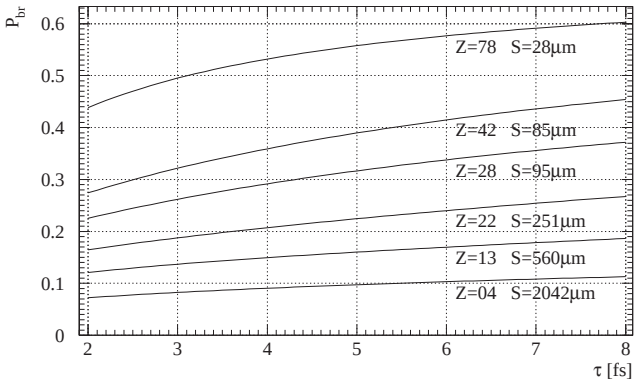

Figure 1.4: Breakup probability (P_{br}) as a function of the mean life for different target thicknesses S and nucleus charges Z.

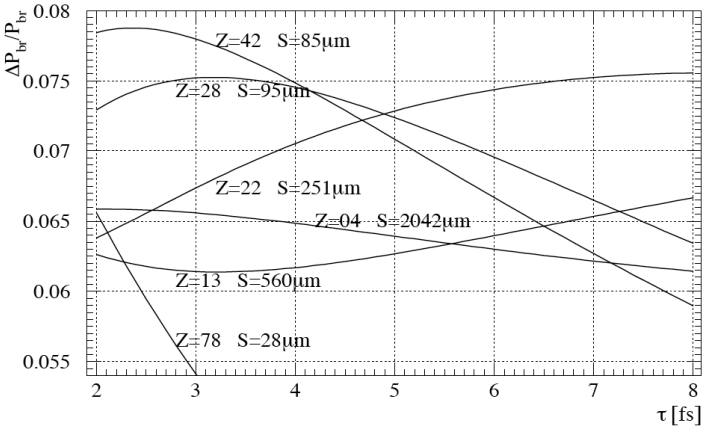

Figure 1.5: Relative accuracy on the breakup probability required to obtain a mean life measurement on πK-atoms with a precision of 20%, as a function of mean life for different targets.

78). Therefore, for the pioneering run in 2007 we chose a Pt-target to optimize the observation of πK atomic-pairs. Fig. 1.5 shows the relative needed accuracy on the breakup probability to obtain a mean life measurement on πK-atoms with a precision of 20% as a function of the mean life for different targets. For the expected mean life of these atoms, i.e. 3.7 fs, Molybdenum ($Z = 42$), Titanium ($Z = 22$) and Nickel ($Z = 28$) targets have approximately the same sensitivity. In 2008, we therefore use a Ni-target to be more sensitive to the mean life measurement.

The approach for the mean life measurement of πK-atoms is discussed here. Let us denote $N^{\text{free}} \equiv N^{\text{C}} + N^{\text{nC}}$ the sum of Coulomb and non-Coulomb-pairs and $N^{\text{real}} \equiv N^{\text{free}} + n^{A}$ the sum of free and atomic-pairs. N^{real} is the total number of detected pairs by the DIRAC-II experiment once the accidental background has

been subtracted. While non-Coulomb and accidental-pairs are distributed linearly over Q, Coulomb-pairs have an enhancement for low relative momenta Q due to their Coulomb correlation. $\frac{dN^C}{dQ}$ and $\frac{dN^{nC}}{dQ}$ are the number of expected events per bin dQ from MC and normalized to one for $|Q| < 20$ MeV$/c$, the region of interest. We can consider them as the probability to have an event in bin dQ. $\frac{dN^{real}}{dQ}$ is the number of measured events per bin dQ once the accidentals are subtracted. Outside of the region where πK-atoms are expected, i.e. above 10 MeV$/c$ (fig. 1.3) one gets

$$\frac{dN^{real}}{dQ} = \beta \cdot \frac{dN^C}{dQ} + (N^{real} - \beta) \cdot \frac{dN^{nC}}{dQ}, \tag{1.18}$$

where β is the number of Coulomb-pairs. By subtracting the Coulomb and non-Coulomb contributions extrapolated to the signal region only atomic-pairs are remaining.

Due to the k-factor defined in equ.(1.14) the number of measured Coulomb-pairs are related to the number of produced atoms N^A. Together with equ.(1.16) one measures experimentally the breakup probability

$$P_{br} = \frac{n^A}{N^A} = \frac{n^A}{k \cdot N^C(\vec{Q} \in \Omega)}. \tag{1.19}$$

and therefore the mean life of πK-atoms (fig. 1.4). The latter is then related to the πK-scattering length difference through equ.(1.8). Details on the measurement of $\pi\pi$ and πK-atoms are given in chapter 5 and 6 respectively.

Chapter 2

Experimental setup

2.1 DIRAC-II spectrometer: generalities

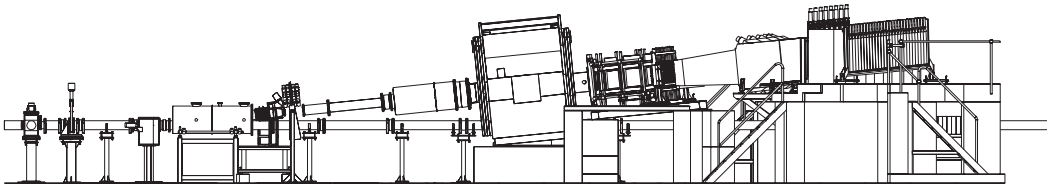

Figure 2.1: DIRAC-II setup (side view).

The initial aim of the DIRAC experiment was the detection of $\pi^+\pi^-$-pairs with low relative momentum and a small opening angle. A double arm magnetic spectrometer with a high momentum resolution (1 MeV/c) has been installed in October 1998 in the T8 experimental area of CERN PS East hall [4] [5]. A side view is given in fig. 2.1.

A 24 GeV/c proton beam from the PS interacts with a 28 μm Pt-target in 2007 and with a 94 (98) μm thick Ni-target in 2001-2003 and 2008. During the 2007 run between 3 and 7 spills per super-cycle ($14-42$ s) were assigned to DIRAC-II. A spill had a duration of 450 ms and an average intensity of $1{\cdot}10^{11}$ protons. After the target the remaining proton beam passes through a vacuum tube and is then absorbed by the beam dump. The halo is suppressed by two shielding upstream the micro drift chambers and downstream the ionization hodoscope (in blue in fig. 2.2). The axis of the spectrometer is inclined upwards compared to the proton beam by an angle of 5.7°, see the side view of the DIRAC-II experiment in fig. 2.1. The secondary particles are passing through two vacuum chambers (in green in fig. 2.2) and are deflected by the spectrometer magnet. Negative particles are crossing the right arm T2 while positive ones the left arm T1. Because the current aim of the DIRAC-II experiment is to detect πK-atoms and measure their mean life, an upgrade was performed beginning 2006. This upgrade consisted of:

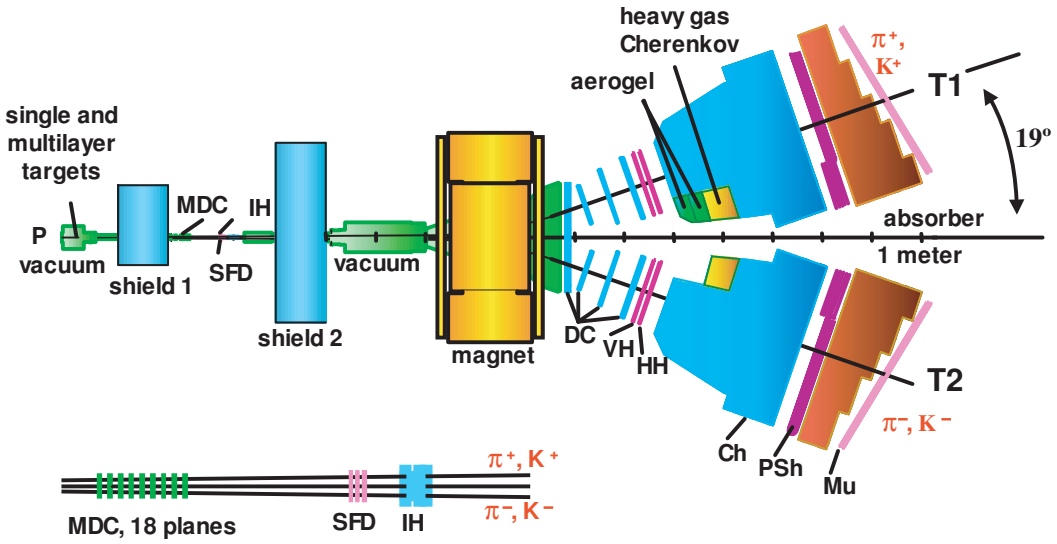

Figure 2.2: Schematic top view of the DIRAC-II setup. From left to right, the detectors are: micro drift chambers (MDC), scintillation fiber detector (SFD), ionization hodoscope (IH), 4 drift chambers modules (DC), vertical and horizontal hodoscope (VH, HH), aerogel Čerenkov counters (ChA), the heavy gas Čerenkov counters (ChF), the N_2-Čerenkov counters (Ch), the preshower detector (PSh) and behind the absorber, the muon detector (Mu).

- a new shielding (shield 1 in fig. 2.2) to decrease the counting rate by 30% in the upstream detectors, which allows an increase of the primary proton beam intensity by a factor of 2,
- an improvement of the scintillation fiber detector (SFD) and the introduction of the micro drift chambers (MDC) upstream the magnet,
- the installation of new electronics for the upstream detectors,
- an extension of the vertical hodoscope (VH), preshower detectors (PSh) and muon counters (Mu) to increase the aperture and hence the πK detection efficiency for high momenta,
- the introduction of 2 new heavy gas Čerenkov counters (one in each spectrometer arm) for pion-kaon separation,
- the addition of an aerogel threshold Čerenkov counter in the positive spectrometer arm for kaon-proton separation (the antiproton contamination in the negative arm is negligible).

The present (upgraded) setup is shown in fig. 2.2. Details can be found in [3].

A first set of detectors is located upstream of the spectrometer magnet:

- Micro drift chambers (MDC),
- Scintillation fiber detector (SFD),
- Ionization hodoscope (IH).

A second set of detectors is located downstream the magnet separated in two identical arms (except for the aerogel Čerenkov counter, which is located only in the positive spectrometer arm), including:

- Drift chambers (DC1-DC4),
- Vertical hodoscope (VH),
- Horizontal hodoscope (HH),
- Aerogel Čerenkov counter (ChA),
- Heavy gas Čerenkov counter (ChF),
- N_2-Čerenkov counter (Ch),
- Preshower counter (PSh),
- Muon hodoscope (Mu).

2.2 Upstream detectors

2.2.1 Micro drift chambers

The micro drift chambers were installed at the end of the 2007 run and results are very preliminary. They are the main tracker upstream of the magnet. The distinctive property of atomic-pairs is the passage for two charged particles at a rather small relative distance before deflection in the magnet. Therefore, upstream detectors have to measure tracks with high spatial resolution and at the same time resolve nearby tracks. In the future, the chambers will be operated in a high current avalanche mode, most probably with the gas mixture Ar(0.33%) + CH(0.66%) + HO(0.01%). The most important features of the detector are:

- a total of 18 planes,
- a spatial accuracy $\sigma = 30$ μm,
- a double track resolution $\sigma = 200$ μm,
- one plane efficiency at beam intensity $I = 2 \cdot 10^{11}$ protons per spill $> 98\%$, due to the "dead zone",
- a time resolution $\sigma = 1$ ns,
- a very low integral material budget.

2.2.2 Scintillating fiber detector

The scintillating fiber detector is, together with the MDC, used for tracking upstream of the magnet. Before 2004 it also provided a trigger signal for rejection of pairs with a relative distance larger than a given threshold. The SFD consists of three fiber planes. Two of them measure the X and Y coordinates perpendicular to the beam. The third one was added later in 2002 to improve the efficiency and measures the W coordinate (in the same plane as the X and Y coordinates, but rotated by an angle of 45° with respect to the X and Y axis). The X and Y planes each have 5 layers of fibers with a diameter of 0.26 mm (instead of 0.44 mm as it was the case before the upgrade), whereas the W plane has only 3 layers of fibers. The active area is 105×105 mm^2. The fibers of one column (5 or 3) are bundled up and attached to a 16 channel position sensitive photomultiplier (PSPM), Hamamatsu H6568. The principal structure of the SFD and the PSPM mapping is shown in fig. 2.3. The performance of this detector can be summarized as:

- average detection efficiency: 98.4%,
- spatial resolution $\sigma = 127$ μm,
- time resolution $\sigma = 0.65$ ns.

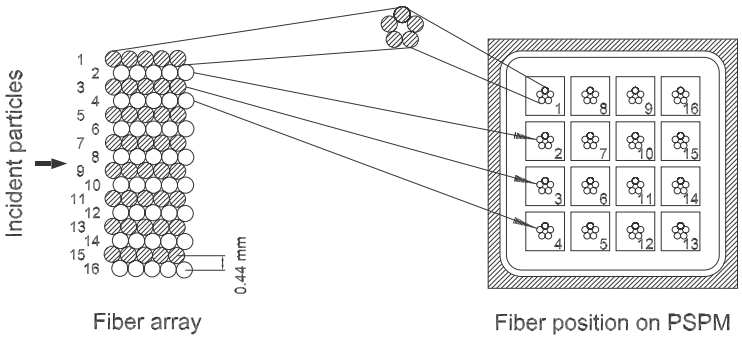

Figure 2.3: Main characteristic of the SFD and mapping of the PSPM readout.

2.2.3 Ionization hodoscope

The distance between two particles from the breakup of an atom is rather small and can be even lower than the resolution of the upstream tracker (MCD and SFD). In this case, only one hit is detected and the reconstruction efficiency is reduced. In order to avoid this, the ionization hodoscope based on the measurement of the ionization losses is used to separate single tracks from double tracks.

The ionization hodoscope consists of 4 planes perpendicular to the beam with 16 scintillating slabs each. One slab is 11 cm long, 7 mm wide and 1 mm thick. For two planes, the slabs are orientated horizontally and for the two others, vertically.

They are connected to the photocathode of the FEU-85 PMs through a lucite light guide, see fig. 2.4. The IH has a time resolution less than 1 ns. For a threshold set to detect 90% of the double tracks, the contamination of the single tracks is around 15%.

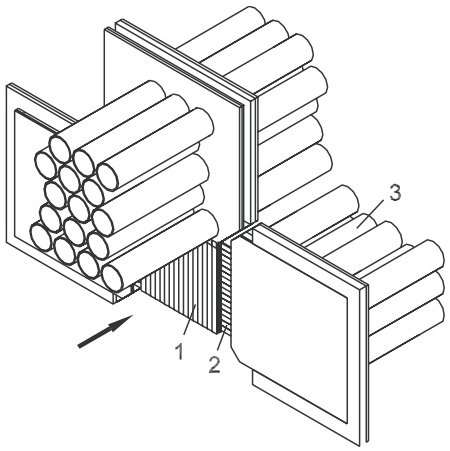

Figure 2.4: Schematic view of the IH. 1: scintillator slabs, 2: light guide, 3: photomultipliers.

2.3 Downstream detectors

2.3.1 Drift chambers

The drift chambers consist of four modules. They are used for tracking downstream the magnet. The general properties of the modules are given in table 2.1. The DC-1 is, for example, a sequence of 6 planes X-Y-W-X-Y-W, where W is rotated by 11.3° compared to the X and Y planes.

Module type	Sensitive area (cm^2)	Measured coordinates	Number of planes
DC-1	40 × 80 left arm	X, Y, W	2+2+2
DC-2	40 × 80	X, Y	1+1
DC-3	40 ×112	X, Y	1+1
DC-4	40 × 128	X, Y	2+2

Table 2.1: General properties of the DC modules.

The anode wire pitch is 10 mm and the distance between the anode and the cathode planes is 5 mm. Between two anode wires a potential wire with a diameter of 100 μm is used to operate the chambers in the high current avalanche mode. The frames are made of aluminum and fiberglass. The latter provides the support for the electrodes and the aluminum is used as a spacer as well as to hold the mylar

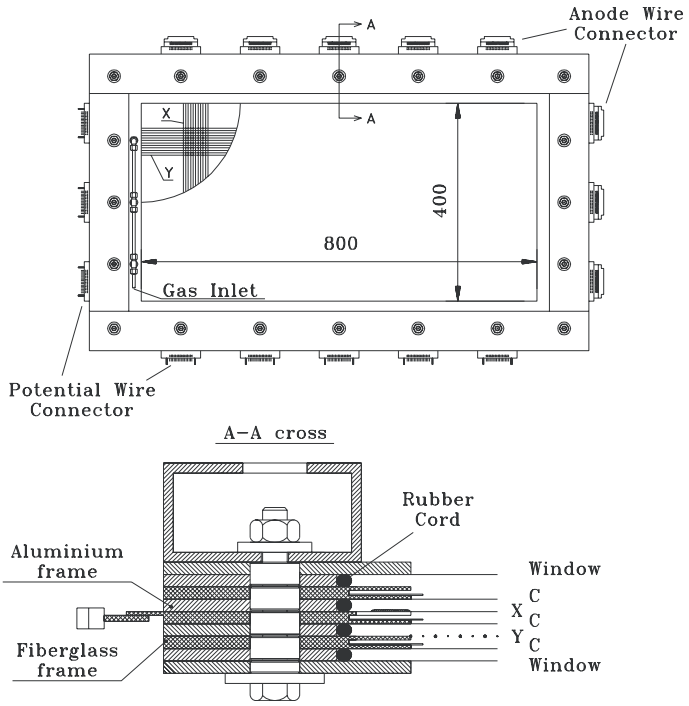

Figure 2.5: Schematic view of the DC-2. Top: general drift chamber design. Bottom: structure of the frame stack. C denotes the cathode foils.

foil for the outer frame. A schematic view of the second module (DC-2) is shown in fig. 2.5. The overall performances of the drift chambers can be summarized as:

- space resolution: $\sigma = 90$ μm,
- single hit efficiency: $\sigma = 96\%$,
- tracking efficiency: $\sigma = 99\%$.

2.3.2 Vertical and horizontal hodoscopes

The vertical and horizontal hodoscope are used for fast coincidence between the two spectrometer arms, necessary for the trigger. They are made of horizontal and vertical scintillating slabs.

Vertical hodoscope

The vertical hodoscope is used by the high level trigger for a very fast and precise timing, rejecting pairs with a relative momentum Q above a given threshold. Also the timing from this detector is used off-line for rejection of accidental-pairs. A third purpose of the VH is the background rejection of proton-pion pairs in the pion-pion pairs signal using the time of flight technique. This part will be improved with the

introduction of the aerogel Čerenkov counter (chapter 3). The VH consists of two planes each composed of 18 vertical scintillating slabs. One slab has a length of 40 cm, a width of 7 cm and a thickness of 2.2 cm. The light is read-out on each slab end by two Hamamatsu R1828-01. The VH performances are:

- single hit detection efficiency for the positive arm: 99.5%,
- single hit detection efficiency for the negative arm: 98.8%,
- time resolution per counter: σ =127 ps,
- proton-pion separation from 1 to 5 GeV/c using time of flight (TOF) techniques,
- kaon-pion separation from 1 to 2.5 GeV/c using TOF.

Horizontal hodoscope

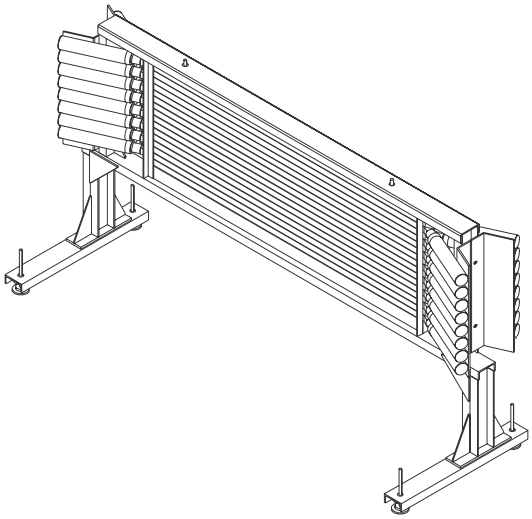

Figure 2.6: Sketch of the horizontal hodoscope.

The horizontal hodoscope is used in the first level trigger for a coplanarity cut: events with a track in each spectrometer arm with a relative vertical distance larger than two slabs are rejected. The HH covers an active area of 40 $\times$ 130 cm^2 in each spectrometer arm. For each arm the hodoscope consist of 16 horizontal extruded scintillating slabs as shown in fig. 2.6. The photons are detected by Philips XP 2008 photomultipliers. The single hit resolution is better than 96.6% and the time resolution is σ = 320 ps.

2.3.3 Čerenkov counters

In addition to the N_2-Čerenkov counter, additional detectors were introduced for kaon identification: the heavy gas counters and the aerogel counter. Their position has been determined by simulating the kaon trajectories originating from ionized πK-atoms, see fig. 2.7. The strongly asymmetric trajectory comes from the fact that particles originating from the breakup of atoms have a very low momentum in the center of mass (fig. 1.2). Therefore, they have almost the same velocity in the laboratory system and light particles are more deflected than heavy ones.

The heavy gas counter separates kaons from pions while the aerogel counter separates kaons from protons. Due to the strong suppression of antiprotons compared to protons, only the positive arm is equipped with an aerogel counter. The original N_2-tank had to be cut to clear space for the two new Čerenkov detectors, see fig. 2.8. This modification reduces the electron/positron rejection efficiency, which can be compensated by the preshower detector.

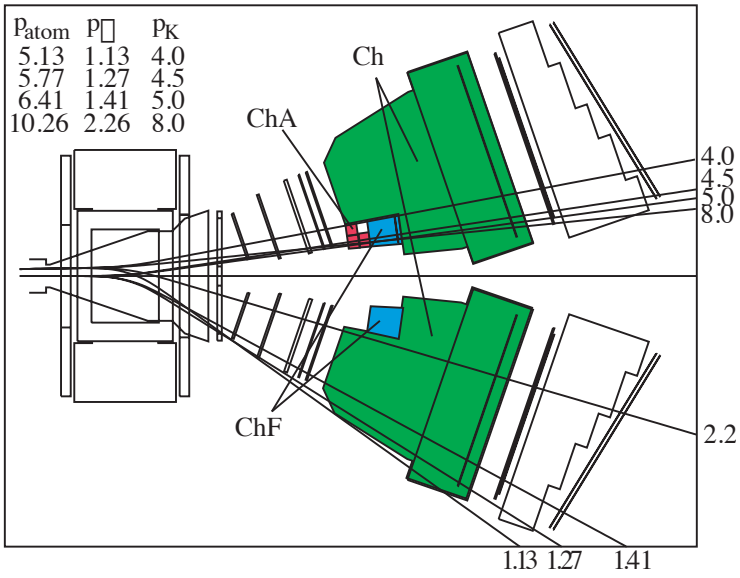

Figure 2.7: Trajectories of K^+ and π^- from πK-atoms for various momenta in GeV/c. The table (upper left corner) gives the π and K momenta for various momenta of πK-atoms.

N_2-Čerenkov counter

The N_2-Čerenkov counter is crucial for the rejection of electrons and positrons. Electron-positron pairs from photon conversions are time correlated and otherwise difficult to suppress. The Ch consist of two identical counters, one in each spectrometer arm. The radiator is nitrogen at ambient temperature and pressure. The Čerenkov opening angle of emitted light is $\theta_{Ch} = 1.4°$ for $\beta = 1$. The surface of the

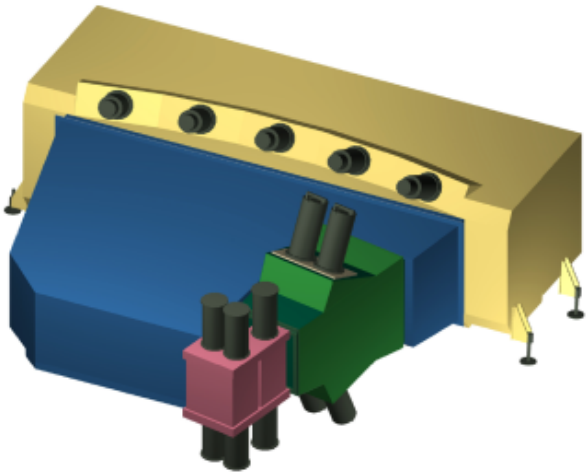

Figure 2.8: The N_2-Čerenkov detector is shown in blue. Its tank has been modified to clear space for the two new Čerenkov detectors: in green the heavy gas and in red the aerogel modules.

entrance and exit windows are 143 × 56 cm^2 and 336 × 96 cm^2, respectively. The Čerenkov light is reflected by 20 spherical mirrors and focused onto 10 photomultipliers Hamamatsu R1587 with UV-window. The output signal is the linear sum of the analogue signals from the PMs.

The performances of the Ch counter for the part with full radiator length are:

- the mean number of collected photoelectrons is 16.3 for $\beta = 1$,
- the detection efficiency is hence greater than 99.8%,
- the contamination from pions above Čerenkov threshold is around 1.5%.

Heavy gas Čerenkov counter

The heavy gas Čerenkov counter shown in fig. 2.9 detects pions and can be used in coincidence for the $\pi\pi$-atoms measurement to reduce contamination from other particle types, or in anti-coincidence for πK-atom observation. The C_4F_{10} gas used as radiator is cleaned permanently by a complex system [39], to achieve a very high purity. Each module is read out by four Hamamatsu R1584 5-inch PMs. Fig. 2.10(a) shows the integrated pulse height of the analogue sum of the four PMs as a function of the momentum for the ChF module installed in the right arm T2. Electrons are rejected using the Ch in anti-coincidence. Anti-protons and kaons are strongly suppressed so that mainly pions are contributing to fig. 2.10. The associated ADC spectrum for p > 4 GeV/c is shown in fig. 2.10(b). The average number of photoelectrons for pions is between 20 and 25 depending on the momentum.

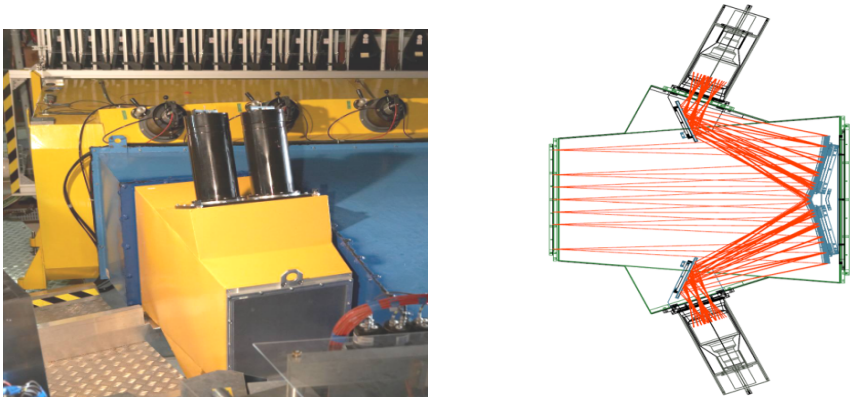

(a) (b)

Figure 2.9: (a): One of the heavy gas Čerenkov detector installed in the negative spectrometer arm. (b): Sketch of the inner part of the heavy gas detector illustrating the Čerenkov light propagation. The photons are first reflected backwards by a set of four spherical mirrors and then focused on the photocathode by flat mirrors.

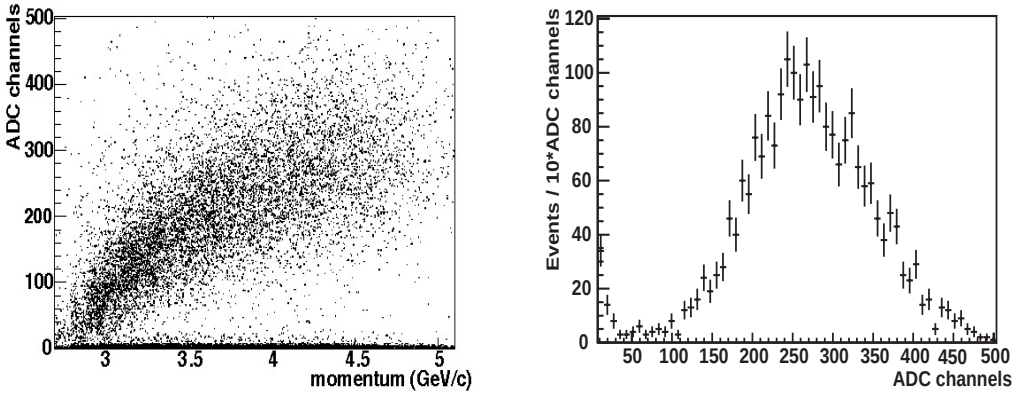

(a) (b)

Figure 2.10: Integrated pulse height of the analogue sum of the four PMs as a function of momentum for pions (a) and the associated ADC spectrum for $p > 4$ GeV/c (b).

Aerogel Čerenkov counter

This counter will be described in chapter 3 in detail as it is the main part of this work.

2.3.4 Preshower detector

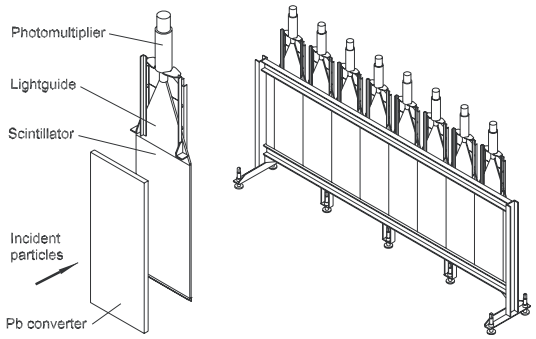

Figure 2.11: Preshower detector components and assembly.

The preshower detector was used to reduce the small fraction of 0.2% of the undetected electrons by the N_2-Čerenkov counter. A thin lead converter typically between 10 and 25 mm is placed in front of a 10 mm thick scintillator which is connected to the PMs through a light guide (fig. 2.11). Since the nuclear interaction length is approximatively 18 cm for lead and the electromagnetic radiation length is only 6 mm, it is possible to easily distinguish between electrons and hadrons by measuring the number of charged particles in the shower by their energy losses in the convertor. The cut in the ADC spectrum has been adjusted offline in order to keep 95% of pions while rejecting 85% of electrons/positrons. This detector became particularly important in the region of the heavy gas and the aerogel Čerenkov counter since the electron/positron rejection efficiency dropped due to the shortness of the radiator length. To compensate this inefficiency, the size of the scintillating slabs have been reduced by a factor of two and a second row of absorber-scintillator was installed in this area (fig. 2.2).

2.3.5 Muon detector

Muon pairs are mainly produced from the desintegration of pions and are like electrons an important source of background. The muon detector consists of two layers of 28 scintillators in each arm located behind a thick iron absorber with a thickness between 60 and 140 cm. The absorber is thicker, closer to the symmetry axis of the two spectrometer arms compensating for the higher momentum of the hadrons. Each 5 mm thick scintillator has an active area of 75×12 cm^2. The scintillators are coupled to fish-tail light guide and then read out by 25 mm FEU-85 PMs. For the second layer, some of the scintillators are directly coupled to the PMs, because of

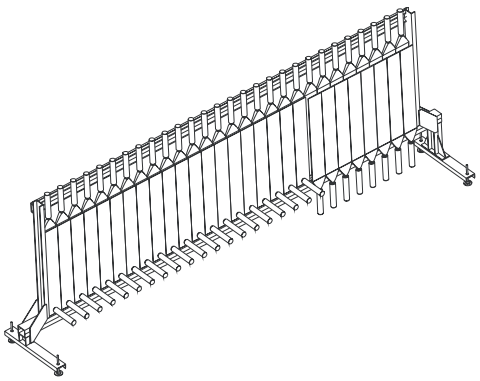

Figure 2.12: Assembly of the muon detector. Because of the floor some of the scintillators are coupled directly to the PMs without light guides.

space constraints (floor) see also fig. 2.12. To compensate the decrease of the light collection efficiency, these scintillators are two times thicker. The time resolution is 1.3 ns.

2.4 The trigger

Several triggers are available in the DIRAC-II experiment. One can separate them into two classes: the special triggers and the more complicated triggers for atomic searches. These triggers have two levels: the first level T1 trigger based on combinatorial logic and the T4 software trigger with track finder and track analyzer using informations from the drift chambers only. The special triggers are ($\bigcup \equiv$ AND):

- the electron trigger: $(\mathrm{VH} \bigcup \mathrm{HH} \bigcup \mathrm{Ch})_{\mathrm{left}} \bigcup (\mathrm{VH} \bigcup \mathrm{HH} \bigcup \mathrm{Ch})_{\mathrm{right}}$
- the pion trigger: $\left(\mathrm{VH} \bigcup \mathrm{HH} \bigcup \overline{\mathrm{Ch}}\right)_{\mathrm{left}} \bigcup \left(\mathrm{VH} \bigcup \mathrm{HH} \bigcup \overline{\mathrm{Ch}}\right)_{\mathrm{right}}$
- the minimum bias trigger left arm: $(\mathrm{VH} \bigcup \mathrm{HH})_{\mathrm{left}}$
- the minimum bias trigger right arm: $(\mathrm{VH} \bigcup \mathrm{HH})_{\mathrm{right}}$.

For the electron and the pion trigger the first level T1 trigger selects symmetric tracks requiring a hit in the same slab of the VH for each arm of the spectrometer.

The atomic triggers are the following:

- the $\pi\pi$ trigger: $\left(\mathrm{VH} \bigcup \mathrm{HH} \bigcup \overline{\mathrm{Ch}}\right)_{\mathrm{left}} \bigcup \left(\mathrm{VH} \bigcup \mathrm{HH} \bigcup \overline{\mathrm{Ch}}\right)_{\mathrm{right}} \bigcup \mathrm{Copl} \bigcup \mathrm{T4}$
- the $K^+\pi^-$ trigger:
  $\left(\mathrm{VH}(16-20) \bigcup \mathrm{HH} \bigcup \overline{\mathrm{Ch}} \bigcup \overline{\mathrm{ChF}}\right)_{\mathrm{left}} \bigcup \left(\mathrm{VH}(1-15) \bigcup \mathrm{HH} \bigcup \overline{\mathrm{Ch}}\right)_{\mathrm{right}} \bigcup \mathrm{Copl} \bigcup \mathrm{T4}$
- the $K^-\pi^+$ trigger:
  $\left(\mathrm{VH}(1-15) \bigcup \mathrm{HH} \bigcup \overline{\mathrm{Ch}}\right)_{\mathrm{left}} \bigcup \left(\mathrm{VH}(16-20) \bigcup \mathrm{HH} \bigcup \overline{\mathrm{Ch}} \bigcup \overline{\mathrm{ChF}}\right)_{\mathrm{right}} \bigcup \mathrm{Copl} \bigcup \mathrm{T4}.$

"Copl" means that coplanarity is required between the positive and negative particles which have to cross the same or an adjacent slab of the HH. From the momentum distribution it is known that the kaon has a trajectory close to the primary beam line between slab 16-20 in the vertical hodoscope and the pion due to its lower mass crosses the vertical hodoscope between slab 1-15, see fig. 2.7. Therefore the T1 trigger is, in contrast to the pion trigger, looking for asymmetric tracks in the two spectrometer arms.

The high level trigger T4 uses the DC to reconstruct the tracks in the horizontal x-direction. This allows a rough estimation of the relative momentum Q. In a first step the track finder is just using information from the hit wire. The drift time is not used. If a track with more than three consistent hits is found in each arm the track analyzer is invoked. A look up table allows to attribute to each track combination a relative momentum. This permits to reject events with high relative momenta. During the 2007 run, data were taken with the so-called *mixed trigger* which contains the $K^-\pi^+$, the $K^+\pi^-$, the $\pi\pi$ and the electron trigger.

2.5 The software

In this section we describe the software used in DIRAC-II for the generation of events and the simulation of the setup as well as the reconstruction of the Monte-Carlo (MC) and data tracks.

DIPGEN (**DI**RAC **P**airs **Gen**erator) is a kinematics generator which simulates the events needed in DIRAC-II, i.e. accidentals, Coulomb, non-Coulomb and atomic-pairs. DIPGEN is written in C++ and uses ROOT classes. The required input is the total inclusive πK laboratory momentum distribution at the target. A vertex, the momenta and the associated relative momentum Q are generated depending of the type of events:

- non-Coulomb-pairs and accidentals are supposed to have uniform distributions of Q,
- Coulomb-pairs have the non-Coulomb distribution Q modified by the Gamov-Sommerfeld factor to include the Coulomb correlation,
- for atomic-pairs, Q is generated taking into account the whole set of cross-sections describing the evolution of atoms in matter.

More details are given in [40].

The events are then propagated forward through the DIRAC-II spectrometer using *GEANT-DIRAC* the MC describing the full setup based on GEANT3. All materials, the magnetic field are taken from the spectrometer specifications in order to match the simulation of absorption, multiple scattering and all sources of background with the measured data. More details are given in [41]. A user guide is available in [42]. The trigger and the detector responses are simulated separately using collected data. The digitization of the response of the aerogel modules has

been implemented by myself using a lookup table. For each particle type, impact position and momentum, an ADC and TDC hit are generated according to the measured spectra. A user guide for the digitization can be found in [43]. MC events as well as data events are reconstructed using the so-called software *Ariane*. Details are given in [44].

Chapter 3

The aerogel Čerenkov counter

To measure the distribution of πK-atoms in the DIRAC-II experiment, one needs to identify kaons in the momentum range between 4 to 8 GeV/c. The time of flight technique is not adequate for the separation of kaons and protons at such energies. I therefore use the Čerenkov technique. Silica aerogel is the only material with a refractive index between those of condensed or solid phases and gases, as it is required here for a proper kaon identification. Due to the wide momentum range a duplex design has been chosen. The counter consists of overlapping modules with two different refractive indices $n = 1.015$ and $n = 1.008$.

The Čerenkov light yield is proportional to $1 - (\beta n)^{-2}$ and therefore very small. Furthermore, due to the large spatial kaon distribution at the location reserved for the Čerenkov counter in DIRAC-II experiment, a sensitive area of 440 $\times$ 340 mm^2 is needed. Such a large area leads to strong absorption of the produced Čerenkov light in aerogel. Therefore, to optimize the detector performance, cosmic ray tests and simulation based on GEANT4 were used. Thereby a novel design has been developed using a pyramidal shape of the aerogel radiator and alternating layers of aerogel tiles and diffusive reflector foils coated with wavelength shifter.

3.1 History and properties of Čerenkov radiation

In 1910, Marie Curie observed blue light emitted from radium solutions, without understanding this effect [45]. In 1934, P. A. Čerenkov and S. I. Vavilov rediscovered Čerenkov radiation while irradiating liquids with gamma-rays [46], but they made Compton-electrons responsible for this effect. Three years later, I. Tamm and I. Frank presented a first quantitative theory [47]. In 1958, I. Tamm, I. Frank and P. A. Čerenkov were awarded the Nobel prize. They explained the phenomenon with the classical Huygens principle: when a high energy particle crosses a dielectric, the emitted spherical light waves form a wave front at a given angle to the particle trajectory. This coherent radiation is produced as soon as the velocity $v = \beta \cdot c$ of the particle is higher than the speed of light c/n in the medium, where n is the

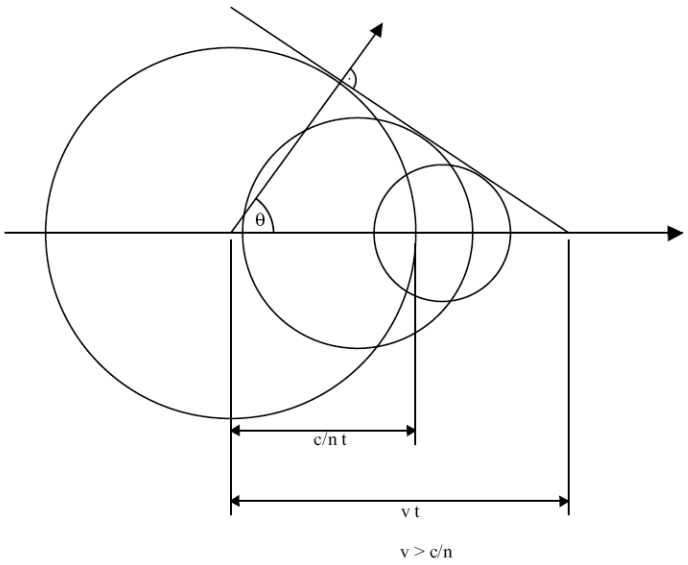

Figure 3.1: Shock wave generated by a particle moving faster than the speed of light in a medium with refractive index n.

refractive index. The minimum velocity β_{min} is:

$$\beta_{min} = \frac{1}{n}. \tag{3.1}$$

Using Huygens geometrical construction (fig. 3.1) one observes that in three dimensional space, the wave front forms the surface of a cone with the particle trajectory as axis and with an opening angle defined as:

$$\begin{aligned} \cos\theta &= (c \cdot \frac{t}{n})/(\beta c \cdot t) \\ &= \frac{1}{\beta n}, \quad \beta > 1/n. \end{aligned} \tag{3.2}$$

For a low energy charged particle in a medium, the induced polarization cancels out, leaving no remaining field (fig. 3.2a). However for velocities of the particle higher than the speed of light in the medium the processes are different. As the influence of the charge propagates with the speed $v = c/n$, one encounters a asymmetric charge distribution leading to a dipole moving through the medium. According to classical electrodynamics, emitted waves cancel out via interference except on a cone with opening angle θ, the Cherenkov angle, where constructive interference leads to photon emission (figure 3.2b). Using equ. (3.1), the threshold speed is defined by:

$$\gamma_{min} = \frac{1}{\sqrt{1-\beta_{min}^2}} = \frac{n}{\sqrt{n^2-1}}. \tag{3.3}$$

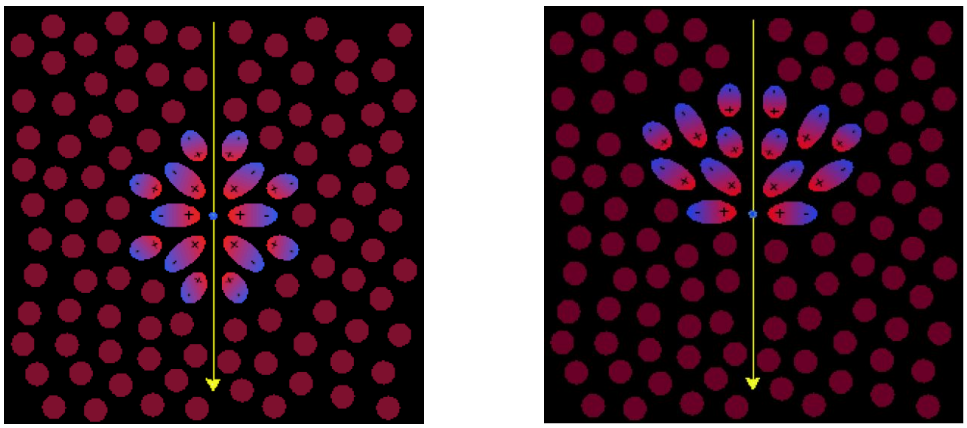

(a) (b)

Figure 3.2: Schematic representation of the production of Čerenkov radiation. (a): The speed of the particle is less than the speed of light in the medium. Thus the medium is symmetrically polarized with no resulting dipole field. (b): The particle velocity is larger than the speed of light in the medium, an asymmetric polarization causes a dipole field which manifests itself an electromagnetic radiation during the buildup of the field.

Čerenkov radiator materials	$n-1$	γ_{min}
Helium	$3.3 \cdot 10^{-5}$	123.0
CO_2	$4.3 \cdot 10^{-4}$	34.0
C_4F_{10}	$1.53 \cdot 10^{-3}$	18.3
Pentane	$1.7 \cdot 10^{-3}$	17.2
C_5F_{12}	$1.72 \cdot 10^{-3}$	16.9
Aerogel	$0.075 \ldots 0.008$	$2.7 \ldots 8.0$
H_2O	0.33	1.52
Glass	$0.75 \ldots 0.46$	$1.22 \ldots 1.37$

Table 3.1: Čerenkov radiator properties.

The intensity of the spectral distribution (number of photons per unit of wavelength λ and unit of radiator length l) is given by the Frank-Tamm relation [47]:

$$\frac{dN_\gamma}{d\lambda dl} = 2\pi \cdot \alpha \cdot z^2 \cdot \frac{1}{\lambda^2} \cdot \left(1 - \frac{1}{(n\beta)^2}\right), \tag{3.4}$$

where $\alpha = \frac{1}{137}$, is the electromagnetic fine structure constant and z the charge of the particle, which is usually $z = 1$ in high-energy physics. Hence Čerenkov radiation consists mostly of UV light.

Table 3.1 lists several materials suitable as radiator for Čerenkov detectors. The refractive index is quoted for the gas at 273 K/ 760 mm Hg for the sodium d-line at 589.3 nm. The data show that most regions for $\gamma = 1.2 \ldots 100$ are covered by solid, liquid, gaseous and aerogel radiator materials.

Based on relation 3.3 one can correctly choose the refractive index of the radiator, so that only particles with γ above γ_{min} produce Čerenkov radiation. This is exactly the principal of a Čerenkov threshold counter. As an example kaons and lighter particles can be separated from protons for a momentum smaller than 5.3 GeV/c, using aerogel with a refractive index $n = 1.015$. Above this momentum even protons can produce Čerenkov light.

3.2 Aerogel

Aerogel is chemically identical to quartz but with a low density ρ. Depending on the refractive index, the range is between $\rho = 30$ and $\rho = 300$ mg/cm^3. As shown in table 3.1, gaseous radiators have a refractive index below $n = 1.002$ and solid or liquid radiator have their indices above $n = 1.3$. The refractive indices of aerogel are just in between them. This property makes aerogel so important for particle identification. Its drawback is the poor optical transmittance and therefore a small number of detected photons. Nevertheless, aerogel is widely used as a Čerenkov radiator, as for instance in LHCb [48], in BELLE [49], HERMES [50] and many other experiments.

3.2.1 Production

Two different types of aerogel can be found on the market[1]:

- *hydrophilic*, produced by the Budker Institute of Nuclear Physics (BINP) together with the Boreskov Institute of Catalysis (BIC) in Novosibirsk (Russia). Since this aerogel absorbs water it has to be kept dry to avoid a significant decrease in quality.
- *hydrophobic*, produced by Matsushita (Panasonic) Electric Works (MEW) Ltd. in Japan. This aerogel is not sensitive to water and hence much more stable.

The two production procedures are similar. For the production of the hydrophilic aerogel, the first step consists of the formation of *alcogel* (SiO_2). The gelation of alcogel takes place by mixing distilled water and methyl-silicate ($Si(OCH_3)_4$) together with ammoniac as a catalyst:

$$\mathrm{nSi(OCH_3)_4 + 4nH_2O \rightarrow nSi(OH)_4 + 4nCH_3OH}, \tag{3.5}$$

and

$$\mathrm{nSi(OH)_4 \rightarrow \{SiO_2\}_n + 2nH_2O}. \tag{3.6}$$

The second step consists of an aging process which takes two weeks, in order to remove the water and to proceed further polymerization. Then, the alcogel has to

[1] Other companies produce aerogel, but not with comparable optical quality. For example, in [51] two hydrophobic aerogels are compared; Panasonic and Airglass Inc., the number of photoelectrons is 2.5 times larger with the aerogel produced by Panasonic.

be dried to become silica aerogel. Removing the methanol (CH_3OH) from the alcogel is the difficult part. Because of capillary forces, drying leads to strong compressions and deformations of the structure. The liquid is therefore removed in an autoclave under supercritical conditions (280° C and a pressure of 120 atm). To improve the optical properties and remove impurities, the aerogel is then baked in an oven at 600° for three hours. After baking, the scattering length is improved by 10-50%. Other reactions are possible for the production of alcogel, using ethanol and different catalysts. At the Boreskov Institute of Catalysis in Novosibirsk, alcogel is produced through the reaction:

$$Si(OEt)_4 + 2H_2O \rightarrow SiO_2 + 4HOEt, \tag{3.7}$$

where Et stands for ethanol [52]. Aging, drying and baking is similar.

For the hydrophobic aerogel, the hydrophilic $-OH$ group in the alcogel is replaced by the hydrophobic $-O-Si(CH_3)_3$ group.

3.2.2 Properties of the aerogel

For applications of aerogel as a Čerenkov radiator, three parameters are important:

- the index of refraction n, which is related to the density ρ (g/cm^3) through the relation:

  $$n = 1 + 0.21\rho. \tag{3.8}$$

  By changing the amount of solvent during the preparation, one can alter the volume occupied by aerogel and hence the density. Also, by baking at temperatures around 700° C, the index of refraction can be increased.

- the Rayleigh scattering length, which is determined by interactions between the structure of the aerogel and the wavelength λ of the incoming light.

- the absorption length, which is determined by impurities, mainly due to iron ions Fe^{3+}. The absorption length is always much longer than the Rayleigh scattering length.

The absorption length is given in fig. 3.3(a) for the $n = 1.05$ aerogel. This index is too high for our proposal but the producer claims that differences in the absorption length are negligible. The Rayleigh scattering length is proportional to λ^{-4}. Usually, the Rayleigh scattering length is given by the value at 400 nm, which is in this case around 40 mm. The corresponding information from Panasonic are not available. Nevertheless, fig. 3.3(b) shows the absorption length for this type of aerogel with $n = 1.03$ measured by the Novosibirsk group [53]. The absorption and Rayleigh scattering lengths are smaller than for the aerogel from Novosibirsk. However, the indices of refraction are different. Table 3.2 summarizes the principal aerogel specification for the one from Novosibirsk (BIC) and the one from Panasonic (MeW).

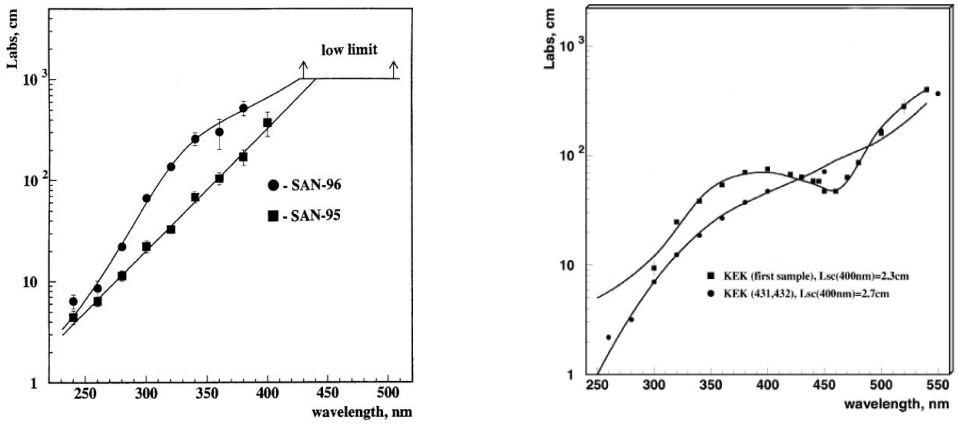

(a) (b)

Figure 3.3: (a): Absorption length as a function of the wavelength for the $n = 1.05$ aerogel produced in Novosibirsk. SAN-95 is the aerogel produced in 1995, SAN-96 is the one produced since 1996. (b): Absorption and Rayleigh scattering length for the aerogel produced by Panasonic with an index of refraction $n = 1.03$.

	n	Unit tile [mm^3]	L_{sc} [mm]	L_{abs} [cm]	
			at 400 nm	at 270 nm	at 350 nm
BIC	1.05, 1.008	$53 \times 53 \times 23.3$	>40	∼10	∼300
MEW	1.015	$111 \times 111 \times 10.5$	>30	∼5	∼40

Table 3.2: Aerogel specifications.

3.2.3 Measurement of the refractive index

Since equ.(3.8) relates the index to the density, one can measure the index of refraction by weighting the aerogel. However, due to the importance of this index for a proper particle separation, a little setup has been built to measure more precisely this index with a laser. A block of aerogel is placed on a rotating table. The laser beam crosses the corner of the block, see photos 3.4. Measuring the deflection of the laser for different incoming angles gives a precise measurement of the index of refraction. A schematic drawing is shown in fig. 3.5 (a), where α is the incoming angle, β the angle of the piece of aerogel and γ the deflection. α, β and γ are related to the index of refraction through

$$\gamma = \alpha - (\beta + \frac{\pi}{2}) + \arcsin\left(\sin\alpha \sin\beta + n\sqrt{1 - \frac{\sin^2\alpha}{n^2}}\cos\beta\right). \qquad (3.9)$$

Fig. 3.5(b) shows the measurement for a piece of $n = 1.05$ aerogel together with the fit function from equ.(3.9) leading to $n = 1.055 \pm 0.002$.

(a) (b)

Figure 3.4: Setup for the refractive index measurement. (a): The laser crosses the aerogel and its deflection is measured. (b): Top view of the laser diode and the tile of aerogel on the rotating table.

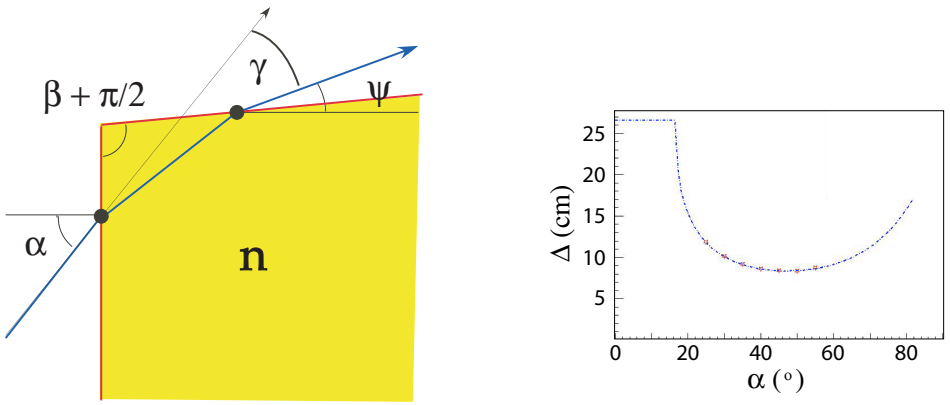

(a) (b)

Figure 3.5: (a): Principal of the refractive index measurement; (b): Measurement of the laser spot displacement for several incident angles, with a fit following equ.(3.9).

3.3 Cosmic ray test setup

In order to test the various designs and to optimize the detector, a test setup has been constructed.

A schematic drawing of the entire setup is presented in fig. 3.8. The test counter consists of an outer light-tight aluminum box equipped with two cylinders, each housing a 5-inch PM. The volume of the outer box is 500(H) × 400(W) × 400(Th) mm^3. The two PMs were mounted horizontally in the cylinders, facing each other (fig. 3.6(a)). The distance between the two PMs is adjustable between 100 and 350 mm. The different prototypes were made of plastic plates. In the cosmic-ray tests two Hamamatsu R1584 PMs were used. I chose such a large photomultiplier, since the light collection efficiency grows with the size of the active area of the detector, see equ.(3.10). Additionally, they have UV windows, that allows the detection of photons in UV-range down to 200 nm.

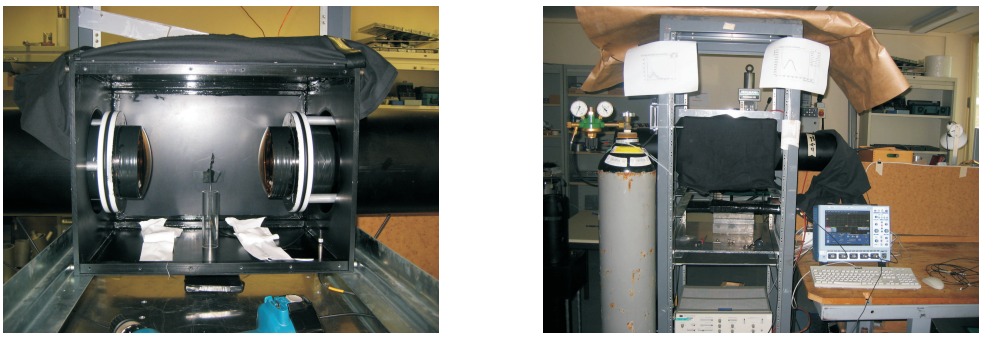

(a) (b)

Figure 3.6: (a): Empty black light-tight box with the two photomultipliers. (b): Setup with the oscilloscope used as DAQ on the right, the nitrogen bottle for aerogel storage on the left and the black box in the middle.

The test detector was set up in the laboratory with three trigger counters, as shown in fig. 3.8. The three scintillation counters S_1, S_2 and S_3 had an area of 100×100 mm^2. S_1 and S_2 were used in coincidence to trigger on vertical cosmic muons. The trigger rate for S_1S_2 was 0.1 counts/s. The third counter S_3 located under the lead absorber was used to set a momentum threshold on incoming muons (for example 66 cm of lead for a momentum for 1 GeV/c [54]). The counting rate dramatically decreased with S_3, mainly due to the tighter restriction in solid angle acceptance, but also due to the momentum distribution of cosmic muons for higher momenta (fig. 3.7).

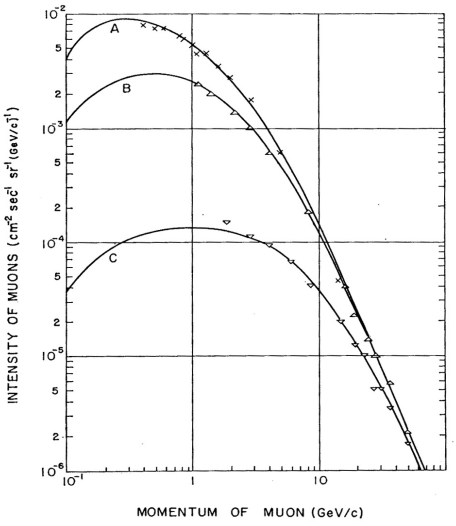

Figure 3.7: Differential momentum distribution of cosmic muons: a) at 3200m and vertical tracks; b) at sea level and vertical tracks; c) at sea level and 68° [63].

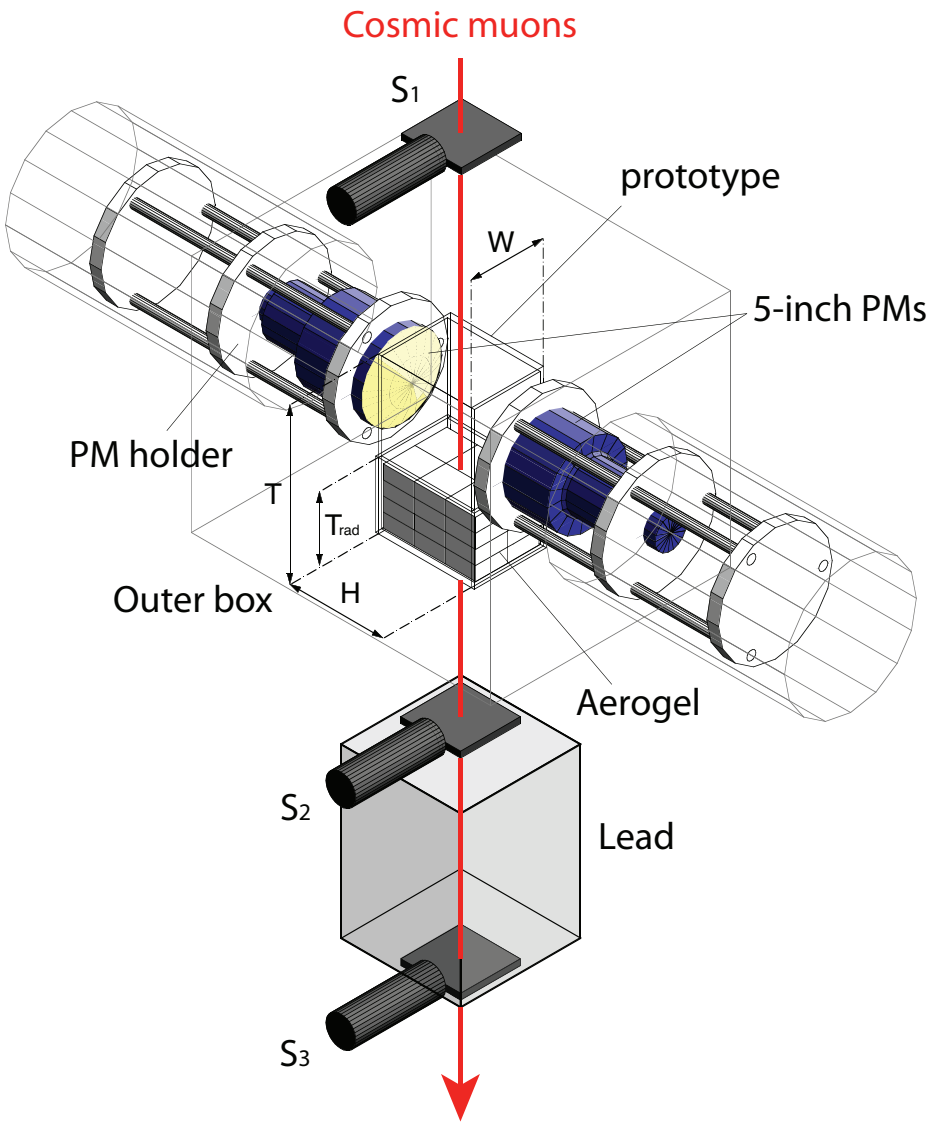

Figure 3.8: Schematic drawing of the cosmic-ray setup.

A LeCroy Wavesurfer 454 oscilloscope was used for data acquisition. The waveforms from the two PMs were saved as ASCII files in the hard disk of the oscilloscope. The oscilloscope could be connected to the network via TCP/IP. A picture of the entire setup is shown in fig. 3.6(b). The data were transfered to a PC for offline analysis, where the waveforms were integrated over a given time gate to calculate the collected charge. The number of detected photoelectrons was obtained from the amplitude spectra with single photoelectron events (section 3.6).

3.4 Direct and diffusion box design

For threshold Čerenkov counters, light can be collected using diffusive reflectors or mirrors. The diffusive geometry usually requires larger volumes of the radiator than mirror light collection geometries. For aerogel, one usually uses diffusive reflectors because of the small Rayleigh scattering length. There are two main diffusive designs: the *direct* design and the *diffusion box* design.

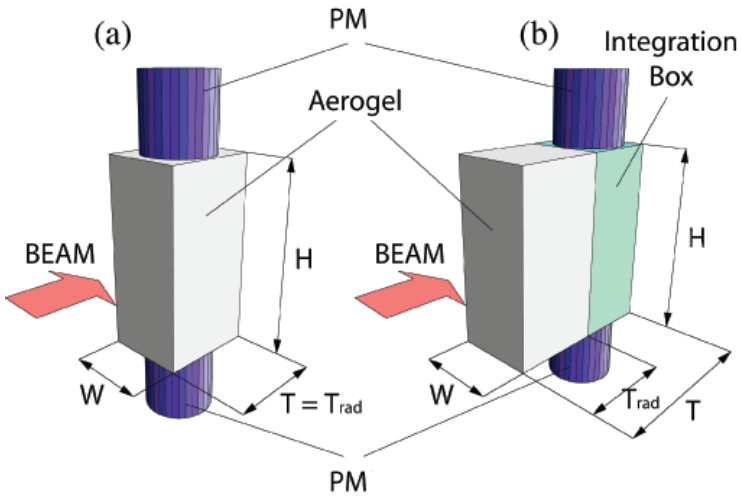

Figure 3.9: Sketch of threshold Čerenkov counters: direct (a) and diffusion box (b) design.

In the direct design, a light tight box is filled with aerogel and PMs are in direct contact with the radiator (fig. 3.9(a)). The inner walls are covered with a diffuse reflector, Tetratex[2] for instance. A diffuse reflector is important since almost no direct light, but only diffused light is detected. Furthermore, the light trajectory is dominated by Rayleigh scattering [53] [56] .

The weak point of this design is the strong correlation between the number of photoelectrons and the impact position of incoming particles. Due to the high absorption in aerogel, photons produced in the center of the detector have a much

[2]Tetratex PTFE-Membran is a woven Teflon produced by Donaldson Filter Components Ltd. and characterized by a very high reflectivity [55].

higher probability not to be detected than photons produced close to one of the PMs. This difference in the light collection efficiency can, as we will see in this chapter, exceed 40%. Ideally, the light collection (LC), without absorption of photons in the radiator, has an upper limit given by:

$$LC = \frac{K}{1 - r(1 - K)}, \tag{3.10}$$

where r is the reflectivity, and K is the ratio between the total surface and the surface of the photocathodes. The probability P_0 that a photon is detected without any reflection is K, the probability P_1 that the photon is detected after exactly one reflection is equivalent to the probability that the photon does not touch the photocathode $(1-K)$, times the reflectivity r, times the probability that the photon is detected K, i.e. $P_1 = (1-K) \cdot r \cdot K$. The probability that the photon is detected independently of the number of reflexions, is the infinite sum LC:

$$LC = \sum_{n=0}^{\infty} P_n = K \sum_{n=0}^{\infty} \cdot (r(1-K))^n \equiv \frac{K}{1 - r(1 - K)}. \tag{3.11}$$

In the diffusion box design fig. 3.9(b), the radiator is followed by an *integration box* filled with either air or nitrogen. The Čerenkov light yield in air ($n = 1.00028$) is 10^3 better with respect to the same thickness of aerogel. The PMs are mounted on the integration box. The photons travel to the PMs through the air, in which the absorption of light (> 200 nm) is negligible. A diffusive reflector is deposited on the inner walls. A remarkable property of this design is the uniform detection efficiency, which does not depend on the impact coordinates of the incident particle. However, the number of detected photons saturates at some radiator thickness, because the light produced far from the integration box is absorbed by the radiator. A detailed comparison between these two designs is described in [57].

The two options were compared using the cosmic-ray test setup. BIC aerogel tiles ($53 \times 53 \times 23.3$ mm^3) with refractive index $n = 1.05$ were used due to the cosmic muons momentum distribution (fig. 3.7). The aerogel tiles were stacked, each layer consisting of 3×2 (6×2) matrix for the little (big) prototypes. The response for large detectors and smaller refractive indices, as required by the DIRAC-II experiment, is then extrapolated using Monte-Carlo. Four different types of prototypes were built and analyzed:

- a small direct design SD with a cross section of 159 × 106 (H × W) mm^2,
- a small diffusion box design SDB with a cross section of 159 × 106 (H × W) mm^2,
- a large direct design LD with a cross section of 318 × 106 mm^2,
- a large diffusion box design LDB with a cross section of 318 × 106 mm^2,

where the sensitive area is located in the plane perpendicular to the beam. T_{rad}, W and H are used throughout the entire section. For further clarity see table 3.3. For the diffusion design, the depth of the integration box (150 mm) must be added to the thickness T_{rad}, so that finally the total distance in the beam direction is (T_{rad}+150) mm.

Abbreviation	Meaning
T_{rad}	Thickness of the aerogel in the beam direction
H	Height between the two PMs perpendicular to the beam
W	Width of the aerogel, perpendicular to the beam and the height

Table 3.3: Glossary of the abbreviations used in this sections.

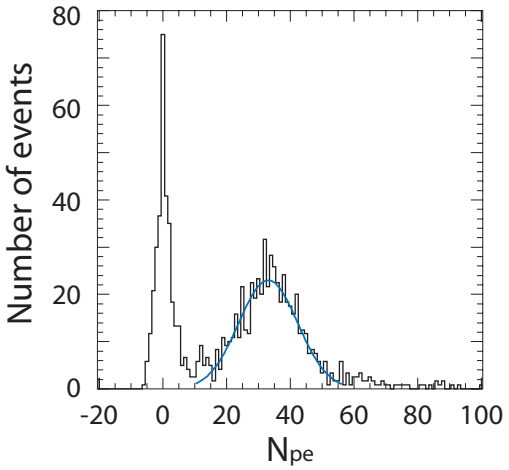

Figure 3.10: Amplitude spectrum obtained from the small direct design (SD) prototype for cosmic muons. A Gaussian fit has been applied to the signal leading to $N_{pe} = 33.6 \pm 1.6$ photoelectrons

The thickness of the aerogel radiator T_{rad} varied in steps of 23.3 mm by piling up tiles. Fig. 3.10 shows a typical amplitude spectrum from the SD design with $T_{rad} = 93.2$ mm for cosmic muons. The amplitude was normalized to the number of photoelectrons (N_{pe}) by the single-photoelectron spectrum obtained with a LED. A Gaussian fit has been applied to the signal leading to $N_{pe} = 33.6 \pm 1.6$. Due to the limited supply of aerogel tiles, the maximum available thickness was 69.9 mm for the long prototypes. The mean number of photoelectrons N_{pe} is plotted in fig. 3.11 as a function of radiator thickness T_{rad} for each prototype. The signals from the two PMs were added to obtain N_{pe}.

The MC simulation based on GEANT4 package [58] was tuned to reproduce the results of the cosmic-ray tests (solid lines in fig. 3.11). The momentum distribution of cosmic muons in fig. 3.7 was implemented in the simulation. MC predictions are used to reproduce the measured N_{pe} and its dependence on T_{rad}. The expected response of the counter for DIRAC-II with refractive index $n = 1.008$ could thus be

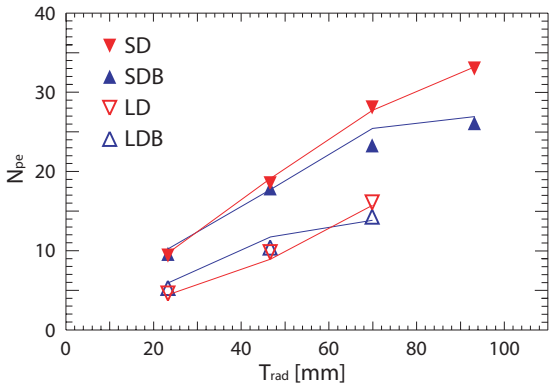

Figure 3.11: Number of photoelectrons N_{pe} as a function of aerogel thickness T_{rad} obtained from cosmic rays and for four different designs: little SD (full-inverse triangle) and big LD (open-inverse triangle) prototypes of the direct design and little SDB (full triangle) and big LDB (open triangle) prototypes of the diffusion box design. The length H of aerogel ($n = 1.05$) is 159 (318) mm for the little (big) designs. The lines show results of simulations.

simulated. The number N_{pe} of expected photoelectrons was simulated for cosmic muons as a function of T_{rad} for an aerogel cross section of 400 (H) $\times$ 150 (W) mm^2 for the direct design and also for the diffusion box design with a 150 mm thick integration box. Fig. 3.12 shows the results. More photoelectrons are detected in the direct design. In the diffusion box design N_{pe} saturates around $T_{rad} = 150$ mm (absorption effects), while N_{pe} still increases in the direct design. As the light yield is the most critical factor in obtaining an efficient K/p separation, the direct design was chosen. N_{pe} shows however a much stronger dependence on the impact coordinate of the incident particles in the direct design.

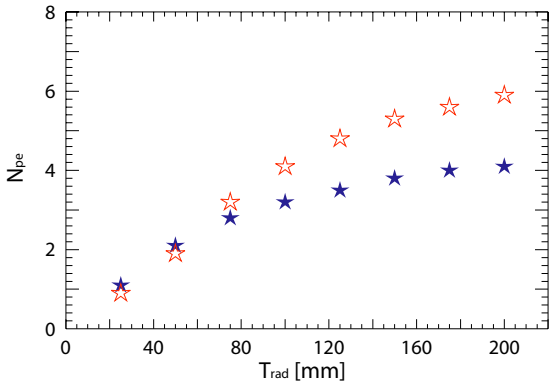

Figure 3.12: Number of photoelectrons N_{pe} as a function of aerogel thickness T_{rad} for cosmic muons (aerogel cross section 400 (H) $\times$ 150 (W) mm^2 and $n = 1.008$). Open stars are for the direct design and full stars are for the diffusion box design.

3.5 Detailed study of the dimensions and of the refractive index

So far, I claimed that the required dimensions are T_{rad} (thickness) $\times$ 15 $\times$ 40 cm^3 and that the index of refraction had to lie between $n = 1.008$ and 1.015. However, this information was based on a first approximation. In this section a precise study is presented, based on simulation and measurements from DIRAC-II.

As mentioned earlier, the goal of the detector is to identify kaons, which come from the desintegration of πK-atoms. These kaons have a flat momentum distribution in the vertical direction, but the intensity increases slowly from top to bottom. The cuts at the edges of the distribution are defined by the acceptance of the DIRAC-II spectrometer. The height of the aerogel detector is given by this vertical kaon distribution and is therefore 420 mm.

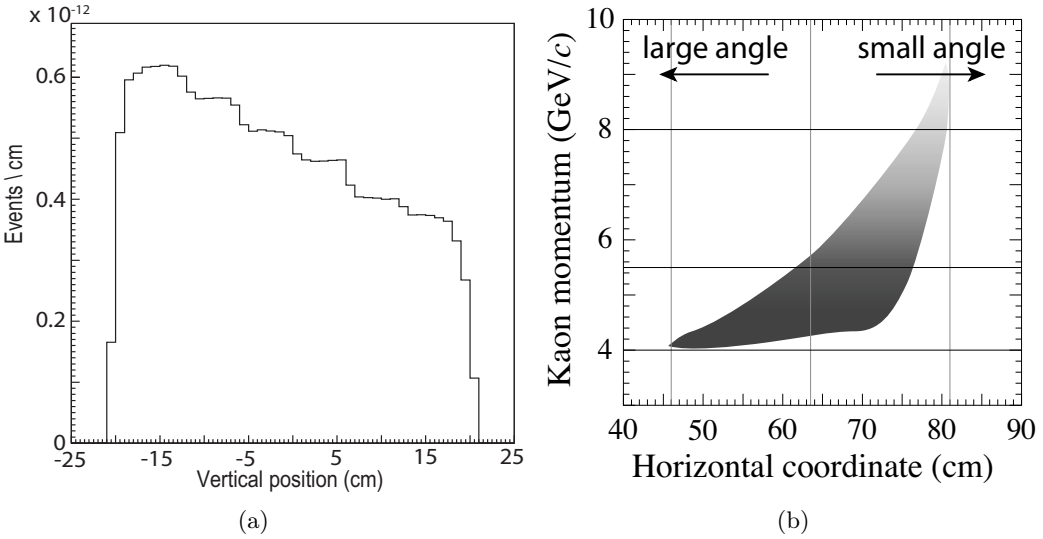

(a) (b)

Figure 3.13: Distributions of kaons from the desintegration of πK-atoms, as a function of the vertical distance (a), and momentum versus horizontal position (b).

The momentum of the kaons emerging from the break-up of πK-atoms is distributed in the range 4 – 8 GeV/c. Due to the deflection angle in the dipole magnet, the kaons are distributed at the location of the aerogel counter over a distance of 350 mm in the horizontal plane. Fig.3.13(b) shows the momentum distribution of kaons from the break-up of πK-atoms as a function of horizontal coordinate [59]. The kaon intensity increases with the decreasing momentum: more than 50% of the kaons are in the range 4 – 5.5 GeV/c and about 70% are in the range 4 – 6 GeV/c. The correlation between spatial and momentum distributions is mainly smeared due to production angle and multiple scattering in the production target. This leads to a large fraction of more abundant low momentum kaons distributed in the inner half of the acceptance, close to the incident proton beam, where the deflection angle

is small. The kaons are distributed over the full momentum range in this region. On the other hand, kaons in the outer half of the acceptance have momenta only in the range 4 – 5.5 GeV/c.

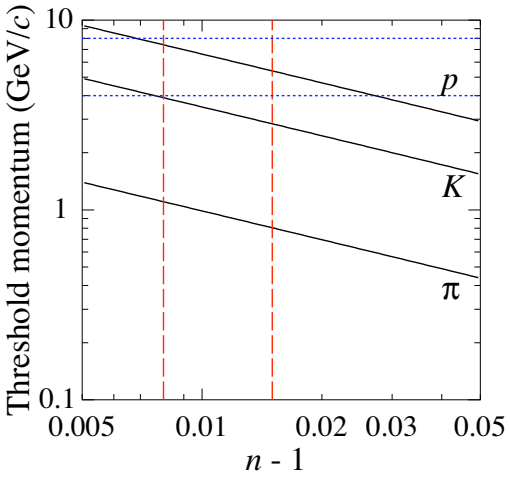

Figure 3.14: Threshold momentum of Čerenkov radiation for protons, kaons and pions as a function of refractive index $(n-1)$. The two horizontal dotted lines are at 4 and 8 GeV/ c, the two vertical dashed lines for $n = 1.008$ and 1.015.

Fig. 3.14 shows the dependence of the threshold momentum for Čerenkov radiation for protons, kaons and pions, as a function of refractive index n. The two horizontal dotted lines at 4 and 8 GeV/c show the range of the momentum for kaons in DIRAC-II. The two vertical dashed lines are at $n = 1.008$ and 1.015: at least two refractive indices should be used for the kaon proton separation over the full momentum range. A small refractive index ($n = 1.008$) is needed to keep protons below their threshold for high momenta. However, low momentum kaons are just above the threshold for such n, leading to a very low light yield. Because kaons populate mostly the low momentum region, a high detection efficiency for such kaons is very important. Therefore, I chose a duplex design with two different refractive indices, each covering either the low or the high momentum region. The basic concept is schematically illustrated in fig. 3.15. The detector consists of three modules having identical geometry: two low-momentum modules so called H1 and H2 to cover the momentum range 4 – 5.3 GeV/c and one high-momentum module (L1) overlapping with H1 to cover the momentum range 5.3 – 8 GeV/c in the inner half of the acceptance. The counting rate for the aerogel counter is expected to be about 10^6/s over the full acceptance, mainly from pions which are much more abundant.

The next task is to determine the optimal index of refraction. As mentioned, two refractive indices are needed for efficient K/p separation in the wide momentum range 4 – 8 GeV/c. The number of expected photoelectrons for kaons and protons was simulated for refractive indices in the range $n = 1.006$ – 1.018. Thereby the

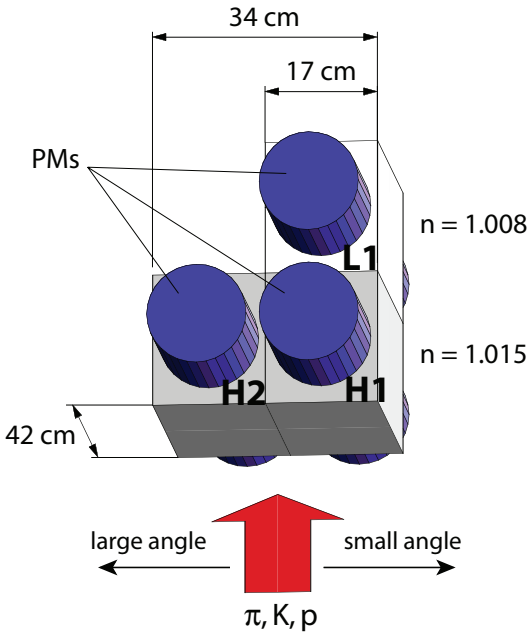

Figure 3.15: Sketch of the final design. The modules H1 and H2 ($n = 1.015$) cover the momentum range 4-5.5 GeV/c and the module L1 ($n = 1.008$) covers the range from 5.5 to 8 GeV/c. The PMs are mounted on the top and bottom surfaces of each module. The sensitive area is 420 × 170 mm^2.

wavelength dependence was assumed to be independent of the refractive index in the modeling of Rayleigh scattering and absorption lengths (fig. 3.3). Fig. 3.16 shows examples of the results for the refractive indices (a) 1.008, (b) 1.010, (c) 1.014 and (d) 1.016. The average number of photoelectrons N_{pe} is plotted as a function of incident momentum for kaons as well as for protons. As mentioned in section 3.4, the light yield of the direct design strongly depends on the vertical impact position. The borderlines show the limiting cases: incident particles crossing near one of the PMs (top borderline) and in the middle of the counter (bottom borderline). The vertical line shown in each plot shows the proton threshold momentum. The small light yield below threshold for protons is due to δ-electrons.

Comparing fig. 3.16(a) and (b), one finds that the refractive index $n = 1.008$ should be used for a clean K/p separation above 7 GeV/c. However N_{pe} becomes too small for aerogels with refractive index $n = 1.006$. The production of such aerogels is also difficult and consequently significantly more expensive. Therefore $n = 1.008$ was chosen for the high-momentum module L1, for which a reasonable efficiency in K/p separation is achieved up to 8 GeV/c. The small amount of detected light can be increased by using a wavelength shifter (section 3.7).

The refractive indices $n = 1.014$ and 1.016 (fig. 3.16(c) and (d)) give a good light yield for kaons and a clear separation from protons in the relevant momentum range of 4 – 5.5 GeV/c. The K/p separation is possible up to the momenta around 6 GeV/c

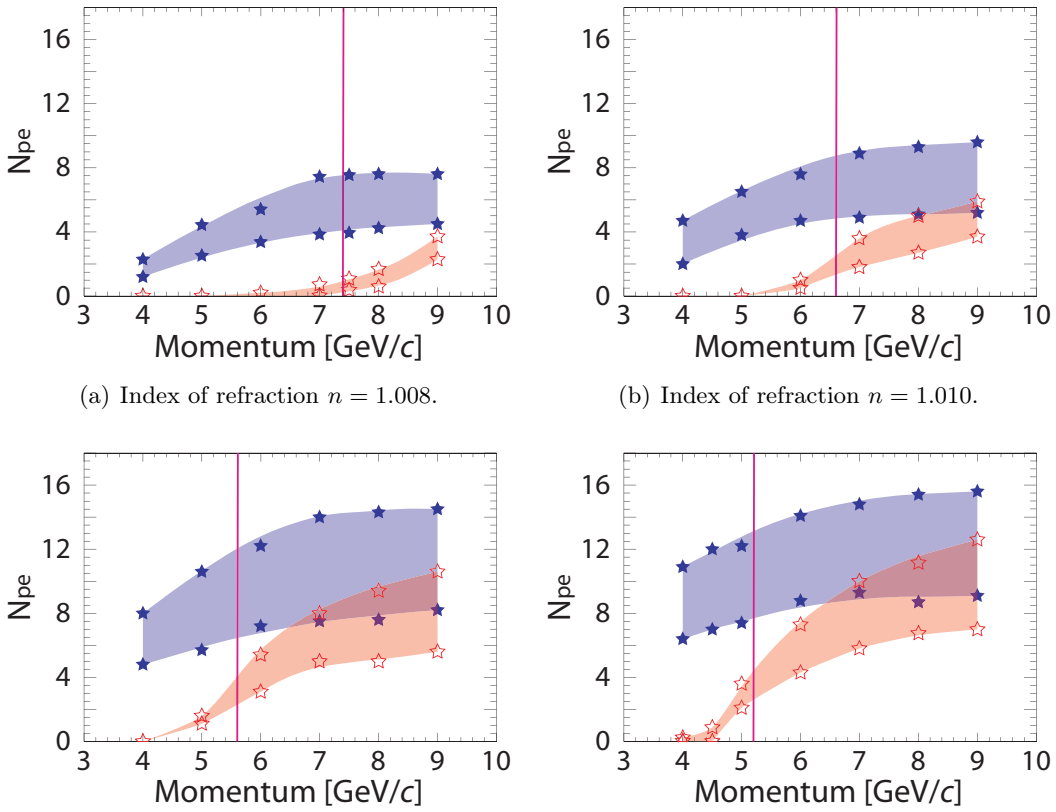

(a) Index of refraction $n = 1.008$.

(b) Index of refraction $n = 1.010$.

(c) Index of refraction $n = 1.014$.

(d) Index of refraction $n = 1.016$.

Figure 3.16: Average number of photoelectrons for kaons (full stars) and protons (open stars) as a function of momentum for the final direct design with a thickness $T_{rad} = 170$ mm.

for these refractive indices. At this momentum both low- and high-momentum modules can be used for the separation, leading to a significant improvement in the separation efficiency. The wide bands in fig. 3.16 due to light attenuation in the aerogel prevent an optimum K/p separation. This can be circumvented with a pyramidal structure of the radiator (section 3.7).

The BIC and the MEW aerogel samples were compared in the cosmic-ray tests. The refractive index was $n = 1.05$ for the BIC and $n = 1.015$ for the MEW samples. I used an aerogel prototype with the small direct design. The sizes of the aerogel stacks were similar, namely 106 (H) $\times$ 106 (W) $\times$ 93.2 (T_{rad}) mm^3 for the BIC sample and 111 (H) $\times$ 111 (W) $\times$ 105 (T_{rad}) mm^3 for the MEW one.

The mean values obtained from the BIC and the MEW samples were 33 and 17 photoelectrons, respectively. To compare the two samples having different n, the number of photoelectrons N_{pe} was normalized to $n = 1.05$ using the approximation $N_{pe} \propto 1 - n^{-2}$ (equ. 3.4). This led to 3.6 ± 0.1 and 5.2 ± 0.3 N_{pe} per cm for the BIC and the MEW samples, respectively. The results indicated a larger light yield

for the MEW aerogel. The degradation of transparency of the BIC samples due to water absorption is a possible explanation for part of the difference. I therefore adopted the $n = 1.015$ MEW aerogel for H1 and H2, which is one of the standard products of MEW and is therefore easily available. In addition, the hydrophobic feature of the MEW aerogels allows for easy handling of the radiator. On the other hand, BIC aerogel with $n = 1.008$ was chosen for L1. The BIC aerogel is reported to have larger scattering and absorption lengths (fig. 3.3) which are crucial features in view of the modest number of photoelectrons expected for L1.

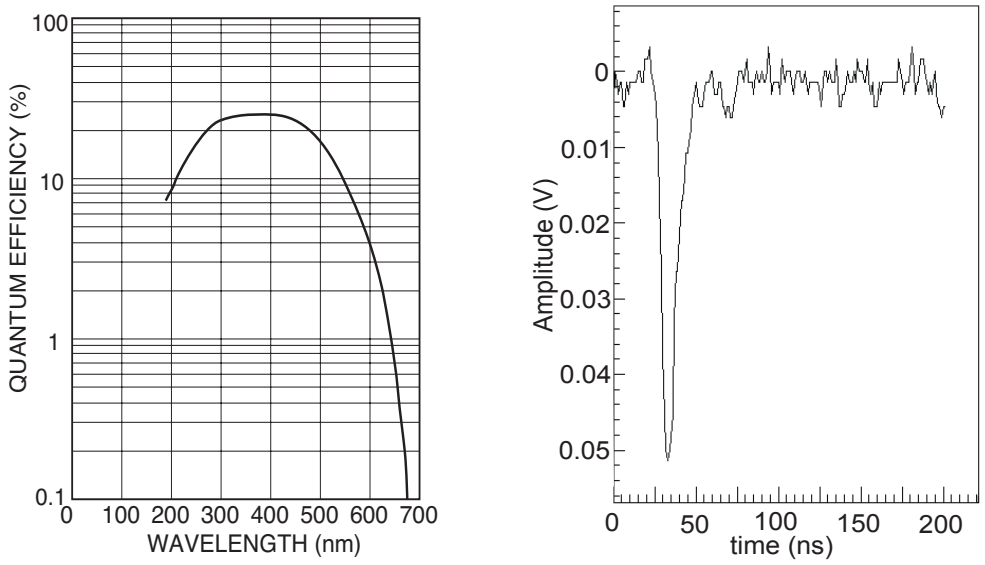

(a) (b)

Figure 3.17: (a): Typical quantum efficiency for a bialkali photomultiplier with a UV-window. (b): Typical single photo-electron pulse taken with a LED from the SN117 (D)-type PM with a bias voltage of V_{bias} = 2000 V.

3.6 The photomultipliers

The counter with the low index of refraction $n = 1.008$ detects only 1 – 6 photons (fig. 3.16) and therefore optimizing every component becomes crucial. Čerenkov light is produced mainly in the UV region. Typical quantum efficiency for a photomultiplier reaches a maximum at 400 nm and a cutoff approximately at 300 nm. With a UV-window, the PM is efficient down to 200 nm and even lower with a quartz window. However, aerogel is not transparent for light with a wavelength shorter than 250 nm (fig. 3.3) and therefore quartz is unnecessary. A typical quantum efficiency as a function of the wavelength for a bialkali PM with a UV-window is given in fig. 3.17(a). Equ.(3.10) leads to the conclusion that a large acceptance is crucial for efficient light collection in aerogel Čerenkov counters. Therefore 5-inch

	PM type	Number of stages	Gain (typ.) $\times 10^7$	Rise time [ns]	Spectral range [nm]	Relative Q.E. (meas.)
A	Hamamatsu R1584 old ver.	14	1.4	2.5	185 – 650	0.75
B	Hamamatsu R1584 new ver.	14	1.4	2.5	185 – 650	1
C	Photonis XP4500/B	10	2	2.5	200 – 650	1
D	Photonis XP4570/B	10	2	4.3	190 – 650	1.2

Table 3.4: Photomultipliers tested in this work.

PMs were chosen as photon detectors. Four different types of 5-inch photomultipliers with a UV window were tested:

- Hamamatsu R1584 old version (A),
- Hamamatsu R1584 new version[3] (B) [60],
- Philips XP4500/B (C),
- Philips XP4570/B (D) [61].

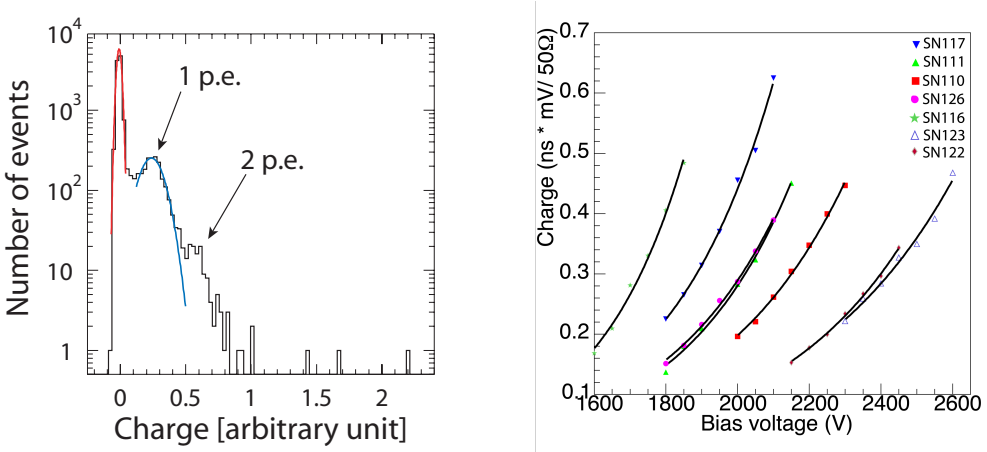

(a) (b)

Figure 3.18: (a): Integrated pulse height histogram for single photoelectrons (p.e.) generated by a LED and detected by the SN117 (D)-type with a bias voltage V_{bias} = 2000 V. (b): Charge vs. bias voltage for the seven (D)-type PMs.

The important parameters are summarized in table 3.4. The single photoelectron peak is clearly separated from the noise in each of the four PMs. The four PMs

[3]Hamamatsu claims that the new version has a photocathode with a higher transmittance in the UV sector. The transmittance as a function of the wavelength is shown in Appendix B for the old and the new versions.

were compared in cosmic-ray tests and the relative quantum efficiency for Čerenkov light was measured with a test aerogel counter. PMs (A) and (D) showed 25% lower and 20% higher quantum efficiencies, respectively, with respect to the otherwise comparable (B) and (C). I therefore opted for (D) which is also significantly cheaper. Seven (D)-type PMs were ordered for the DIRAC-II counter, requesting a selection for cathode blue sensitivity larger than 11 μA/lm to ensure as high quantum efficiency as for the tested sample. The PM with the lowest gain is used as a spear.

A typical pulse is shown in fig. 3.17(b) for the SN117 (D)-type PMs. To count the number of photoelectrons it is important to determine the integrated pulse height or charge for one photon. To do so, a 400 nm LED located in the outer box was supplied with very short pulses generated by a pulse generator. The pulses were also used as trigger signals for the oscilloscope. To avoid contamination from two or more photoelectrons the amplitude of the pulses was reduced so that the signals were detected with only 5% probability in each PM. The probability for two or more photoelectron events was then 0.13%. The single photon spectrum is shown in fig. 3.18(a).

The charge of one photoelectron as a function of the bias voltage V_{bias} has been measured for all seven PMs in order to get a correct calibration. The results are shown in fig.3.18(b). The two PMs with the highest gain are used for the counter with the aerogel $n = 1.008$ because of the low number of expected photoelectrons. The PM with the lowest gain is used as a spear.

3.7 New designs

3.7.1 Pyramid design

Another critical issue for efficient K/p separation is the strong dependence of the light yield on the impact coordinate of the incident particle in a large counter (section 3.5). This effect can be compensated by adding aerogel tiles at the centre of the detector (fig. 3.19). The pyramid design was simulated for the full size detector assuming a refractive index $n = 1.05$. The number of photoelectrons is plotted in fig. 3.20 as a function of impact coordinate for:

- (a) a rectangular solid shape (blue triangles) of size 420 (L) × 170 (W) × 170 (T) mm^3,
- (b) additional tiles in pyramid configuration at ±50 mm and ±100 mm (red crosses) with two 20 mm layers (dark area in fig. 3.19).
- (c) the pyramid design (green squares) with an additional layer 20 mm at ±150 mm to (b) (light area in fig. 3.19).

The bumps in fig. 3.20 are due to the sudden change of radiator thickness. The pyramid design clearly improves the uniformity in light yield. With the three step

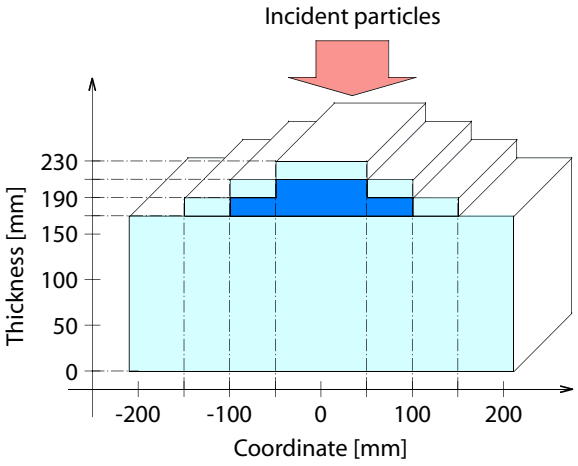

Figure 3.19: Pyramid design: the thickness increases in the middle to compensate for absorption in the aerogel. Photomultipliers are at the left and right.

pyramidal structure, the variation of N_{pe} over the full length is reduced from 40% to 15%. Note that the orientation of the pyramid (upstream or downstream side) is irrelevant since photons are diffused. Both orientations were in fact simulated and there were no differences in the light yield.

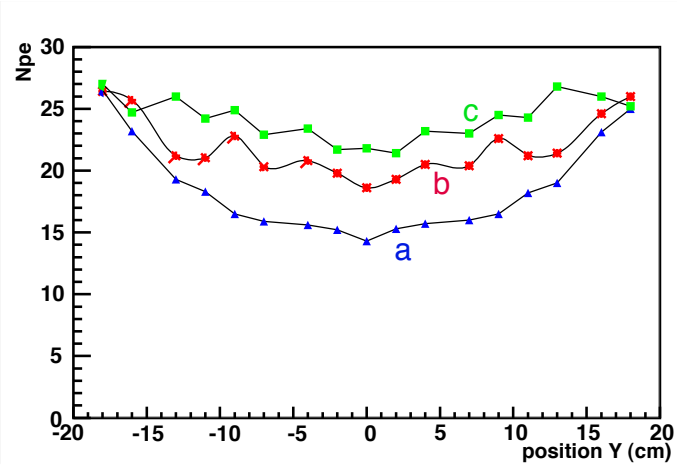

Figure 3.20: Number of photoelectrons N_{pe} as a function of position for the $n = 1.05$ aerogel. The blue line (a) is for the direct design with a thickness $T_{rad} = 150$ mm without additional layers. In red (b) is the pyramid design with two layers of thickness 20 mm each and in green (c) the pyramid design with three additional layers (fig. 3.19).

3.7.2 Sandwich design

The simulation plotted in fig. 3.16a) shows that for the direct design with the final size of 170 (T_{rad}) × 170 (W) × 420 (H) and an index $n = 1.008$, the number of photoelectrons are on average between one and six depending on the momentum and the impact position.

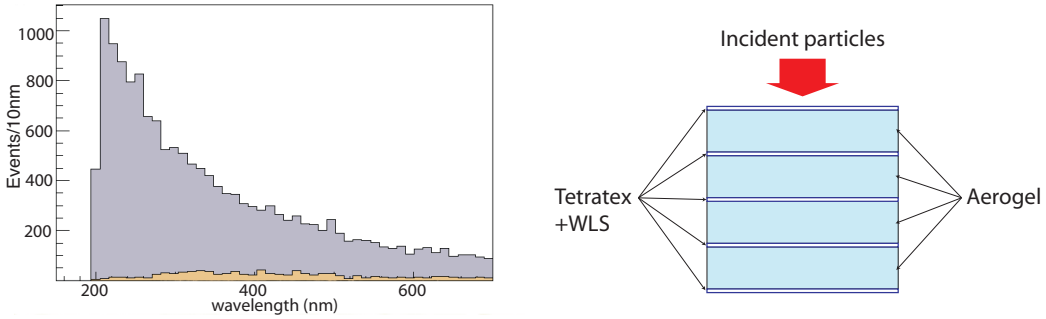

(a) (b)

Figure 3.21: (a): Čerenkov light distribution in grey and photons reaching the two PMs in brown. (b): Sketch of the sandwich design. Layers of aerogel tiles are separated by Tetratex coated with a wavelength shifter (WLS).

The number of Čerenkov photons is proportional to $\frac{1}{\lambda}$ (equ. 3.4). Thus the main part of the light is in the UV region. Fig. 3.21(a) shows the number of produced Čerenkov photons in grey and the number of photons reaching the PMs in brown. This plot has been simulated. The distribution is cut at 200 nm, since aerogel is not transparent anymore for shorter wavelength. Only a small fraction of the UV-light reaches the PM. The aim of this design is the conversion of the abundant UV-photons from Čerenkov radiation to longer wave lengths and therefore to take advantage of larger absorption length (fig. 3.3), which increases rapidly from 10 cm at 270 nm to 3 m at 350 nm. Furthermore longer wavelengths provides a better matching to the PM sensitivity. Fig. 3.21(b) illustrates the concept of the sandwich design incorporating a wavelength shifter (WLS). Tetratex reflector foils coated with WLS and layers of aerogel tiles are alternately stacked in the direction of the incident particles. The gap between the foils has to be smaller than the absorption length, i.e. of the order of a few cm.

The sandwich design was tested in the cosmic ray setup using a small direct design container filled with BIC $n = 1.05$ aerogel. Three Tetratex foils coated with WLS were inserted between four layers of 23.3 mm thick aerogel tiles. Tetratex foils covering the inner walls of the container were also coated with WLS. Various WLS materials were tested, such as POPOP, tetraphenylbutadiene (TPB) and p-terphenyl (pT). Three different techniques were investigated to deposit the WLS: (A) dissolving the WLS in a solvent and spraying the solution on the foil, (B) immersing the foil in the solution, or (C) evaporating the WLS on the foil in vacuum. In the methods (A) and (B) the solution slowly evaporates and the WLS forms a thin

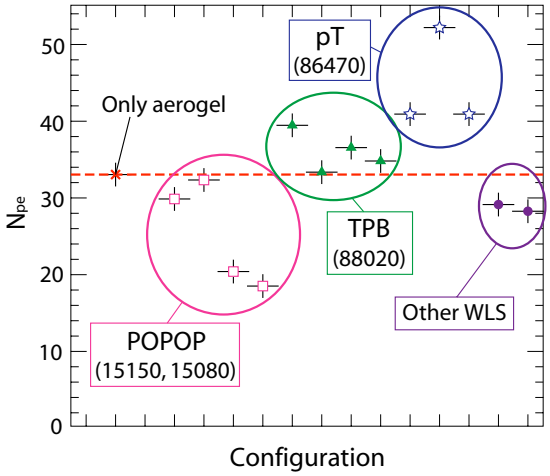

Figure 3.22: Comparison of light yield in the sandwich design with the BIC $n = 1.05$ aerogel for various configurations (WLS, solvents and coating techniques). The numbers below the WLS names show the chemical identifications.

layer on the reflector surface. In general (B) gives a more uniform coating than (A). Different solvents such as cyclohexane, tuluol, chloroform, and dichloromethane were studied to increase the concentration of WLS, in particular of pT, which was hard to dissolve. The maximum concentration was obtained with chloroform as solvent. Fig. 3.22 shows the average number of photoelectrons for various configurations (different solvents and coating techniques). The dashed line shows the reference value obtained without WLS on the Tetratex. Tetratex foils with WLS were also tested without aerogel but no light yield could be observed within the measurement precision.

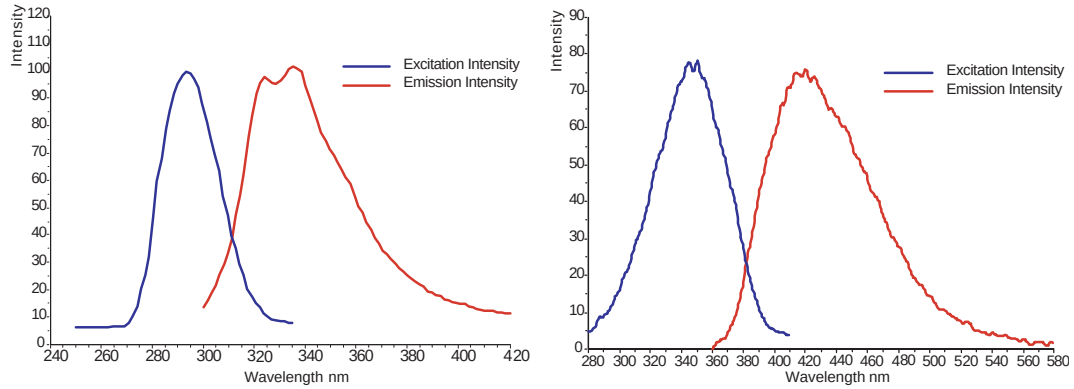

(a) (b)

Figure 3.23: Absorption and emission spectra for two different wavelength shifters. (a): p-Terphenyl (pT) and (b) Tetraphenylbutadiene (TPB) [62].

The immersing technique consistently showed better results than spraying. Configurations with TPB and especially pT showed positive results. The best result, 50% increase in yield, was obtained with pT dissolved in chloroform and with the immersing technique. The peak absorption and emission for pT (TPB) are at 290 nm (340 nm) and 330 nm (420 nm), respectively (fig. 3.23). The peak emission for TPB matches the peak sensitivity of the PMTs. Its peak absorption is in the region where the absorption length of aerogel is already of the order 1 m. However, for pT the absorption length is 35 cm at the absorption peak and about 2 m at the emission peak. Since Čerenkov photons are much more abundant at shorter wavelength, this is the likely explanation for the better results obtained with pT. The evaporation technique of the WLS layer has the advantage of being more controllable. However, the adherence of pT to Tetratex is poor. TiO_2 paint can be coated by pT by evaporation. However, I could not obtain satisfactory results, possibly due to the worse reflectivity of TiO_2 paint. I therefore opted for Tetratex foils immersed in a solution of pT dissolved in chloroform for the final detector construction. A picture of these foils illuminated with a 250 nm UV-lamp is shown in fig. 3.24.

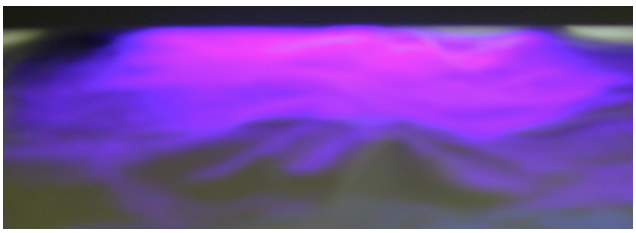

Figure 3.24: p-terphenyl applied on Tetratex and illuminated with a 250 nm UV-lamp.

3.8 Assembly of the final design

Fig. 3.25 shows an overview of the final detector. For the mechanical drawings I refer to Appendix C. Aerogel is well known to be fragile. For this reason a 0.5 mm thin inner box (fig. 3.26(a)) was developed to simplify the placement of the aerogel inside the detector. Furthermore, Tetratex is made of teflon and therefore cannot be glued on the inner walls of the box. A mechanical system (fig. 3.26(b)) has to hold and place the foils against the inner walls. For a better reflectivity two layers of Tetratex are superposed.

Once the Tetratex is fixed one can start filling the boxes with the aerogel tiles. The configuration of the aerogel blocks is shown in fig. 3.27. Note that, like in a brick wall, the gaps between two pieces are always shifted compared to the precedent layer. The total volume is 24 ℓ for H1 and H2 together and 13.4 ℓ for L1. Table 6.1 summarized the configuration of the aerogel counter. The pyramid design was implemented to both modules with three layers at ± 55, ± 111 and ± 166 mm (in steps of 42 mm thickness) for the low and at ± 53, ± 106 and ± 159 mm (in steps

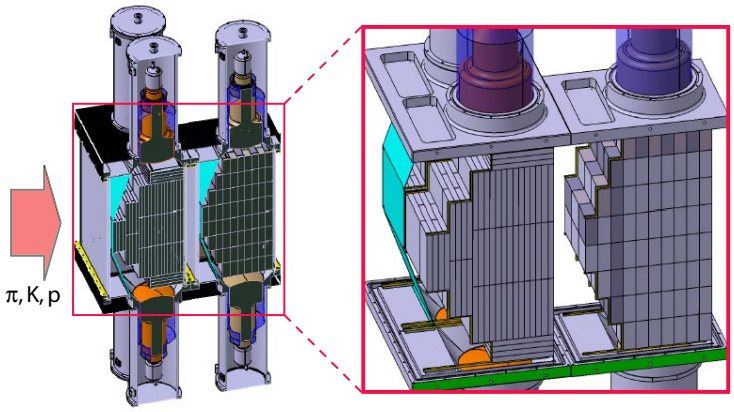

Figure 3.25: Overview of the final detector. Right: Close-up view of the inner part.

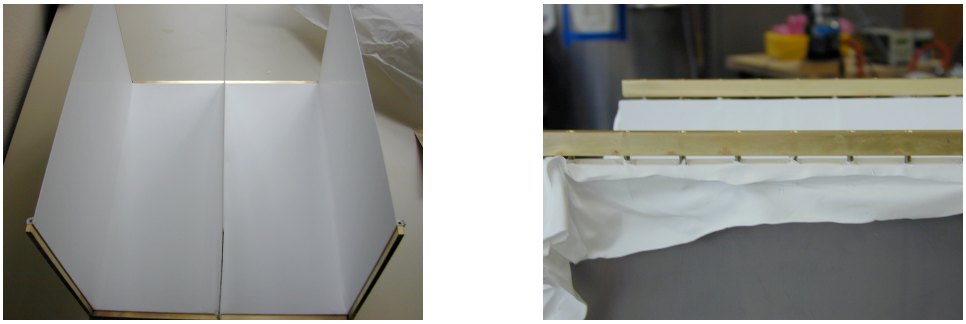

(a) (b)

Figure 3.26: (a): The inner box of H1 and H2 modules. (c): Frame holding and stretching the Tetratex against the inner walls.

of 23.3 mm) for the high-momentum module. The dimensions were determined by the sizes of the tiles from MEW and BIC. The larger step thickness for the low-momentum modules was chosen due to the shorter absorption length for the MEW aerogels.

The most difficult part from the mechanical point of view was the construction of the aerogel support, which should hold together all the aerogel tiles without applying to much pressure due to the fragility of aerogel. Furthermore, especially for the aerogel from Panasonic, large uncertainties on the size of one tile result in variations on the total length of the aerogel radiator in the order of centimeters. The frame should therefore be adjustable to fit the aerogel shape. The support consists in a 3 mm thick aluminum frame with a waving of a 100 μm wire. A picture is shown in fig. 3.28(a). The frame is painted in white with TiO_2, a diffusive reflector, to avoid light absorption. In fig. 3.28(b) and fig. 3.28(c) are shown a photo of the inner box filled with aerogel tiles confined by its support for the $n = 1.015$ and

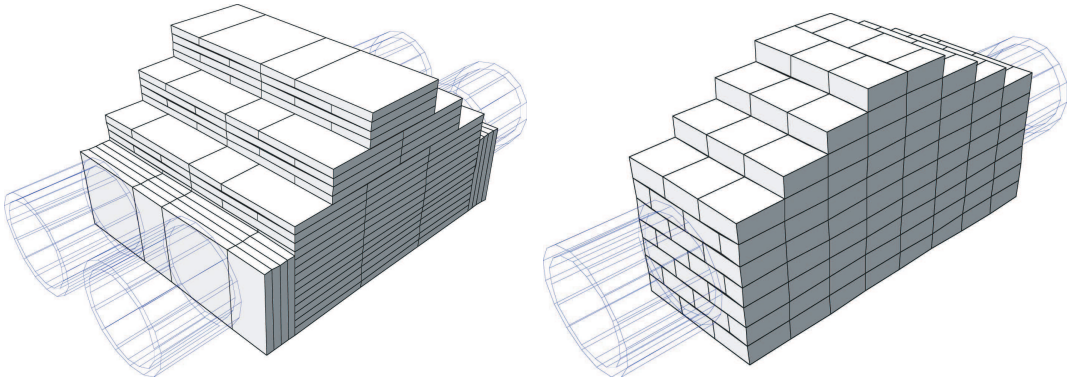

(a) (b)

Figure 3.27: Configuration of the aerogel blocks, (a) for the H1, H2 modules and (b) for the L1 module.

	L1	H1 and H2
Refractive index	1.008 ± 0.0004	1.015±?
Aerogel type	BIC	MEW
Number of aerogel pieces	124	172
W × H × ($\mathrm{Th}_{rad}^{min} - \mathrm{Th}_{rad}^{max}$) ($\mathrm{mm}^3$)	159×424×(163.1-233.)	333×417×(111-231)
Aerogel volume	13.4ℓ	24ℓ

Table 3.5: Properties of the aerogel radiator for modules H1, H2 and L1.

$n = 1.008$ detector respectively. For the latter, one can see also the Tetratex foils coated with WLS stacked in between aerogel layers. Fig. 3.28(d) is a picture of the inner box filled and already closed by the main support. The little wires visible on the photo are the only matter in between the aerogel and the PMs.

The filled inner box is then slid inside the external gas tight box made of 1,5 mm thick iron (fig. 3.28(e)). The aim of this outer-box is to protect the hydrophobic $n = 1.008$ aerogel from humidity and also to cancel out the magnetic field inside the box from the spectrometer magnet and from the earth. In fact large area PMs are very sensitive to magnetic fields (section 4.2). The relative output as a function of the magnetic field is shown in Appendix B.2.

The main support is the central part of the mechanical structure, which is mounted gas tightly using an O-ring system on the external box (fig. 3.28(f)). The inner structure of the main support has been designed to guide the light towards the PMs.

The main support consists of an aluminum block surrounded by a 1 mm thick iron layer for the magnetic field. The aluminum block has been excavated and polished to optimize the light collection. A thin aluminum and MgF_2 layer has been evaporated under vacuum (at CERN) on the light guide to improve the reflection. The peak of maximal reflectivity has been chosen to coincide with the emission spectrum of the WLS .

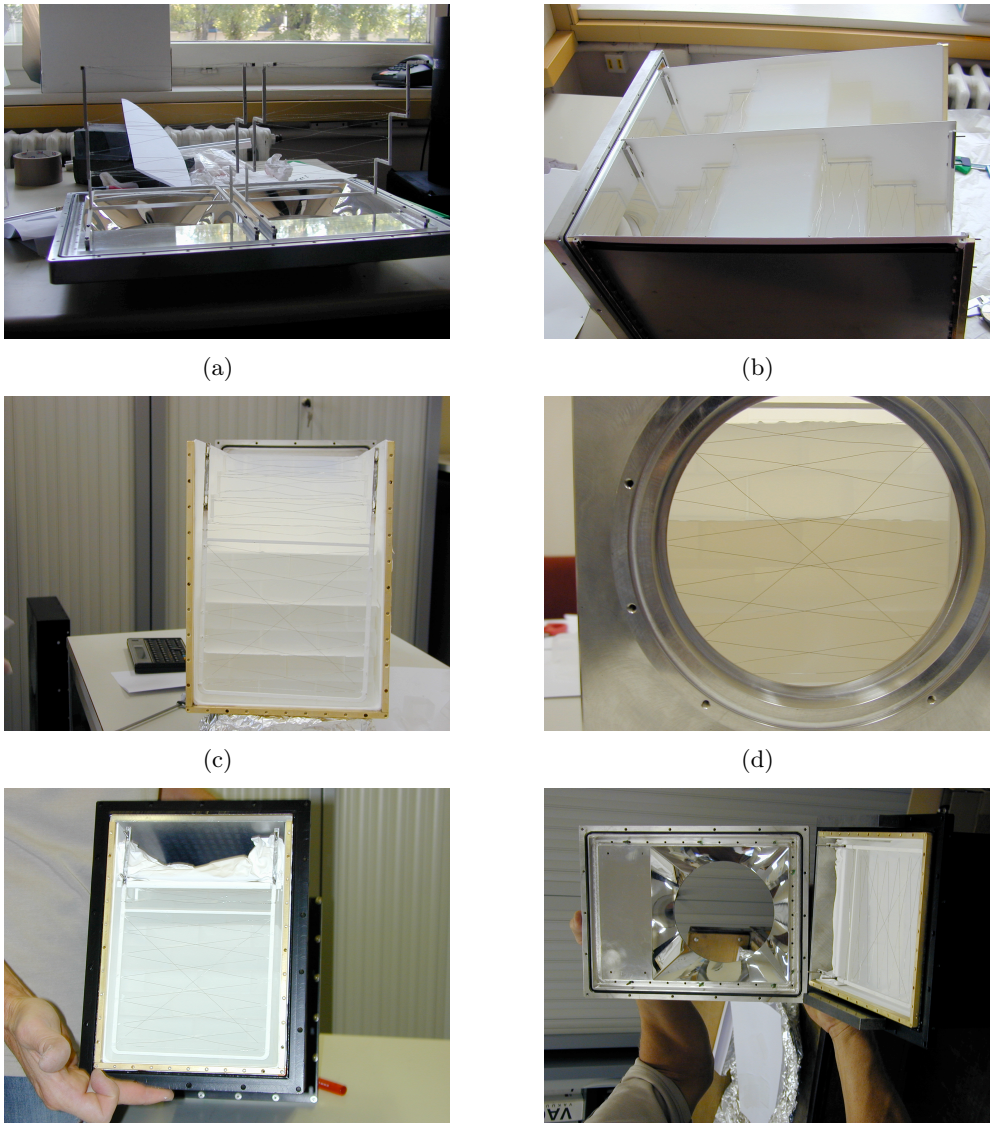

(a) (b) (c) (d) (e) (f)

Figure 3.28: (a): The aerogel holder consists in a step like structure with waving of a 100 μm wire mounted on the main support. (b): Inner box for the two $n = 1.015$ modules filled with aerogel tiles which are hold together by its support. (c): same as (b) but for the $n = 1.008$ detector. (d): Picture of the closed inner box. The wires from the aerogel support is the only material between the aerogel and the PM (visible). (e): Inner box filled with aerogel protected by the (black) outer-box for the L1 module. (f): Main support just before being mounted on the L1 module. Note the mirror for high light collection efficiency.

Chapter 4

Performance of the aerogel Čerenkov detector

Measurements with different levels of precision have been performed in order to analyze the response of the aerogel detector and its efficiencies. In a first step, a cosmic rays test was performed for a rough estimate of the average number of photoelectrons. A second test was done in the DIRAC-II environment to analyze the aerogel modules in real beam conditions, taking into account the magnetic field of the spectrometer and the high beam intensity. Finally, during the 2007 run the whole DIRAC-II spectrometer could be used for a precise study of the detector response as a function of momentum, impact position and particle type. During the latter analysis different triggers were used: the minimum bias trigger for a study of the relative number of detected particle types and the usual DIRAC-II mixed trigger which is the one also used for the πK-atoms search.

4.1 Test with cosmic rays

Before the installation of the detector in the DIRAC-II area a cosmic ray test was performed to measure the pulse height spectrum for the final detector. The three scintillators S_1, S_2 and S_3 (placed under the lead absorber) used for the trigger as well as the DAQ (oscilloscope LeCroy Wavesurfer 454) were taken from the cosmic test setup (section 3.3). For L1 the cosmic muons need a momentum higher than 0.85 GeV/c to be above the Čerenkov threshold. A lead thickness of almost half a meter is needed to absorb less energetic muons leading to a strong decrease in the counting rate due to the tighter restriction in the solid angle acceptance. Furthermore, the intensity of muons above the threshold decreases rapidly [63]. Therefore, only H1 and H2, the two modules with the heavy refractive index, were tested. The detector was installed between two scintillators S_1, S_2 (10×10 cm^2) , see picture 4.1 and S_3 was placed under 0.4 m of lead. The counting rate was $5 \cdot 10^{-3}$ Hz.

Fig. 4.2 shows the integrated pules height spectrum for cosmic muons for the $n = 1.015$ module H1. The signals from the two PMs were added and converted into the

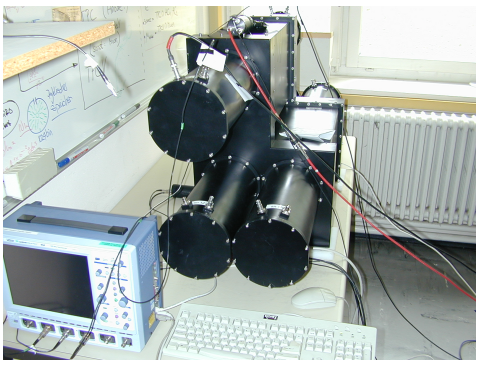

Figure 4.1: Detector during the cosmic ray test in the laboratory.

number of photoelectrons, N_{pe}. Fig. 4.2(a) was obtained with the two scintillators placed near one of the PM and fig. 4.2(b) half way between the two PMs. The mean value of photoelectrons obtained from a Gaussian fit was 6.4 for both spectra, indicating that the average number of photoelectrons is independent of the impact position of the incident particle, as expected for the pyramid design. Assuming that the incident cosmic muons have an average momentum of 1 GeV/c [63], one obtains 10.0 ± 0.9 photoelectrons for $\beta \approx 1$ and hence 4.8 ± 0.5 photoelectrons for kaons at 4 GeV/c.

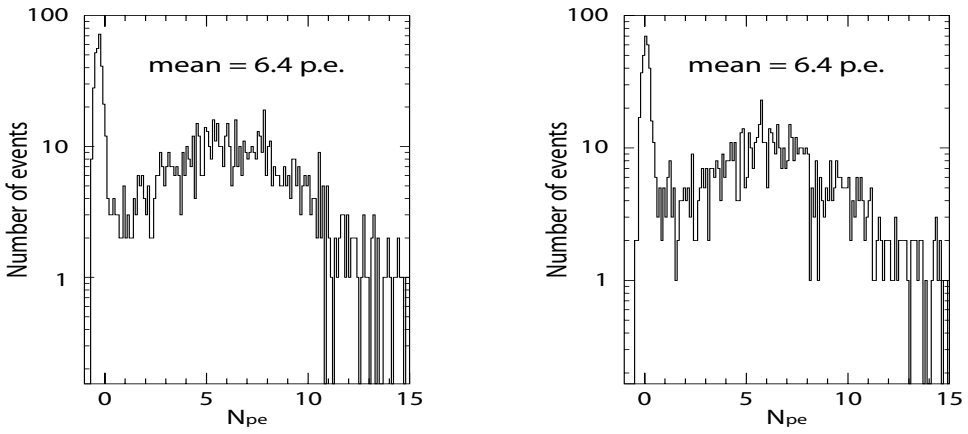

(a) (b)

Figure 4.2: Integrated pulse height spectrum for H2 collected with cosmic ray muons crossing the detector near one of the PM (a) and in the middle between the two PMs (b). The horizontal axis is calibrated and scaled in number of photoelectrons N_{pe}.

Similarly, for H1 one obtains a light yield independent of the impact position and with a mean value of photoelectrons of 11.1 ± 1.0 for $\beta = 1$ leading to 5.5 ± 0.5 for kaons at 4 GeV/c. This difference in the light yield between H1 and H2 can be

partly explained by a variation in the quantum efficiency of the PMs.

4.2 Test with beam

At the beginning of 2007, after installation of the counter in the DIRAC-II experimental area (fig. 4.3), a one week test was performed using the 24 GeV/c proton beam from PS synchrotron on a 94μm Ni target. The aim was to analyze the performance of the detector and to measure the influence of the spectrometer magnet on the efficiency of the photomultipliers. The dipole magnet was first switched off. Unfortunately, due to the update of the electronics, I could not use the existing DAQ and trigger but I had to build my own ones.

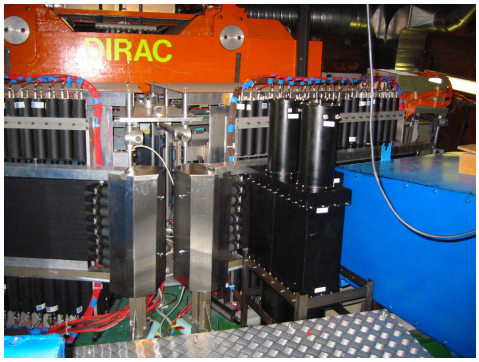

Figure 4.3: Detector (in black on the right) after installation in the DIRAC-II area.

For the DAQ, I used a LeCroy WavePro 7100 oscilloscope in segmentation mode[1]. For the trigger, I used in coincidence the signal from the beam spill, the signal from the vertical hodoscope (VH) slabs 18+19 and the signal from the PSh detector slab 19 for a rough tracking. In addition I used the N_2-Čerenkov detector (Ch) in the left arm in coincidence to select $e^{\pm}$. The configuration can be written as

$$\text{Spill} \bigcup \text{Ch} \bigcup \text{PrSh}_{\text{Slab19}} \bigcup \text{VH}_{\text{Slab18+19}} \ . \tag{4.1}$$

A typical integrated pulse height spectrum measured with H1 is shown in fig. 4.4 for $\beta = 1$. The average number of photoelectrons (N_{pe}) resulting from a Gaussian fit (in red) is 10.4 ± 0.7. For H2, one obtains similarly 9.4 ± 0.7 photoelectrons. For both modules, the N_{pe} are in good agreement with the estimations from the cosmic ray test.

To evaluate the influence of the fringe fields from the spectrometer magnet on the PMs, I repeated the measurement with the magnet switched on. Only positive

[1] In segmentation mode the oscilloscope kept 200 pulses in memory before writing them to the hard disc.

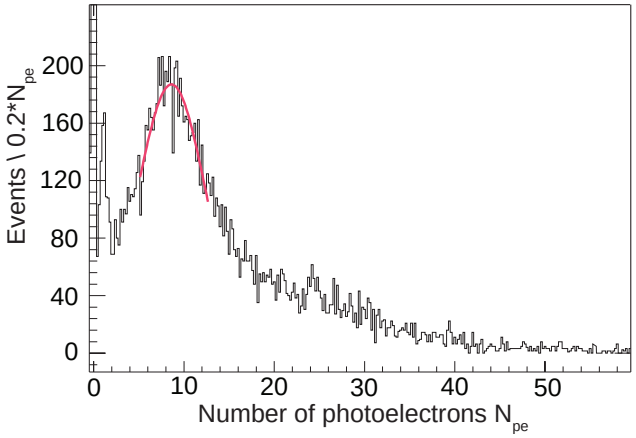

Figure 4.4: Integrated pulse height spectrum measured with H1 for $e^{\pm}$ and with the spectrometer switched off.

e^+ should cross the aerogel detector now. The PMs became inefficient and only 10% of the expected N_{pe} could be measured. The issue was solved by surrounding the whole detector with a 1 mm thick box of μ-metal. In this configuration I measured the average number of photoelectrons for H1 and H2 leading to $N_{pe} = 9.8 \pm 0.6$ and $N_{pe} = 8.7 \pm 0.5$ respectively, a 5 – 10% shift compared to what had been measured with the magnet switched off. The width of the distribution becomes somewhat larger under the influence of the magnetic field. To get a rough approximation of the losses, the number of events in the pedestal and in the signal region are counted with and without magnetic field and rescaled to the same total number of entries. With the magnet switch on, the number of events in the pedestal increases by 48 for 10‘000 events in the signal region, which represents an effect of less than 0.5%. For L1, the effect from the magnetic field is somewhat stronger. The N_{pe} decrease by 15% from 5.6 ± 0.5 to 4.8 ± 0.5.

4.3 The 2007 DIRAC-II run

In this section, the entire setup is used. One can take advantage of the existing DAQ, triggers (section 2.4), the response of all detectors and Ariane, the track reconstruction software (section 2.5).

4.3.1 Calibration using electron-trigger

The electron trigger (section 2.4) uses the Ch detectors in coincidence to select positrons in the left arm where the aerogel detector is located and electrons in the right one, provided that the spectrometer magnet is switched on. Due to their light masses ($\beta = 1$), the Čerenkov light yield is maximum for positrons, which provides a good tool for calibrations. With the offline tracking, one can now determine the

exact impact position of the particle at the entrance window of the aerogel counter. The three modules are therefore scanned in horizontal and vertical direction. As expected, the detector response does not depend on the horizontal coordinate. Fig. 4.5 shows the correlation between the mean ADC channel resulting from a Gaussian fit and the vertical coordinate for the three modules (H1, H2 in black and L1 in red). The flat black distributions reflect the success of the pyramid design. For L1, the strong y-dependence, even with the pyramid-design, leads to the conclusion that the WLS may decrease the reflectivity of the Tetratex foils. This effect has not been observed for the different prototypes used in the cosmic ray test setup. For detectors with a small distance between the PMs, the light yield should depend much less on the reflectivity than for large distances, as is the case for L1.

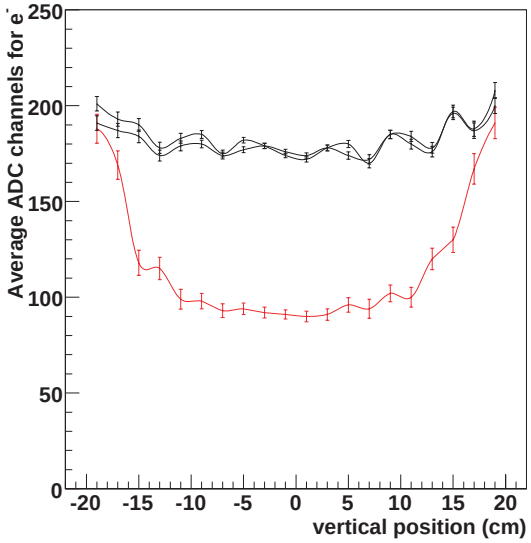

Figure 4.5: Average number of ADC channels for each of the 3 modules vs. vertical position. In black H1, H2 and in red L1. The measurements have been done in beam using positrons with $\beta = 1$.

Module	Refractive index	Average number of photoelectrons
H1	1.015	$9.5 \pm 0.3 - 10.4 \pm 0.3$
H2	1.015	$8.8 \pm 0.2 - 9.6 \pm 0.3$
L1	1.008	$4.4 \pm 0.3 - 7.9 \pm 0.4$

Table 4.1: Average number of photoelectrons for the three modules; the lower number corresponds to a track crossing the center of the module and the larger one to a track close to one of the PMs.

To convert ADC channels to N_{pe}, one can either convert the charge measured with the LED in the laboratory to ADC channels, or crosscheck this calibration by selecting tracks crossing the detector very close to one PM and reading out the signal with the opposite PM. I took advantage of the strong absorption in aerogel so that mainly pedestal and single photons are detected. Fitting the distribution, the number of ADC channels for one photoelectron could be extracted for each PM, see fig. 4.6. The N_{pe} for $\beta = 1$ and for each module are summarized in table 4.1; the lower number corresponds to a track crossing the center of the module and the greater one to a track close to the PMs.

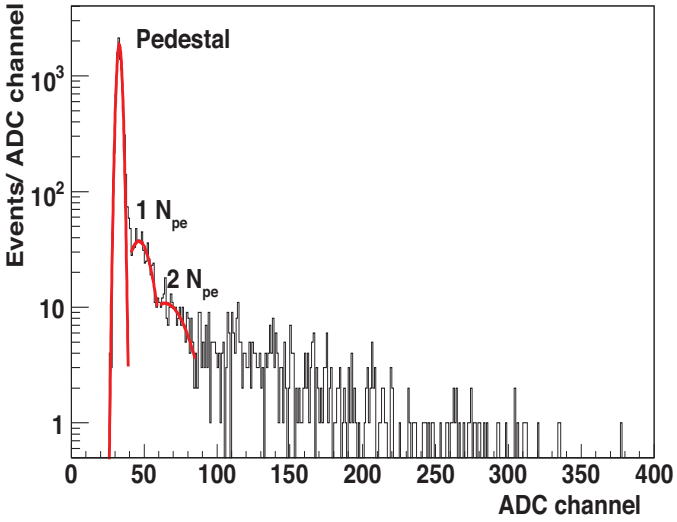

Figure 4.6: Typical single photon ADC distribution used for calibration.

4.3.2 Pion-trigger

The pion trigger rejects electrons and positrons using Ch in anti-coincidence and selects symmetric tracks with the same aperture in each spectrometer arm (section 2.4). Mainly pions and protons are present in the left arm as well as a few kaons. For tracks crossing H1, the scatterplot fig. 4.7(a) clearly shows the presence of pions in the green ellipse. Protons above threshold are shown in the red ellipse, while protons below threshold are in the pedestal. Nevertheless, a few protons give some light due to accidental tracks, thermal photoelectrons or δ-electrons produced in the aerogel [65] or elsewhere (blue ellipse).

The proton distribution below the Čerenkov threshold consists therefore not only in pedestal but also in a positive tail which has to be included. Kaons are diluted in the pion and proton background due to their strong suppression [64]. Fig. 4.7(b) shows the integrated pulse height spectrum measured with H1 for pions selected with the heavy gas detector (ChF) in coincidence.

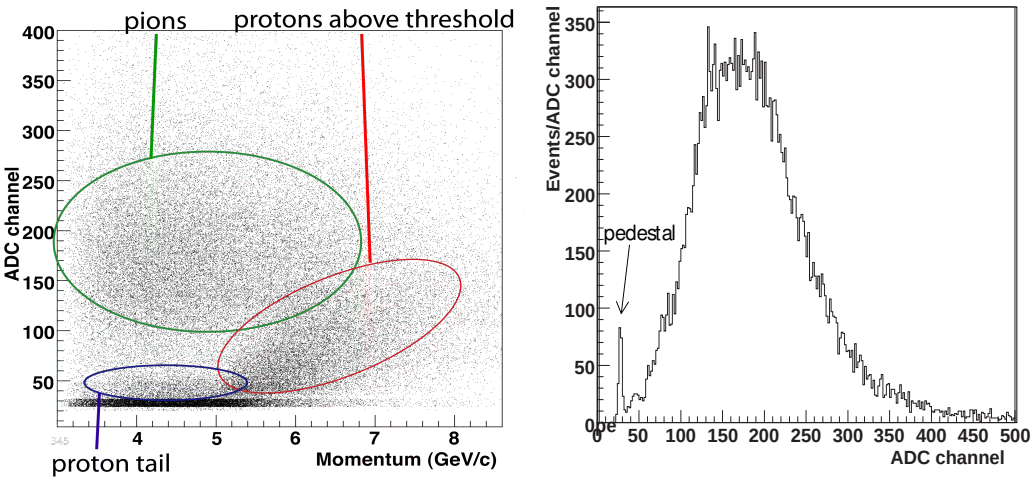

(a) (b)

Figure 4.7: (a): Scatterplot for H1. The pions are surrounded in green, the protons in red and the tail from pedestal in blue. Due to the low production rate, kaons are not visible in this plot. (b): Integrated pulse height spectrum measured with H1 for pions selected with the ChF in coincidence.

4.3.3 Minimum bias trigger

To compare the relative number of detected kaons and protons with results from other experiments [64], I used the minimum bias trigger. This trigger only requires a hit in the vertical and horizontal hodoscope of the left spectrometer arm, and the relative number of particles are hence not biased. I ran the experiment with both polarities of the spectrometer magnet to analyze positive and negative particles in the aerogel detector. For the following analysis, Ch and ChF are used in anti-coincidence. Only protons and kaons are accepted. Also, the track is required to cross the selected aerogel module.

Negative polarity

With this polarity negative particles, i.e. antiprotons and negative kaons cross the aerogel detector. The ratios of kaons over antiprotons at the target ($K^-/\bar{p}$) have been measured [64], with a 24 GeV/c proton beam for different targets, momenta and angular ranges. For the conditions in DIRAC-II experiment, at the target the ratio $K^-/\bar{p}$ should be between 6 – 7 for 4 GeV/c and 5 – 5.5 for 7 GeV/c.

This ratio can be measured by counting the number of events in and above the pedestal, for a momentum range where antiprotons are below the Čerenkov threshold. One assumes that the fraction of antiprotons giving signal (δ-electrons, accidentals,..) is negligible. Antiprotons are stable, but kaons are decaying. Therefore, the number of detected kaons has to be corrected in order to get the number at

Momentum (GeV/c)	$N_{\bar{p}}$	N_{K^-}	$K^-/\bar{p}$ measured	$K^-/\bar{p}$ expected [64]
3.75-4.25	276	1873	6.8	6-7
6-8	266	1540	5.8	5-5.5

Table 4.2: Expected and measured relative number of antiprotons and negative kaons at the target.

the target. The fraction to add can be extracted from fig. 3 in [66]. The measured and expected numbers are summarized in table 4.2. According to [64], the ratio between the number of protons and kaons is more than twenty times higher than for antiprotons and kaons. The signal over background ratio is hence much higher and the kaon distribution is not diluted anymore. Therefore, the kaon spectrum can be measured directly with H1, H2 and L1 (fig. 4.8). For histogram (a) and (b) particles with a momentum between 3.75 and 4.25 GeV/c are selected and for the histogram (c) particles between 6 and 8 GeV/c. Particles with low momenta are more abundant and hence the momentum range could be smaller for H1 and H2. A Gaussian fit has been applied in red leading to $N_{pe} = 5.5 \pm 0.2$ for H1, $N_{pe} = 4.5 \pm 0.2$ for H2 and $N_{pe} = 3.3 \pm 0.4$ for L1. According to equ.(3.4), kaons with a momentum of 4 GeV/c should give 50% of Čerenkov light at saturation in H1 and H2 leading to respectively 11 and 9 N_{pe} for $\beta = 1$. In L1, kaons with an average momentum of 7 GeV/c should be at 70% of the Čerenkov light at saturation leading to 4.7 N_{pe} for $\beta = 1$. These numbers are compatible with the range given in table 4.1. For L1, due to the strong y-coordinate dependence, only tracks in the center part of the module have been selected.

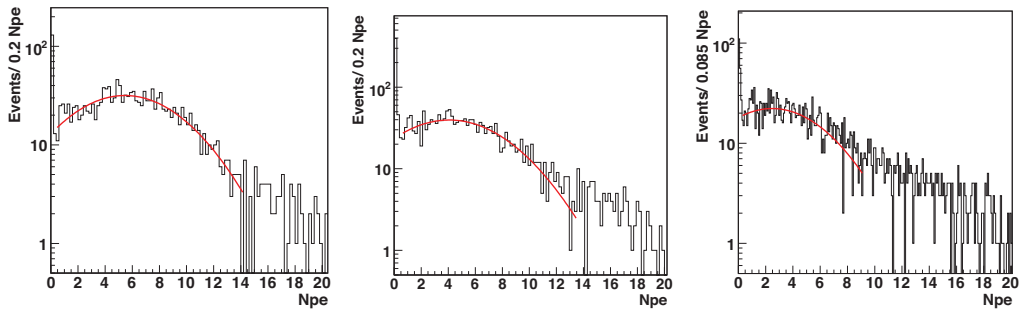

(a) (b) (c)

Figure 4.8: Integrated pulse height spectrum for kaons with a momentum between 3.75 and 4.25 GeV/c measured with H1 (a) and H2 (b). Integrated pulse height spectrum measured with L1 for kaons between 6 and 7 GeV/c (c). Pions are removed using the heavy gas detector (ChF) in anti-coincidence and antiprotons are naturally suppressed.

Momentum (GeV/c)	N_p	N_{K^+}	K^+/p measured	K^+/p expected [64]
3.75-4.25	3556	1387	0.39	0.22-0.25
6-8	4550	1998	0.44	0.12-0.14
3.75-4.25	4054	837	0.21	0.22-0.25
6-8	5630	883	0.15	0.12-0.14

Table 4.3: Expected and measured relative number of protons and positive kaons at the target without (first two lines) and with (last two lines) taking into account protons giving a signal below the Čerenkov threshold.

Usual positive polarity

The situation becomes more difficult with the usual polarity of the spectrometer magnet, i.e. with positives particles in the left arm. Depending on the momentum, 4 – 8 times more protons than kaons are expected. The measured and expected ratio between protons and kaons are summarized in table 4.3 (first two lines) by counting naively for protons only the events in pedestal. The number of events in the pedestal are less than the number of expected protons [64]. This confirms the statement that protons give some signal above pedestal. In order to match the measured and expected values, around 10% of the protons should give some signal. This is in agreement with the opposite polarity measurement. Due to the strong suppression of antiprotons, a 10% effect is not relevant and can be neglected.

Let me remind that the signal above pedestal from protons can be partially explained by δ-electrons, accidental tracks and thermal photoelectrons, especially because of the large size of the PM windows (5-inch) . Furthermore the PMs are at the limit of the recommended current[2]. In next section, one selects protons only, using different techniques (Λ-decay, time of flight). Their measured ADC spectrum consists in pedestal with a positive tail. Taking into account this tail, the expected and measured fractions are again in agreement, as shown in table 4.3 (two last lines). Therefore, one cannot consider naively the proton distribution as pedestal only, and one has to study carefully the proton spectrum to estimate its contamination in the signal region.

4.3.4 Mixed trigger

In this section, only the kaon and proton spectrum is studied. The relative number of protons, kaons and pions are no longer used. Therefore, we switch to the DIRAC-II mixed trigger used during the 2007 data taking for the search of πK-atoms. In the mixed trigger we used only $\pi^- K^+$ tagged events (section 2.4). First, the proton spectrum is studied. This proton distribution is then subtracted from the total ADC spectrum taken with the mixed trigger. Only protons and kaons are selected

[2] A baseline shift appears at a primary beam intensity of 17×10^{10} protons per spill on a Pt target. The capacitors of the voltage dividers are no longer able to discharge the accumulated charge leading to a shift of the baseline. This effect can be removed by replacing the positive voltage divider by an uncoupled negative one.

since Ch and ChF are in anti-coincidence, and therefore the remaining spectrum after subtraction contains only kaons.

Proton distribution

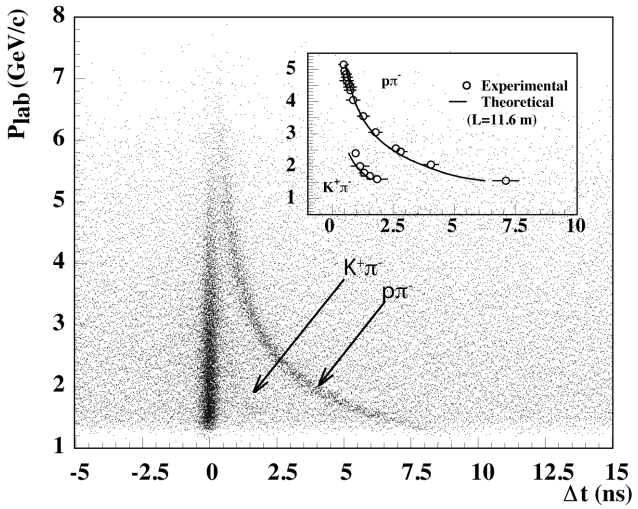

Figure 4.9: The time difference between the left and right arm of the spectrometer measured by the vertical hodoscope (VH) as a function of the momentum of the positive particle (left arm). The accumulated vertical band corresponds to $\pi^-\pi^+$-pairs and the curved band is due to $\pi^- p$-pairs. In the intermediate region $\pi^- K^+$-pairs are visible for momenta below 2.5 GeV/ c.

Extraction of proton signal using TOF techniques or Λ decays: For protons with a momentum lower than 4 GeV/c, it is possible to use TOF technics (fig. 4.9) due to the high time resolution in the vertical hodoscope. Fig. 4.9 shows the time difference between the left and right arm of the spectrometer as a function of the momentum of the positive particle (in the left arm). The vertical accumulation centered at 0 are $\pi^-\pi^+$-pairs. The curved accumulation on the right are $\pi^- p$-pairs where the protons become slower due to their mass. A few $\pi^- K^+$-pairs are visible in the intermediate region. The same results can be presented in a different way using the following relation:

$$\Delta t = \frac{L_+}{c}\sqrt{1+\left(\frac{m_+}{p_+}\right)^2} - \frac{L_-}{c}\sqrt{1+\left(\frac{m_-}{p_-}\right)^2}, \tag{4.2}$$

where $L_{+(-)}$, $p_{+(-)}$ and $m_{+(-)}$ are the particle path-lengths, momenta and masses respectively for the positive (negative) particles. Negative particles are dominated by pions. Hence, if we attribute to the negative particle the mass of a pion, one can according to equ.(4.2), plot the mass of the positive particle squared (fig. 4.10).

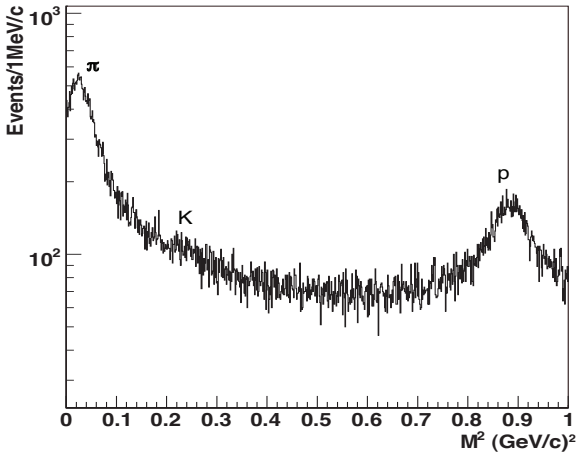

Figure 4.10: Squared mass distribution of the positive particle while the negative particle mass is set to m_π.

Another way to select protons is to use the Lambda intermediate state, which decays into a proton and a pion. Fig. 4.11 shows the invariant proton-pion mass distribution. The peak corresponds to the Lambda decay.

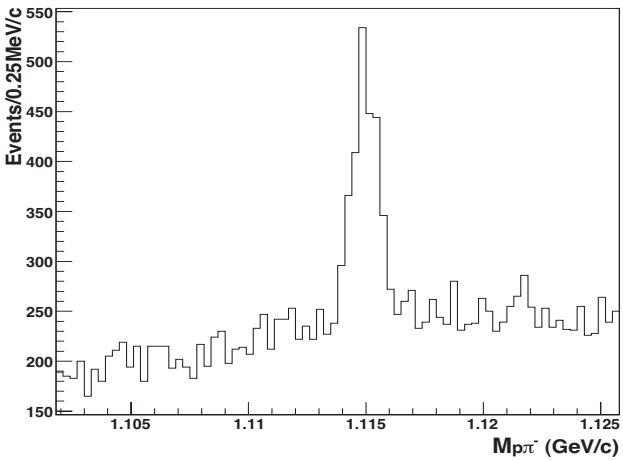

Figure 4.11: Invariant proton-pion mass spectrum. The peak is due to the Λ decay.

Using these two techniques to select protons, one obtains the resulting proton spectrum measured from left to right with H1, H2 and L1 respectively (fig. 4.12). The best fit is obtained with a Gaussian, plus a decreasing exponential for the positive tail of the distribution. This distribution provides a good way to estimate

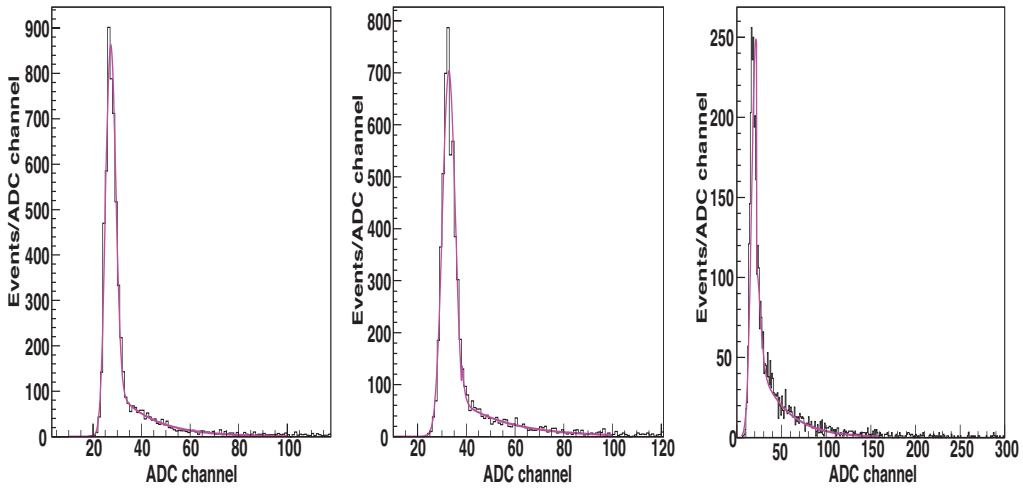

(a) (b) (c)

Figure 4.12: From left to right: Proton ADC spectrum measured with the aerogel modules H1, H2 and L1 respectively. Protons are selected using TOF technique and Λ-decays. For a parameterization, the distribution is fitted in pink with a Gaussian and an exponential.

the proton rejection efficiency. A cut one photoelectron above the mean of the pedestal leads to (94.6±8.4)%, (93.2.6±7.6)% and (89.6±9.8)% of rejected protons for H1, H2 and L1 respectively.

Kaon distribution

The proton distribution can be scaled to the ADC spectrum taken with the mixed trigger by matching the height of the two pedestals. Since the trigger selects only protons and kaons, after subtraction of the scaled proton distribution only kaons should remain. The kaon spectrum is shown in fig. 4.13 for H1, H2 and L1, respectively. Residuals from the single photon peak appear at the expected place. The fit function contains a Gaussian with the mean value fixed at the single photoelectron peak and a second Gaussian for the signal. The width of the single photon peak is too small compared to what is expected but for correctness I decided not to constrain the fit. Applying the same cut introduced above, i.e. one single photoelectron above the mean of pedestal, one gets the kaon detection efficiency of $(96.2 \pm 10.6)\%$, $(94.6 \pm 11.0)\%$ and $(89.2 \pm 12.8)\%$ respectively.

4.4 TDC analysis

During the 2007 run and only in the mixed trigger and only for $\pi^- K^+$ tagged events, the ADC gate has been shifted for all Čerenkov and preshower detectors, inducing a loss of a large fraction of the signal. Therefore, for the extraction of πK-atoms

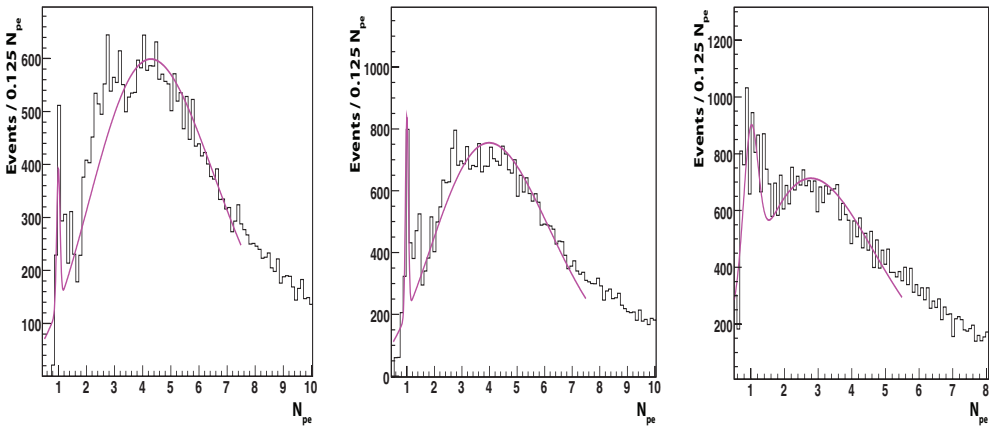

Figure 4.13: From left to right: amplitude distribution measured with H1, H2 and L1 respectively. For the heavy aerogel modules (H1 and H2), the kaons are selected with a momentum between 4 and 4.5 GeV/c and for the light module L1, kaons between 6 and 8 GeV/c. The sum of two Gaussian (one for the single photon and one for the signal) fitted to the data to estimate the kaon detection efficiency (pink).

one could use only information from the TDC. In this section, the efficiency of the TDC and distribution are discussed on the basis of exclusive $\pi\pi$ triggers.

Three TDC channels are available, one for each aerogel module. The signal of the analogue sum of the two PM signals of each module passes through a discriminator for the TDC and is measured for in an ADC. If the signal is greater than a threshold given by the discriminator, the TDC registers the event. In contrast to the ADC in which the integral of the signal is measured, the discriminator determines the threshold amplitude only. It is therefore not possible to attribute an exact ADC channel to the threshold set on the TDC. Nevertheless, one can use the proportionality between amplitude and area of the signal to estimate the corresponding ADC channel. Fig. 4.14 shows the ADC spectrum only for registered TDC hits, normalized by the total ADC spectrum. The result has been measured with H1, H2 and L1, respectively without any requirement on the trigger. In the plateau all ADC events have a corresponding TDC hit. The best estimate of the ADC channel corresponding to the cut in the discriminator is given by the dotted line.

With the corresponding ADC channel, one can obtain the proton rejection efficiency and the kaon detection efficiency using the ADC proton and kaon parameterization from the previous section. I adjusted the threshold on the discriminators of the TDC so that the corresponding ADC channel leads, according to fig. 4.12, to a rejection of 95% of protons with H1, H2 and 90% with L1. The fractions of rejected protons have been crosschecked by counting the number of events in the Λ peak with and without a TDC hit. Deviations are smaller than 3%.

For a fine-tuning of the threshold, it is possible to increase the proton rejection efficiency. Pulses with a large amplitude rise faster than small pulses and thus reach

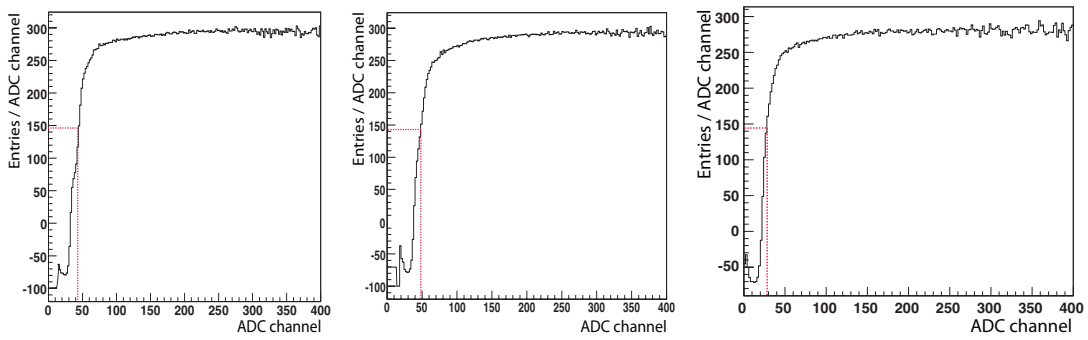

(a) (b) (c)

Figure 4.14: From left to right: ADC spectrum for registered TDC hits normalized by the total ADC spectrum for H1, H2 and L1. Red lines correspond to the discriminator setting.

faster the threshold of the discriminator of the TDC. Hence cutting at the right end of the peak of the TDC removes the small ADC signals from the data sample and leads to a better proton rejection efficiency. In the further analysis events between channel 256 and 318 are accepted in H1 and H2. For L1, events between 234 and 291 are accepted.

4.5 Digitization of the detector response

Ariane the reconstruction software for real tracks as well as for MC has been introduced in section 2.5. In the latter case, the digitization of the detectors is also done in Ariane separately from GEANT-DIRAC. The responses of the aerogel detector are implemented in the software based on lookup tables, which have been obtained from real data. For each event, depending on the particle type, momenta and vertical impact position a random number is generated according to the corresponding measured ADC spectrum.

For protons and kaons, I divided the momentum range in 0.5 GeV/c bins between 4 and 6 GeV/c and in two bins of 1 GeV/c between 6 and 8 GeV/c due to less statistics. The corresponding ADC spectrum is measured and parametrized. The dependence on the vertical position is then introduced according to fig. 4.5. Electrons and pions have $\beta = 1$ between 4 and 8 GeV/c. Therefore the momentum range has not to be divided in subranges.

For the digitization of the time distribution for the three aerogel modules, a fit is applied to the TDC spectrum (fig. 4.15). One channel corresponds to 500 ps. Four different regions can be observed:

- The time correlated events are around channel 300 where a Gaussian fit has been applied. This is the region of interest.
- Around channel 200 and 300 are time correlated events with small signals.

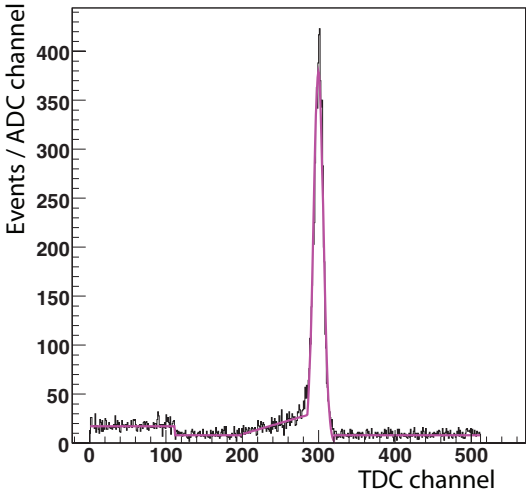

Figure 4.15: TDC spectrum measured with H1. For H2 and L1 the distribution is similar.

Small TDC-channels correspond to slow discriminator response (small signal amplitudes). In this region also time correlated events are shifted due to jittering. The first part of this region is dominated by accidentals but the second part contains mainly good events and should not be cut out.

- A background region is located between channel 120 and 200 and between 320 and 500. These events are time uncorrelated (accidentals).
- Another background region is located between channel 0 and 120 where the time uncorrelated events are counted twice. This is due to reflections in cables or some other trigger related effects, but they are however cut out.

For each hit in the ADC above the channel corresponding to the threshold of the discriminator, a TDC hit is simulated according to the fitted distribution (fig. 4.15).

Chapter 5

Data analysis: Search for $\pi\pi$-atoms

The aim of this study is to extract $\pi\pi$-atoms using only the detectors downstream of the magnet (fig. 2.2). Indeed, during the 2007 run only downstream detectors were in use. It is hence crucial to compare the $\pi\pi$ data from the so called *upstream* tracking including information from the whole setup, with the so called *downstream* tracking, which uses only the DC and is therefore independent of the upstream detectors (IH, SFD, MDC). Furthermore, one hopes to increase the $\pi\pi$ data sample and hence reduce the statistical errors on the published $\pi\pi$-scattering lengths [1].

This $\pi\pi$-analysis has been performed with the 2001 data sample for which the upstream tracking, as well as the corresponding Monte-Carlo data, were available. In the last section, the method is applied to the 2007 data sample searching for $\pi\pi$-atoms in a first step to give confidence to the πK search.

5.1 Downstream tracking

5.1.1 Procedure

The pattern recognition starts with the horizontal x-coordinates at the last plane of the DC and proceeds back to the target. First, a straight line is fitted through the hits in the drift chambers and is extrapolated into the magnet where a deflection algorithm (shown schematically in fig. 5.1(a)) changes the slopes and coordinates of the track according to the magnetic field. Then, another straight line is fitted back to the target, with the constraint that the track crosses the beam spot, i.e. $x = 0$. However, this method cannot take into account multiple scattering in the upstream detectors and in the aluminum-window of the vacuum chambers close to the magnet (fig. 2.2). The constraint $x = 0$ remains essential for the determination of the momentum P. Once the momentum is determined, the procedure is repeated with the vertical y-coordinate; the deflection algorithm for the magnetic field is applied to the y-coordinate and the track extrapolated back to the target. This is

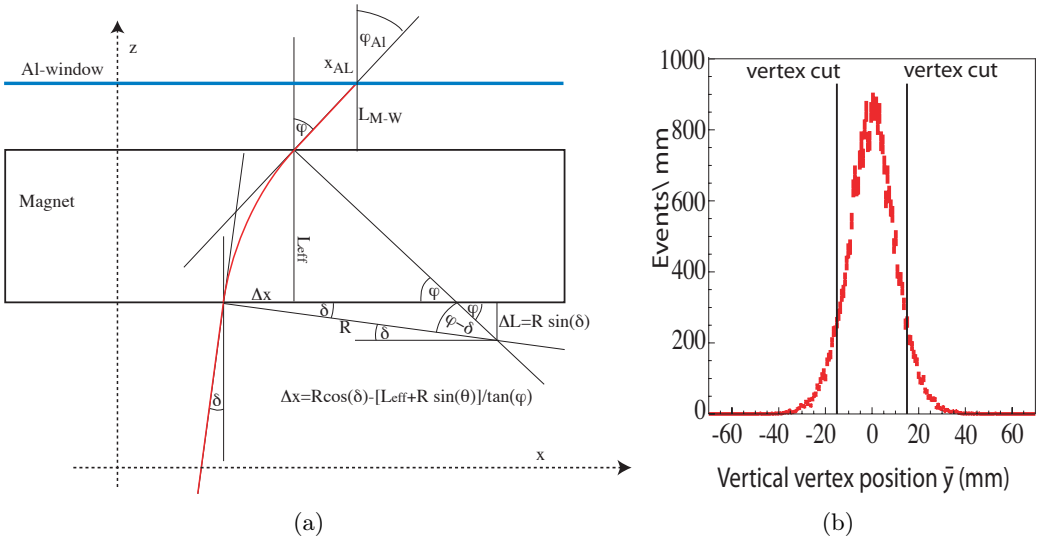

(a) (b)

Figure 5.1: (a): Principle of the horizontal deflection algorithm. (b) Distribution of the average $\overline{y}$ of the two y-coordinates at the target for downstream extrapolation method. No cut has been applied so far to the vertex position $\overline{y}$.

the so-called *extrapolation* method. In contrast to the x-coordinate, the constraint $y = 0$ is not needed since the momentum is already known. This method provides for the two tracks (one from the left arm and one from the right one) of an event two different y-coordinates for the vertex position at the target y_{T1}, y_{T2}. A vertex cut has been applied requiring that the average of the y-coordinates $\overline{y} = (y_{T1} + y_{T2})/2$ lies at most 1.5 cm from the beam spot. The $\overline{y}$-distribution is shown in fig. 5.1(b).

The number of reconstructed events by the downstream tracking can be improved by releasing the cut on $\overline{y}$. Events with large $\overline{y}$ are in fact good events which have been scattered in the upstream detectors and are hence rejected while they are kept in the full tracking. In this study, we try to recover these events by introducing a new tracking method, the so-called *interpolation* method. For the x-coordinate, the two methods are exactly the same, while for the y-coordinate the fringe fields of the spectrometer magnet are neglected and the deflection algorithm is hence ignored. One can therefore fit a straight line back from the Al-window through the magnet to the target with the constraint $y_T = 0$.

In fig. 5.2 a scheme for the vertical track propagation is shown comparing the two different reconstructions. Both methods for the downstream tracking ignore multiple scattering in the IH, the SFD and the MDCs. The extrapolation method also ignores multiple scattering in the Al-window since a straight line is fitted from the drift chambers back to the magnet. On the contrary, the interpolation method ignores the magnetic deflection, since a straight line is fitted from the Al-window to the target. However, no cuts have been applied with this new interpolation method, leading to higher statistics. For more details we refer to [67].

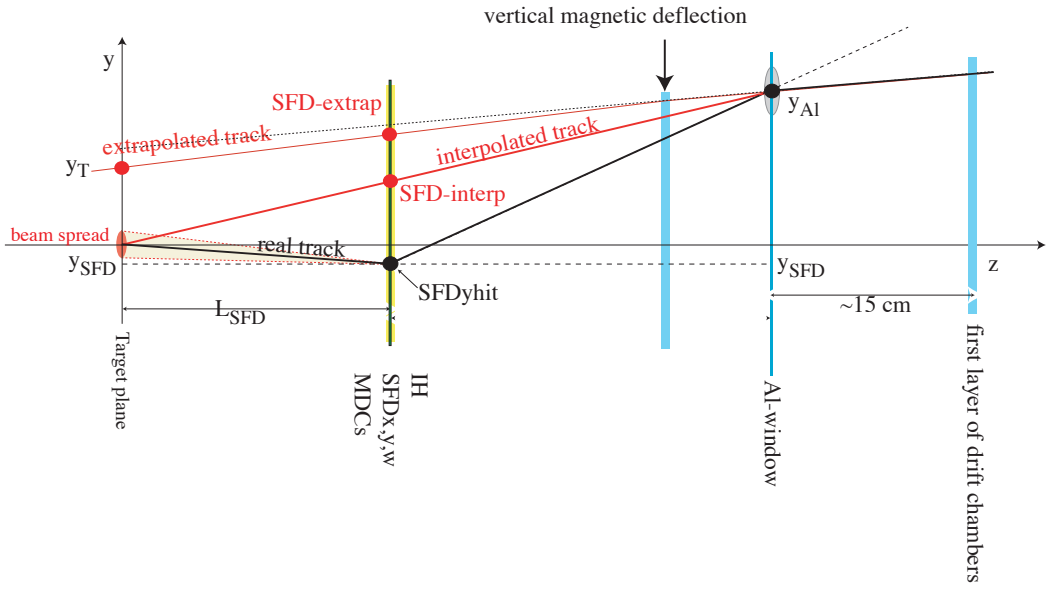

Figure 5.2: Principle of the vertical track propagation according to different track reconstruction algorithms. The downstream tracking ignores multiple scattering in the IH, the SFD and the MDCs. The extrapolation method also ignores multiple scattering in the Al-window, since a straight line is fitted from the drift chambers up to the magnet. The interpolation method ignores the magnetic deflection since a straight line is fitted from the Al-window to the target.

5.1.2 Quality of the downstream tracking

In this section, the quality of the downstream tracking with the interpolation method is analyzed. As a first step, I use the well-known and precise upstream tracking to compare the variable of interest for the further $\pi\pi$-analysis, i.e. Q, the relative momentum in the center of mass of the two particles defined as:

$$Q_x = P_x^+ + P_x^-, \tag{5.1}$$

$$Q_y = P_y^+ + P_y^-, \tag{5.2}$$

$$Q_L = 2 \cdot \frac{P_z^+ E^- - P_z^- E^+}{\sqrt{(E^+ + E^-)^2 - (P_z^+ + P_z^-)^2}}, \tag{5.3}$$

where $\vec{P}^+ = (P_x^+, P_y^+, P_z^+)$ and $\vec{P}^-$ are the momenta in the laboratory system for the positive, negative arm respectively. The three components are reconstructed with the information of the DC only for the downstream tracking $\vec{Q}_{DC} \equiv (Q_{x,DC}, Q_{y,DC}, Q_{L,DC})$ and with in additional the IH, SFD and MDCs for the upstream tracking ($\vec{Q}_{upstream}$). We reiterate that Q_L is the longitudinal component along the beam axis, while Q_x, Q_y are in the transverse plane. The difference of the two reconstructed relative momenta are plotted in fig. 5.3: MC in red and real data in blue. The MC and the data are in good agreement. As one could expect, the downstream

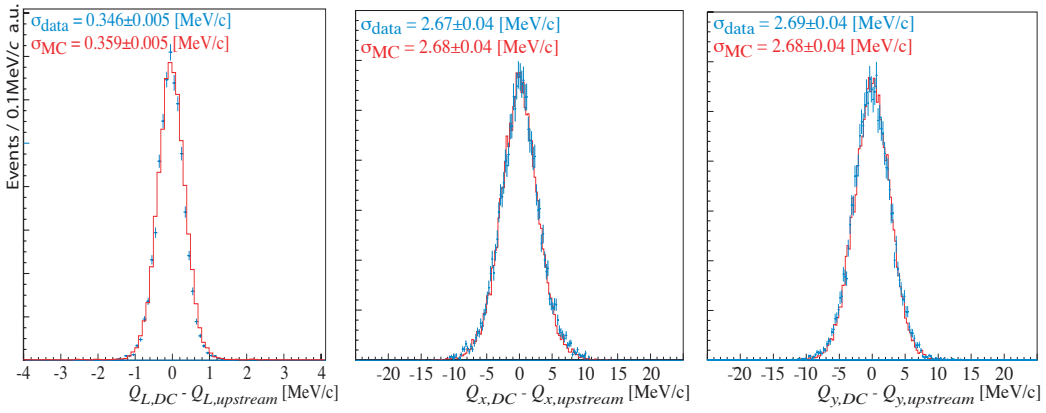

(a) Q_L (b) Q_x (c) Q_y

Figure 5.3: Difference of the Q-components for the upstream and downstream only reconstruction of the Ni-2001 data (blue points with error bars). The simulated Coulomb-pairs, which dominate the 2001 data sample, are shown by the red histograms.

tracking is strongly affected in the transverse plane (Q_x, Q_y). This is related to multiple scattering and leads to a difference in the transverse relative momentum between 2.5 and 3 MeV/c.

Since the MC reproduces the reconstructed Q distribution precisely, one can use it to get information on the absolute reconstruction resolution independently of the upstream tracking. The event by event difference between the generated relative momentum at the exit of the target $Q_{target-exit}$ and the reconstructed one Q_{DC} is plotted in fig. 5.4 for different types of events: atoms in red and Coulomb-pairs in blue. The momentum resolution is 0.35 MeV/c in Q_L and below 2.7 MeV/c in Q_x, Q_y. Therefore a binning of 1 MeV/c for the transverse components and a binning of 0.25 MeV/c for the longitudinal component of the relative momentum Q is appropriated.

For a direct comparison between MC and data one needs to extract one type of events unambiguously from the data. This can be done only for the time uncorrelated flat background, the accidentals. MC accidentals have hence been generated with a cut on the longitudinal and transverse relative momentum $Q_L^{generated} < 30$ MeV/c and $Q_{x,y}^{generated} < 30$ MeV/c respectively. Accidental data have been extracted from the Ni-2001 data sample. A cut at $Q_{x,y} < 8$ MeV/c and $Q_L < 20$ MeV/c has been applied on both data and reconstructed MC.

In fig. 5.5 the ratio data over Monte Carlo is given in green for the extrapolation method and in red for the interpolation method for Q_x, Q_y and $|Q_L|$. While for Q_x and Q_L the interpolation and extrapolation methods are well described by the Monte Carlo, for Q_y the ratio is not flat any more for the extrapolation method above $|Q_y| = 4 - 5$ MeV/c. The interpolation method removes this inefficiency. From now on, I therefore only use the interpolation method.

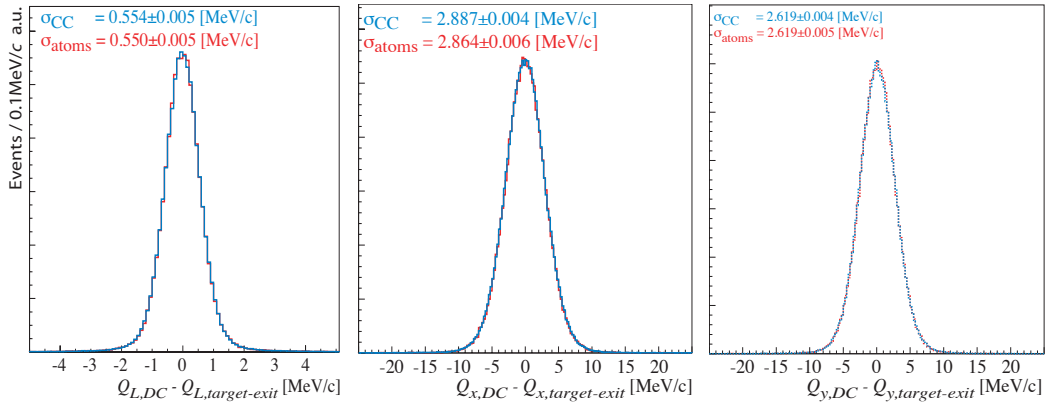

(a) Q_L (b) Q_x (c) Q_y

Figure 5.4: Simulated MC event by event difference between the generated and downstream reconstructed Q-components. The red points show the atoms and the blue histograms the Coulomb-pairs.

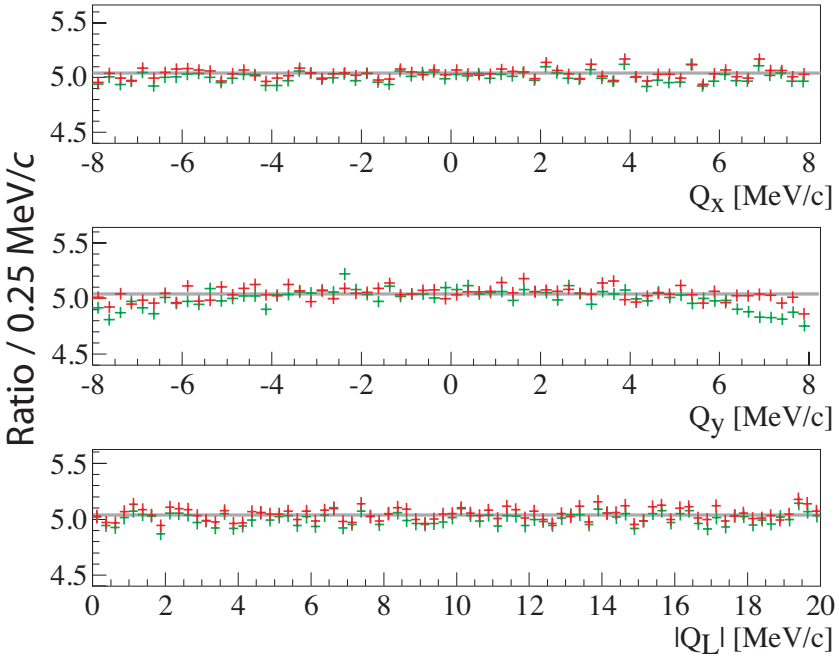

Figure 5.5: Ratio of data over MC events for the Ni-2001 data sample. Accidentals reconstructed with the interpolation method are shown in red, those using the extrapolation method in green.

5.2 Signal extraction

5.2.1 Overview

In this section, I describe how to extract the number of atomic and Coulomb-pairs, the quantities needed for the measurement of the breakup probability, and hence the mean life of these atoms. The relative momentum of ionized atomic-pairs is very small (fig. 1.2), i.e. $Q_L < 2$ MeV$/c$ [1]. DIRAC aims the detection of an excess in the lower part of the relative momentum distribution. Unfortunately, while the atomic-pairs travel through the target, the transverse component of the relative momentum is distorted due to multiple scattering, while the longitudinal component remains almost constant. The aim is therefore to look for an excess in the lower part of the time correlated Q_L spectrum, i.e. for $Q_L < 2$ MeV$/c$.

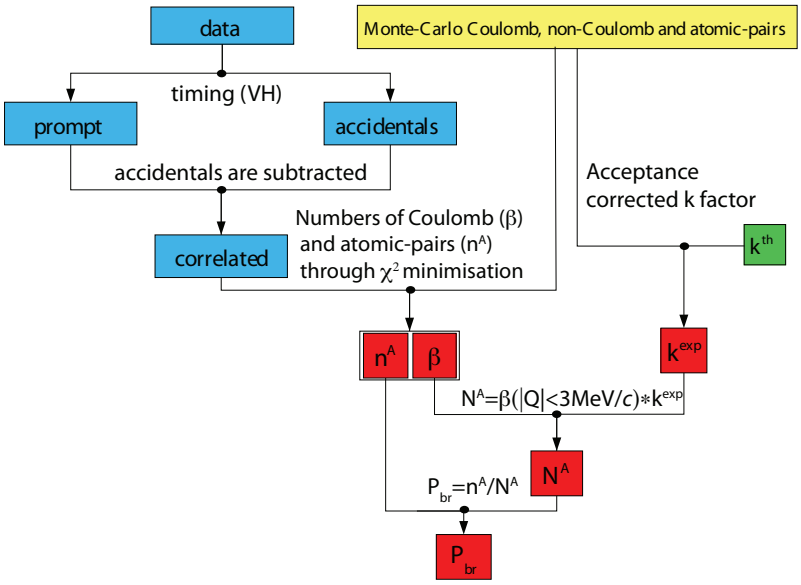

Figure 5.6: Flow diagram illustrating the different steps of the further analysis. Blue boxes use information from data, yellow ones from MC and green ones from theory. For the red boxes, information from different contributions are needed.

A rough overview of the analysis is given in a flow diagram (fig. 5.6). From the data sample prompt (time correlated) and accidentals (time uncorrelated) events are extracted using a timing measurement of the vertical hodoscope (VH). From prompt events, the accidental part is subtracted to get only time correlated events. The numbers of non-Coulomb and Coulomb-pairs (β) are obtained by a fit to the prompt events outside the signal region. The number of atomic-pairs (n^A) is derived from the residuals between the prompt events and this fit extrapolated into the signal region. An improvement can be achieved by including the atomic-pair distribution

in the fit. The theoretical k-factor (k^{th}) which correlates the number of Coulomb-pairs with $|Q| < 2$ MeV/c to the number of produced atoms (N^A) is corrected using MC to take into account the acceptance function of the DIRAC-II experiment. The breakup probability $P_{br} = n^A/N^A$ can then be calculated. Details are given in the following sections.

5.2.2 Event selection

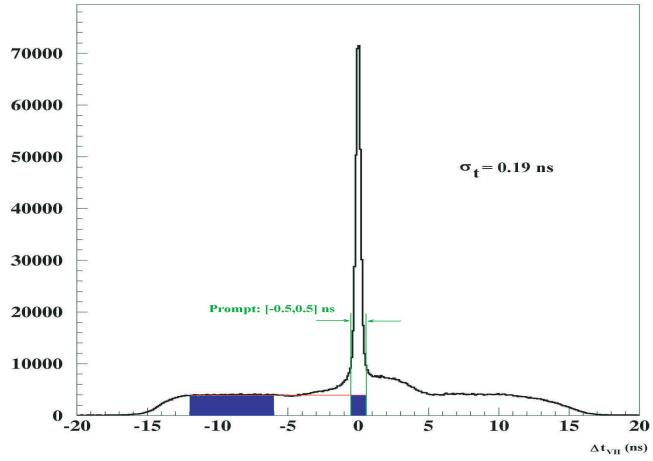

Figure 5.7: Distribution of the time difference Δt between two particles, one in each spectrometer arm, measured by the vertical hodoscopes. Time correlated or *prompt* events are selected between -0.5 and 0.5 ns. Accidentals are taken between -12 and -6 ns.

The time difference between positive and negative particles measured by the vertical hodoscopes is shown in fig. 5.7. This distribution is used to select two different types of events. The first type are the *prompt* events defined as pairs, with a maximum time difference of 0.5 ns. The second type are *accidentals*, which are time uncorrelated pairs measured within -6 and -12 ns, as shown in fig. 5.7. I chose a negative time difference because on the positive side the signal is contaminated by slow protons. These accidentals in fig. 5.7 are used later to estimate the percentage of accidentals in the prompt region.

The prompt events N^{prompt} and accidentals N^{acc} are then further reduced according to the following criteria:

- no electrons nor positrons (anti-coincidence with Ch)
- no muons (anti-coincidence with Mu)
- one and only one DC track per arm
- P^+, the momentum in the lab system for positive particles has to be smaller than 4 GeV/c to remove protons

- $|Q_L| < 20$ MeV/c
- $Q_T < 8$ MeV/c.

5.2.3 Fit function and background description

The prompt spectrum is composed of different event types: atomic-pairs (A) and time correlated Coulomb (C) and non-Coulomb-pairs (nC), plus the time uncorrelated accidentals (acc). One can write

$$\frac{dN^{prompt}}{dQ_L} = \alpha \cdot \frac{dn^A}{dQ_L} + \beta \cdot \frac{dN^C}{dQ_L} + \gamma \cdot \frac{dN^{nC}}{dQ_L} + \delta \cdot \frac{dN^{acc}}{dQ_L}, \tag{5.4}$$

where $\frac{dN^i}{dQ_L}$ are the predicted numbers (MC) of a given event type i ($i = A,\ C,\ nC$ or acc) per interval dQ_L. The free parameters α, β, γ and δ give the corresponding number of an event type if $\frac{dN^i}{dQ_L}$ are normalized to one in the region of interest. In fact one can interpret them as the probability to see an event type in an interval dQ_L. $\frac{dN^{prompt}}{dQ_L}$ is the number of measured prompt events in dQ_L and is not normalized.

Let us first deal with the accidentals. As already mentioned, δ is the number of accidentals present in the prompt spectrum. One can fix this number by measuring the accidental contribution outside the prompt region between -12 to -6 ns. By extrapolating the number of detected accidental-pairs with a straight line to the prompt region as shown in red in fig. 5.7, it is possible to extract the fraction of accidentals in the prompt region and one gets $\delta = N^{prompt} \cdot (11.74 \pm 0.21)\%$.

Once the accidentals (blue area in prompt range) are subtracted only time correlated events remain. One can define the number of time correlated events inside N_{IN}^{corr} and outside N_{OUT}^{corr} the signal region where no atomic-pairs are expected, i.e. for $|Q_L| > 2$ MeV/c [1]:

$$\begin{aligned} N_{IN}^{corr} &= \alpha + \beta + \gamma, \\ N_{OUT}^{corr} &= \beta + \gamma. \end{aligned} \tag{5.5}$$

Together with equ.(5.7) one can rewrite equ.(5.5) as:

$$\frac{dN_{IN}^{corr}}{dQ_L} = \alpha \cdot \frac{dn^A}{dQ_L} + \beta \cdot \frac{dN^C}{dQ_L} + (N_{IN}^{corr} - \alpha - \beta) \cdot \frac{dN^{nC}}{dQ_L}, \tag{5.6}$$

$$\frac{dN_{OUT}^{corr}}{dQ_L} = \beta \cdot \frac{dN^C}{dQ_L} + (N_{OUT}^{corr} - \beta) \cdot \frac{dN^{nC}}{dQ_L}. \tag{5.7}$$

The first fitting procedure uses the region $|Q_L| > 2$ MeV/c to measure the number of the Coulomb and non-Coulomb-pairs and hence equ.(5.7) is used. The number of Coulomb and non-Coulomb-pairs can then be extrapolated in the signal region according to their distribution. First, one needs to normalize the probability function in the fitting region, i.e. for $|Q_L|$ between 2 and 20 MeV/c. Introducing a bin size of 0.25 MeV/c for each bin $dQ_{L,i}$ ($i = 1, .., 80$) one can write:

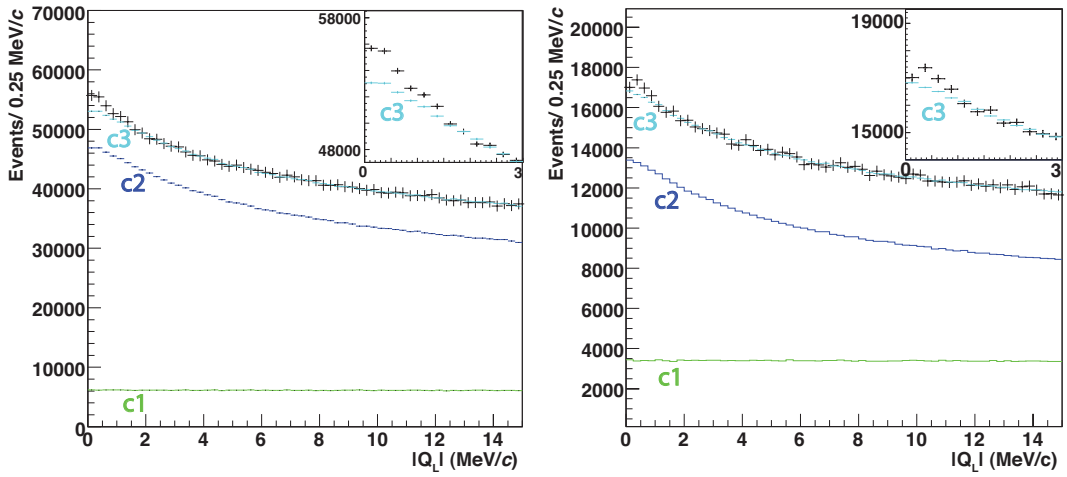

(a) (b)

Figure 5.8: Q_L **distribution for data (points with error bars in black) and fitted background for simulated non-Coulomb-pairs in green (c1) and simulated Coulomb-pairs in blue (c2). The total simulated background is plotted in turquoise (c3). The excess of data for low** Q_L **is the signal. In (a) the results for the Ni-2001 94** μ**m target are plotted and in (b) for the Ni-2001 98** μ**m target. The insets are close-up views of the signal regions.**

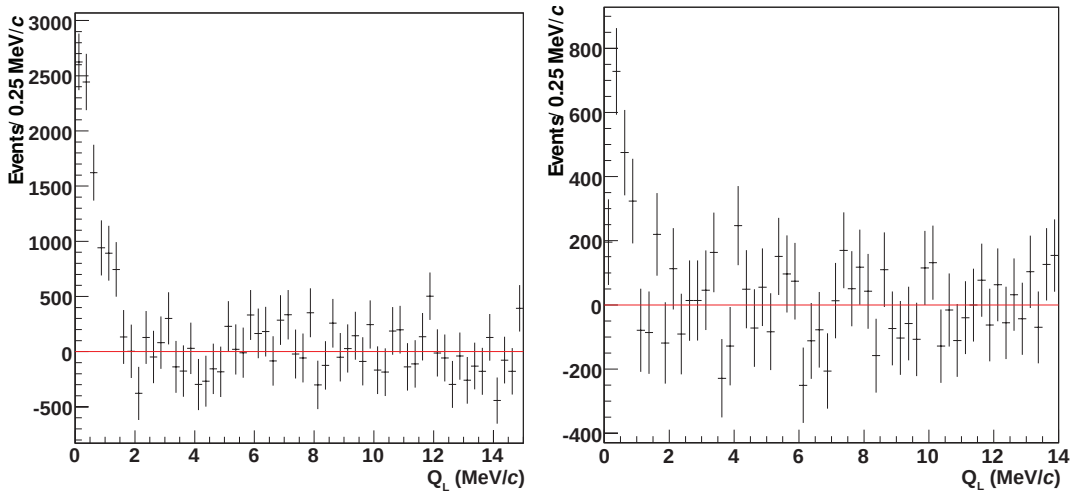

(a) (b)

Figure 5.9: Residuals between data and fitted background contributions from MC in Q_L **for the Ni-2001 94** μ**m target (a) and for the Ni-2001 98** μ**m target (b).**

$$\sum_{i=9}^{80}\left(\frac{dN^C}{dQ_{L,i}}\right)=\sum_{i=9}^{80}\left(\frac{dN^{nC}}{dQ_{L,i}}\right)=1, \tag{5.8}$$

The χ^2-function to be minimized is then the difference between the data and the MC background predictions in the Q_L distribution between 2 MeV/c and 20 MeV/c:

$$\chi^2\equiv\sum_{i=9}^{80}\left(\frac{\frac{dN^{corr}}{dQ_{L,i}}-\beta\cdot\frac{dN^C}{dQ_{L,i}}-(N^{corr}-\beta)\cdot\frac{dN^{nC}}{dQ_{L,i}}}{\sigma_i^{prompt}}\right)^2, \tag{5.9}$$

where σ_i^{prompt} is the error[1] on bin i of the measured prompt $|Q_L|$ distribution.

The χ^2-minimization based on Minuit [69] determines the free parameter β which is the number of Coulomb-pairs between 2 and 20 MeV/c. The fit is shown in fig. 5.8 together with the data in black. In green are the non-Coulomb, and in blue the Coulomb-pairs. In turquoise is the sum of both contributions. The excess of data at low Q_L is the signal. The residuals are plotted in fig. 5.9 and summarized in table 5.1 (first and last line). The error on β are MINOS errors, while the error on the atoms comes from the square root of the data.

Instead of using the simulated non-Coulomb Q_L distribution in the χ^2 defined in equ.(5.10), one can also use the accidental Q_L distribution extracted from the data, since their distribution are locally identical. This allows to be less MC dependent, the only simulated pairs are the Coulomb correlated ones. Fig. 5.10 shows the two distributions: the non-Coulombs in red and the accidentals in blue.

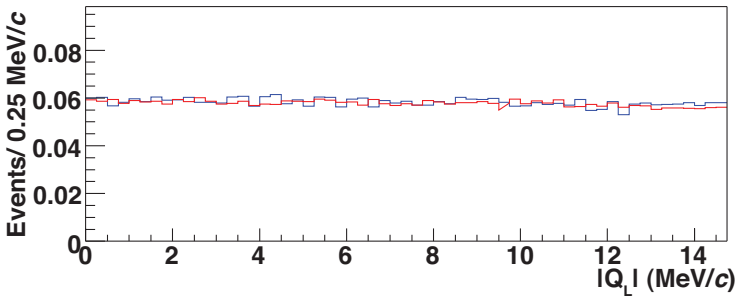

Figure 5.10: $|Q_L|$ distribution for accidentals extracted from the data in red and simulated non-Coulomb pairs in blue.

Another technique is to include the predicted atomic shape in the fit, the so-called *fit with atomic shape*. In this case, the signal region will also be used for the fit, i.e. for $|Q_L|$ between 0 and 20 MeV/c and the number of atoms α is the second

[1] The error is the statistical fluctuation and hence the square root of the bin content: we neglect the fluctuations of the MC, since 10 times more events than in the collected data have been produced .

target	fit technique	fit variable	$\chi^2/ndof$	β	n^A, α
Ni-94 μm	without atomic shape	Q_L	54.6/50	$361'855 \pm 3'343$	$9'404 \pm 705$
Ni-94 μm	with atomic shape	Q_L	64.0/58	$362'582 \pm 2'865$	$9'214 \pm 654$
Ni-94 μm	with atomic shape	Q_L, Q_T	613/478	$303'026 \pm 2'215$	$7'654 \pm 441$
Ni-98 μm	without atomic shape	Q_L	59.3/50	$98'468 \pm 1'570$	$2'636 \pm 370$

Table 5.1: Fit parameters and number of extracted atoms for the 2007 data sample for different fits. The errors on β and α (for the fit with atomic shape) are calculated with MINOS, while the errors on n^A (for the fit without atomic shape) are the square root of the data.

free parameter of the χ^2. This technique has the advantage that the errors on the atoms are reduced, since the distribution is fixed form the MC. The χ^2 based on equ.(5.6) for the new fit is:

$$\chi^2 \equiv \sum_{i=1}^{80} \left(\frac{\frac{dN^{corr}}{dQ_{L,i}} - \alpha \cdot \frac{dN^{at}}{dQ_{L,i}} - \beta \cdot \frac{dN^{C}}{dQ_{L,i}} - (N^{corr} - \beta - \alpha) \cdot \frac{dN^{nC}}{dQ_{L,i}}}{\sigma_i^{prompt}} \right)^2 . \quad (5.10)$$

The result of the fit is shown in fig. 5.11, where again the data are in black, the non-Coulomb in green and the Coulomb-pairs in blue. In contrast to the previous fit one can directly see the $\pi\pi$-atom distribution in red. In turquoise is the sum of all three contributions, which fits the data perfectly. Results are summarized in table 5.1 (second line). They are in good agreement with the fit without atomic shape.

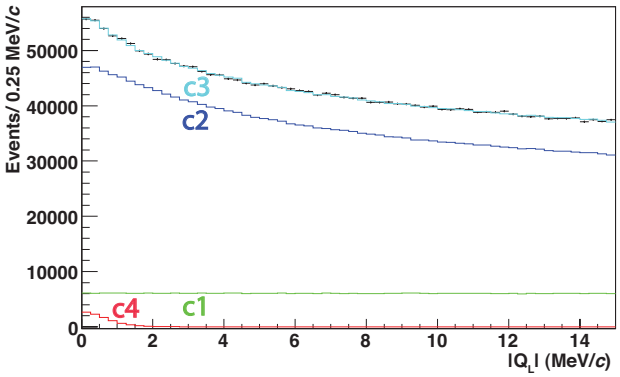

Figure 5.11: $|Q_L|$ distribution for data (points with error bars in black), fitted background for simulated non-Coulomb-pairs in green (c1) and simulated Coulomb-pairs in blue (c2). In addition to the fit without the atomic shape, the simulated $\pi\pi$-atom distribution is plotted in red (c4). The total MC contributions is plotted in turquoise (c3).

To minimize the errors on the fit parameters, one would like to fit simultaneously in Q_L and Q_T. One has to ensure that the MC correctly describes the background in

the transverse plane. Once the MC Coulomb and non-Coulomb contributions have been subtracted from the prompt data, the residuals should contain the atomic-pairs for $|Q_L| < 2$ MeV/c and they should be flat centered at zero outside of the signal region, i.e. for $|Q_L| > 2$ MeV/c. Fig. 5.12(a) shows the Q_T distribution for $Q_L > 2$ MeV/c. The non-flat shape shows that our understanding of the background in terms of transverse momentum is not sufficient at this point.

Two corrections have then been applied to the MC:

- The bar holding the PMs of the Ch detector absorbs particles. Since the trigger requires a hit in the preshower detector located just behind the Ch, these events are not registered which leads to a dip in the data. This effect has been corrected by re-weighting the MC events passing through the Ch bar to simulate the effect of the dip.
- The simulated width of the Λ decay is too small compared to the one from data, as shown in fig. 5.13. This can be corrected by a 1 ‰Gaussian smearing. The source of this smearing is still under investigation, but recent results suggest a assumption for the pressure in the vacuum chambers.

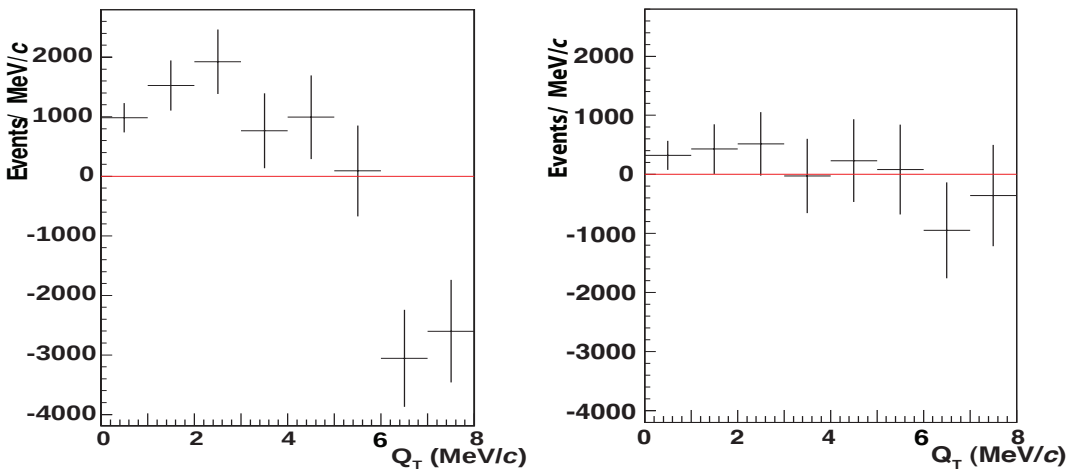

(a) (b)

Figure 5.12: Distribution of Q_T-residuals between data and fitted background contribution from MC for Q_T without corrections (a), and with corrections (b) (Ni-2001 94 μm target). Only events with $|Q_L| > 2$ MeV/c are selected where no atoms are expected.

After corrections, the Coulomb and non-Coulomb MC contributions have been again subtracted from the data in the region where no atoms are expected, to obtain the Q_T distribution shown in fig. 5.12(b). The distribution is now flat within errors and the bin content is centered around zero. The MC describes the transverse component of the relative momentum sufficiently well to be included in the fit

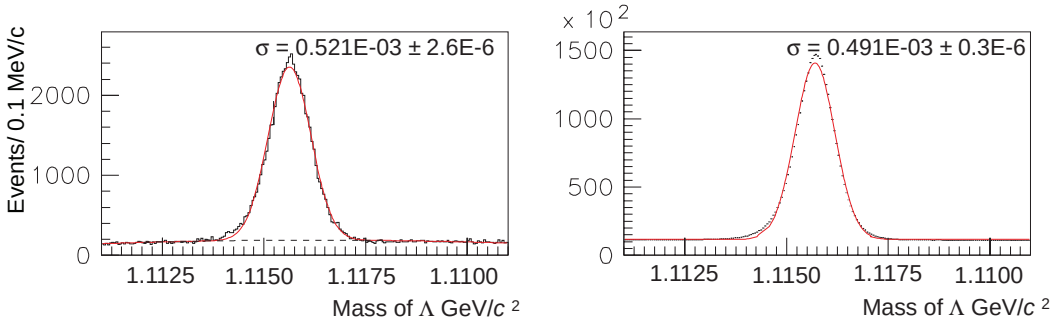

Figure 5.13: $\pi^- p$ invariant mass distribution for the momentum range between 5 and 8.6 GeV/c. The peak corresponds to the Λ-resonance. The measured distribution is on the left and the simulated one on the right [70].

function. Keeping a binning in Q_L of 0.25 MeV/c and a binning in Q_T of 1 MeV/c, the two-dimensional χ^2 is then:

$$\chi^2 \equiv \sum_{i=1}^{80}\sum_{j=1}^{8}\left(\frac{\frac{dN^{corr}}{dQ_{L,i}dQ_{T,j}} - \alpha\cdot\frac{dn^{A}}{dQ_{L,i}dQ_{T,j}} - \beta\cdot\frac{dN^{C}}{dQ_{L,i}dQ_{T,j}} - (N^{corr}-\beta-\alpha)\cdot\frac{dN^{nC}}{dQ_{L,i}dQ_{T,j}}}{\sigma_{i,j}^{prompt}}\right)^2, \tag{5.11}$$

where i defines the bin in Q_L and j in Q_T. The fit region is for $|Q_L| < 20$ MeV/c and $Q_T < 8$ MeV/c.

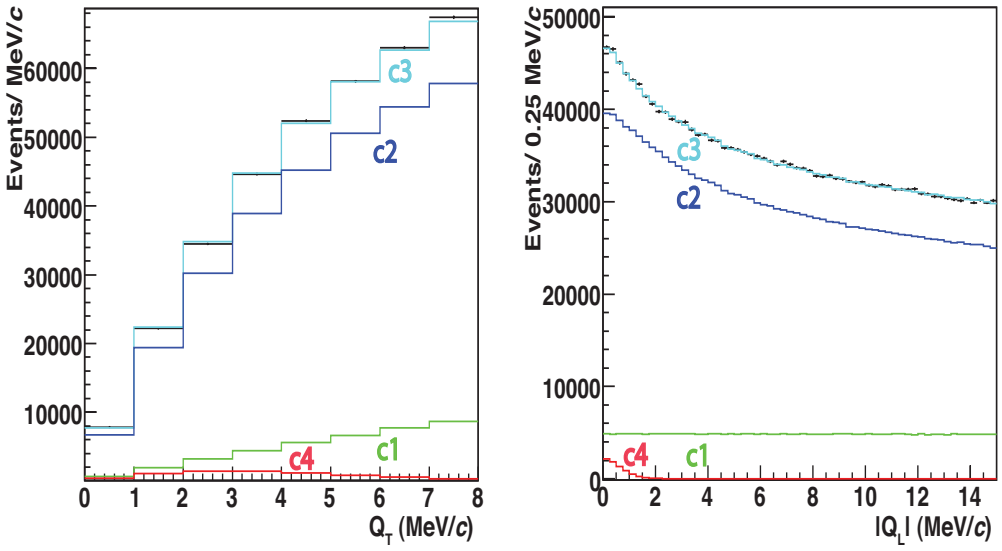

Figure 5.14: Q_T (left) and $|Q_L|$ (right) distributions for data (black points with error bars) and the fitted background in green for simulated non-Coulomb (c1), in blue for simulated Coulomb-pairs (c2), in red for simulated atomic-pairs (c4) and in turquoise the sum of all MC distributions (c3) (Ni-2001 94 μm target data sample).

The Q_T and Q_L fit results are shown in fig. 5.14 together with the data for the Ni-2001 94 μm target data sample. The residuals between data and MC in Q_T and Q_L are shown in fig. 5.15 together with the fitted MC distribution. Results of the fit are summarized in table 5.1 (third line). The number of Coulomb-pairs β and atomic-pairs α are slightly lower than for the fit along Q_L only. The errors become smaller by including also the transverse plane.

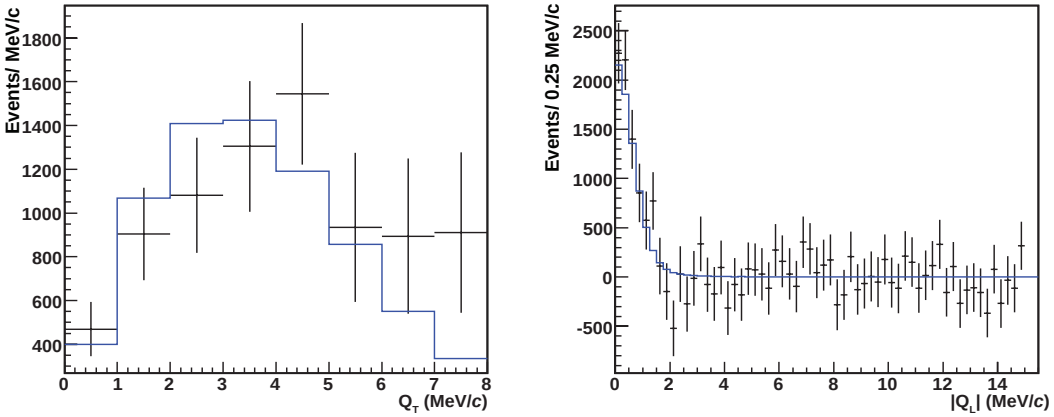

Figure 5.15: Residuals between the data (points with error bars in black) and the MC background distributions for Q_T (left) and $|Q_L|$ (right). The $\pi\pi$-atoms distribution from MC is fitted (blue line) for the Ni-2001 94 μm target data sample. Q_T corrections are applied.

5.3 Measurement of the mean life of $\pi\pi$-atoms

The mean life measurement is performed in three steps: the measurement of the experimental k-factor (k^{exp}), the breakup probability P_{br}, and the mean life of $\pi\pi$-atoms in the 1S state, τ_{1S} defined in equ.(1.8).

In section 1.2 equ.(1.14) we introduced the theoretical k-factor ($k^{th} = 0.615$) relating the number of Coulomb-pairs for $\Omega = \{Q < 4 \cdot p_B\}$ to the number of produced atoms. For $\pi\pi$-atoms rounding down to the closest bin, one gets $4 \cdot p_B = 2$ MeV/c. We remind that p_B is the Bohr momentum.

However, the experiment measures the number of reconstructed Coulomb and atomic-pairs below a given cut Q_L^{cut}, Q_T^{cut}, $n^A(Q_L^{cut},\ Q_T^{cut})$ and $N^C(Q_L^{cut},\ Q_T^{cut})$ respectively. In this analysis I chose for the signal region, where the break up probability has to be measured, the following cuts: $|Q_L|^{cut} = 2$ MeV/c and $Q_T^{rec} = 8$ MeV/c. In contrast to k^{th}, the introduced k^{exp} takes into account the acceptance of the setup and the overall inefficiency of the experiment. Using the breakup probability introduced in equ.(1.16) one can define k^{exp} as

$$P_{br} = \frac{n_i^A}{k^{th} \cdot N^C(Q^{initial} < 4 \cdot p_B)} \equiv \frac{n^A(Q_L^{cut},\ Q_T^{cut})}{k^{exp} \cdot N^C(Q_L^{cut},\ Q_T^{cut})}, \tag{5.12}$$

where n_i^A are the number of generated atoms. This equation can be rewritten as

$$k^{exp} \equiv k^{th} \cdot \frac{N^C(Q^{initial} < 4 \cdot p_B)}{n_i^A} \cdot \frac{n^A(Q_L^{cut},\ Q_T^{cut})}{N^C(Q_L^{cut},\ Q_T^{cut})}. \tag{5.13}$$

The k^{exp}-factor has been calculated using $2 \cdot 10^8$ MC events for the Coulomb-pairs and $7.4 \cdot 10^5$ MC events for the atomic-pairs. The results are summarized in table 5.2, giving the experimental k-factor $k^{exp} = 0.0667$. The error is negligible due to the large statistical sample.

	n^A	N^C	$k^{exp} \times 10^5$
Total generated	740'000	199'492'851	
Generated with $Q^{init} < 2MeV/c$	738'871	1'284'811	
$Q_L^{rec} < 2MeV/c$, $Q_T^{rec} < 8MeV/c$	$147'203 \pm 153$	$2'358'312 \pm 73$	$6'675 \pm 7$

Table 5.2: Number of generated and reconstructed atomic and Coulomb-pairs for $Q_L^{rec} < 2$ MeV/c and $Q_T < 8$ MeV/c and the corresponding experimental k-factor k^{exp} (taking into account the acceptance and inefficiencies of the setup).

The next step consists in the determination of the breakup probability using equ.(5.12). Table 5.3 summarizes the latter for the different fits described in the last section. The results are in agreement.

Target	Type of fit	Fit var.	P_{br}	τ_{1S}
Ni-94 μm	without atomic shape	Q_L	$(43.3 \pm 3.4)\%$	$2.58^{+0.61}_{-0.50}$
Ni-94 μm	with atomic shape	Q_L	$(40.0 \pm 3.3)\%$	$2.10^{+0.48}_{-0.38}$
Ni-94 μm	with atomic shape	Q_L, Q_T	$(38.7 \pm 2.5)\%$	$1.92^{+0.34}_{-0.26}$
Ni-98 μm	without atomic shape	Q_L	$(38.5 \pm 7.8)\%$	$1.88^{+1.00}_{-0.88}$

Table 5.3: Measured P_{br} for the 94 μm target and the associated mean life τ_{1S} obtained using the relation plotted in fig. 5.16 for different fitting techniques. The results for the 98 μm target are also shown.

Finally, as discussed in section 1.3 one can calculate numerically the breakup probability P_{br} as a function of the mean life using equ.(1.15). Fig. 5.16 shows this relation for the Ni 94μm target and for $\pi\pi$-atoms. The mean life τ_{1S} of $\pi\pi$-atoms in the 1S state, is listed in the last column of table 5.3. For the Ni 98 μm target, similarly to fig. 5.16 a relation between P_{br} and τ_{1S} has been simulated. The two first fits along Q_L only, are in agreement with the published results from DIRAC using the complete upstream tracking [1], i.e.

$$\tau_{1S} = 2.91^{+0.49}_{-0.62} \text{ fs}.$$

While for the Q_L, Q_T fit, the mean life is slightly low compared to the published one. This shift comes from events with high Q_T. Cutting in the event selection at $Q_T = 4$ MeV/c moves the average mean life up. This illustrates that the method in the transverse plane is still not perfect. Either multiple scattering introduces a bias

in Q_T or other physical processes contaminate events with high Q_T. Although, the MC has been considerably improved, small discrepancies are still present. However, a fit along Q_L only provides a good estimate of τ_{1S} using only downstream detectors. Also, the statistical errors are comparable to the published ones, proving an excellent background suppression.

To conclude this part, the downstream tracking procedure is quite satisfactory for Q_L, but for Q_T the resolution is strongly affected by multiple scattering. The upgrade of the setup should not affect the downstream tracking, especially because the new Čerenkov detectors are located behind the tracker (DC). This leads to the conclusion that one has an operational reconstruction method for the 2007 data sample without upstream detectors. Furthermore, the interpolation methods avoid the vertex cut and therefore permits an increase in the number of detected atoms by 85% in the same data sample [1].

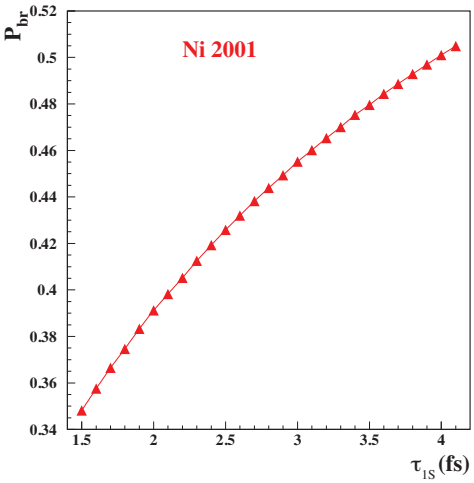

Figure 5.16: Breakup probability P_{br} for a 94 μm Ni-target as a function of the mean life of $\pi\pi$-atoms in the 1S state.

5.4 Analysis of the 2007 data sample

Before starting the πK analysis, I apply the technique for $\pi\pi$-atoms discussed above to the 2007 data sample taken with a dense Pt-target which improves the breakup probability. The aim of this analysis is to crosscheck that the new downstream tracking has not been affected by the upgrade of the setup and is therefore ready for the πK-search. Due to the low production rate of πK-atoms only the one dimensional fit along Q_L is used to keep the number of entries per bin reasonably high. Also, this fit provides the most reliable results. The two different fit techniques described in section 5.2 were applied, with and without atomic shape. The results

of the latter fit are shown in fig. 5.17(a) and the residuals between data and fitted background in fig. 5.17(b). For the fit with atomic shape the results are shown in fig. 5.18. The fit results are summarized in table 5.4.

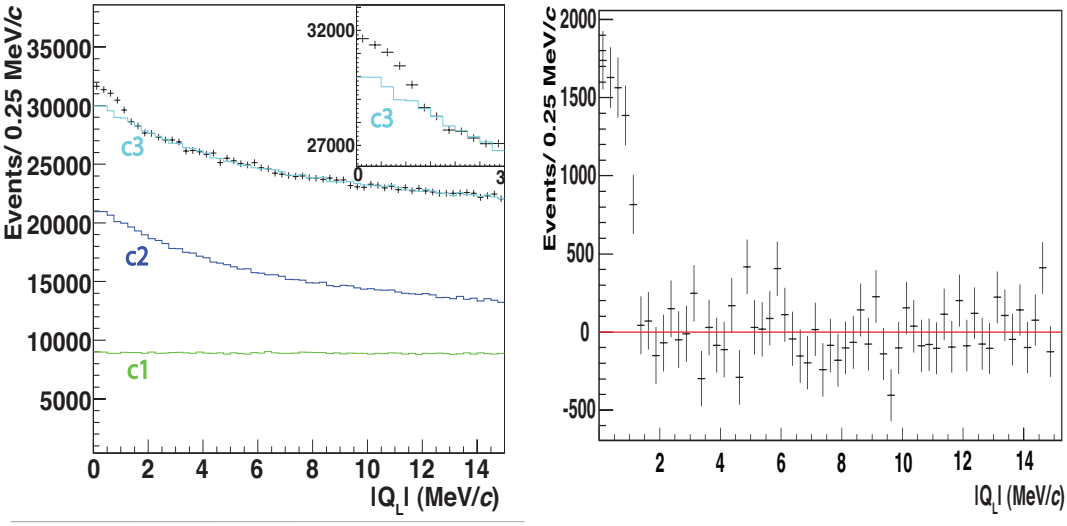

(a) (b)

Figure 5.17: (a): $|Q_L|$ distribution for the 28 μm Pt data (points with error bars in black) and the fitted background for simulated non-Coulomb in green (c1) and for simulated Coulomb-pairs in blue (c2). The total simulated background is plotted in turquoise (c3). The excess of data for low $|Q_L|$ is the signal. The inset is a close-up view of the signal region. (b): Residuals of the data and the fitted background contribution.

These results demonstrate that the elaborated technique for atom extraction is still valid on the 2007 data sample. However, the MC for the background description, is the one used for the 2001 data sample without taking into account the upgrade of the setup. Furthermore, the Ni-target during the 2001 run is less dense than the 2007 Pt-target. Therefore, the results shown in table 5.4 are preliminary. Nevertheless, fig. 5.17(b) demonstrate that the background description is under control since the residuals are flat above 2 MeV/c.

target	fit technique	fit variable	$\chi^2/ndof$	β	n^A, α
Pt-28 μm	without atomic shape	Q_L	65.7/50	$159'639 \pm 2'367$	$7'098 \pm 533$
Pt-28 μm	with atomic shape	Q_L	79.1/57	$160'292 \pm 1'992$	$6'945 \pm 513$

Table 5.4: Fit parameters and number of extracted atoms for the 2007 data sample for different fits. The errors on β and α (for the fit with atomic shape) are calculated with MINOS, while the errors on n^A for the fit without atomic shape are the square root of the data.

For k^{exp}, since no MC is existing, I use the 2001 simulation. The efficiency of the setup has not changed for $\pi\pi$-pairs during the upgrade and therefore the k^{exp}

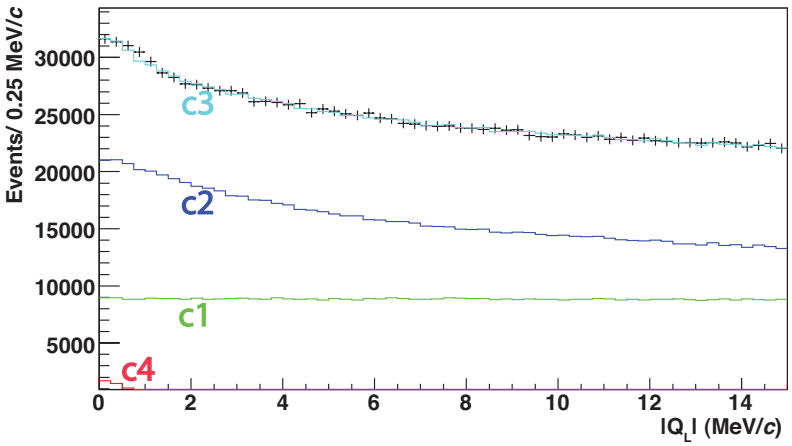

Figure 5.18: $|Q_L|$ distribution for data (points with error bars in black), fitted background for simulated non-Coulomb in green (c1) and for simulated Coulomb-pairs in blue (c3). In addition to the fit without the atomic shape, the simulated $\pi\pi$-atom distribution is plotted in red (c4). The total simulated background is plotted in turquoise (c3). The total MC contributions, the sum of signal and background, is plotted in turquoise (c3).

should not be affected. The resulting breakup probability is summarized in table 5.5.

Target	Type of fit	Fit var.	P_{br}
Pt-28 μm	without atomic shape	Q_L	$(61.7 \pm 5.8)\%$
Pt-28 μm	with atomic shape	Q_L	$(60.7 \pm 4.9)\%$

Table 5.5: Measured P_{br} for two different fit techniques: with and without atomic shape.

For $\pi\pi$-atoms, the relation between the breakup probability and the distribution has not been simulated yet for the 2007 Pt-target, all efforts for the 2007 run being focused on the πK-analysis. However, around 7000 $\pi\pi$-atoms were observed. Such an encouraging result is enough motivation to start the search for πK-atoms, even without upstream detectors.

Chapter 6

Data analysis: Search for πK-atoms

The aim of this chapter is to apply the technique trained on the $\pi\pi$-data sample to search for πK-atoms, which have not been observed so far. This work was the main goal of the DIRAC-II experiment and of this thesis. I will discuss only the one dimensional fit along Q_L which is more reliable than Q_T due to multiple scattering in the upstream detectors as described earlier with the 2001 data. Also, due to the small production rate of kaons, πK-atoms are much less abundant than $\pi\pi$-atoms. Fitting in two dimensions (including the transverse plane) reduces the number of entries per bin, which are already very low in the 2007 data.

6.1 Kinematics of πK-atoms

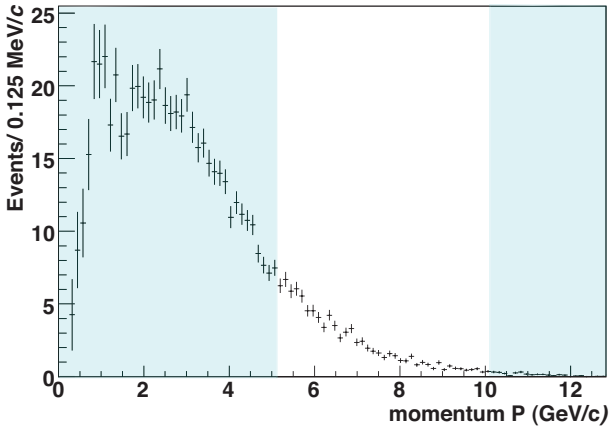

Figure 6.1: Momentum distribution in the laboratory system for πK-atoms simulated with Fritiof 6.0. The shaded regions are rejected by cuts in the further event selection.

Estimation of the momentum distribution at production for πK-atoms have been performed using Fritiof 6.0. This distribution (fig. 6.1) does not take into account reconstruction or trigger efficiencies nor the acceptance function of the setup. The shaded region is rejected. The upper limit is set to reduce the background, while the lower limit comes from the acceptance of the setup. Particles originating from the breakup of πK-atoms have in the center of mass system a very low momentum p^* (fig. 1.2). Therefore, for p_π, p_K and p_A, the momentum in the laboratory system of the pion, kaon and atom respectively, one obtains the following relations

$$\frac{p_\pi}{p_K} \simeq \frac{m_\pi}{m_K},$$
$$\frac{p_\pi}{p_A} \simeq \frac{m_\pi}{m_A}.$$

One can use these properties to rescale the momentum distribution in fig. 6.1 to obtain the ones of the pions and kaons from the breakup of πK-atoms (fig. 6.2(a) and (b) respectively). Pions with a momentum below 1.2 GeV/c have a trajectory outside the acceptance of the spectrometer (fig. 2.7), which sets the lower limit on the range of detected atoms.

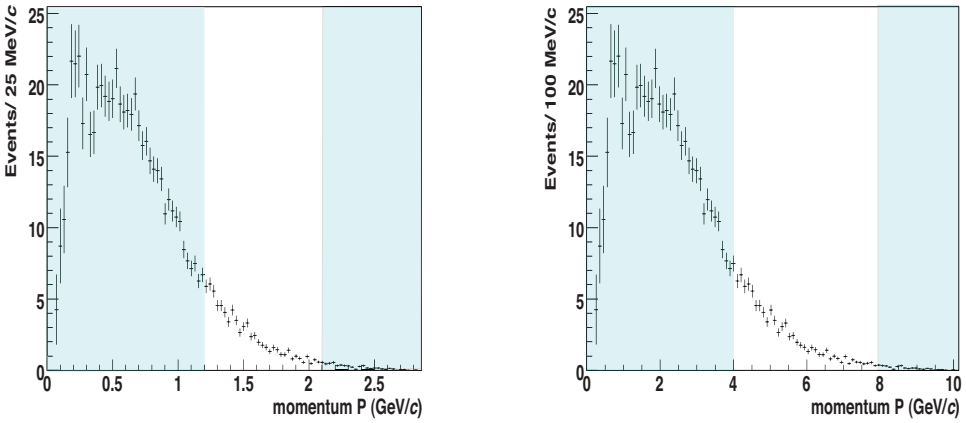

(a) (b)

Figure 6.2: Momentum distribution in the laboratory system for pions (a) and kaons (b) originating from the breakup of πK-atoms. The shaded regions are rejected by acceptance and cuts in the further event selection.

6.2 Event selection

In this chapter events are selected by the πK-trigger described in section 2.4. Prompt and accidental-pairs are extracted from the data using the time difference Δt between the positive and negative arms in the VH. Both types of events have then to satisfy the following criteria:

- no electrons nor positrons (anti-coincidence with Ch in the left and right arm),

- no muons (anti-coincidence with Mu),
- one drift chamber track per arm,
- $|Q_L| < 20$ MeV/c,
- $Q_T < 8$ MeV/c,
- the momentum of the kaon is larger than 4 GeV/c and smaller than 8 GeV/c,
- the momentum of the pion is larger than 1.2 GeV/c and smaller than 2.1 GeV/c.

6.3 $\pi^- K^+$ analysis

6.3.1 Overview

For the $\pi^- K^+$-data sample the TDC of the aerogel was used in addition to remove protons in the positive arm[1]. For events with a momentum below 5.3 GeV/c a time correlated hit is required in H1 or H2, while for events with a momentum above 5.3 GeV/c a time correlated hit is required in L1 instead. In the negative arm backgrounds from antiprotons and negative kaons are negligible.

A rough overview of the πK analysis is given in a flow diagram (fig. 6.3). The numbers of non-Coulomb and Coulomb-pairs (β) are obtained by a fit to prompt events outside the signal region. The number of atomic-pairs (n^A) is derived from the residuals between the prompt events and this fit, extrapolated to the signal region. The theoretical k-factor (k^{th}) which correlates the number of Coulomb-pairs with $|Q| < 3$ MeV/c to the number of produced atoms (N^A) is corrected using MC to take into account the acceptance function of the DIRAC-II experiment. The breakup probability $P_{br} = n^A/N^A$ can then be calculated. Details are given in the following sections.

6.3.2 Monte-Carlo simulation and k^{exp} measurement

For the determination of the experimental k-factor (k^{exp}) MC is asked, although the MC is not perfect. k^{exp} is defined in equ.(5.13) as:

$$k^{exp} \equiv k^{th} \cdot \frac{N^C(Q^{initial} < 4 \cdot p_B)}{n_i^A} \cdot \frac{n^A(Q_L^{cut},\ Q_T^{cut})}{N^C(Q_L^{cut},\ Q_T^{cut})}, \tag{6.1}$$

where $k^{th} = 0.615$ for $\Omega = 4 \cdot p_B$. For πK-atoms rounding down to the closest bin, one gets $4 \cdot p_B = 3.0$ MeV/c (instead of 2 MeV/c for $\pi\pi$-atoms). For the πK analysis I used for the signal region $Q_L^{cut} < 3$ MeV/c and $Q_T^{rec} < 8$ MeV/c.

[1] As already mentioned in section 4.4, for the 2007 πK analysis only informations from the TDC could be used.

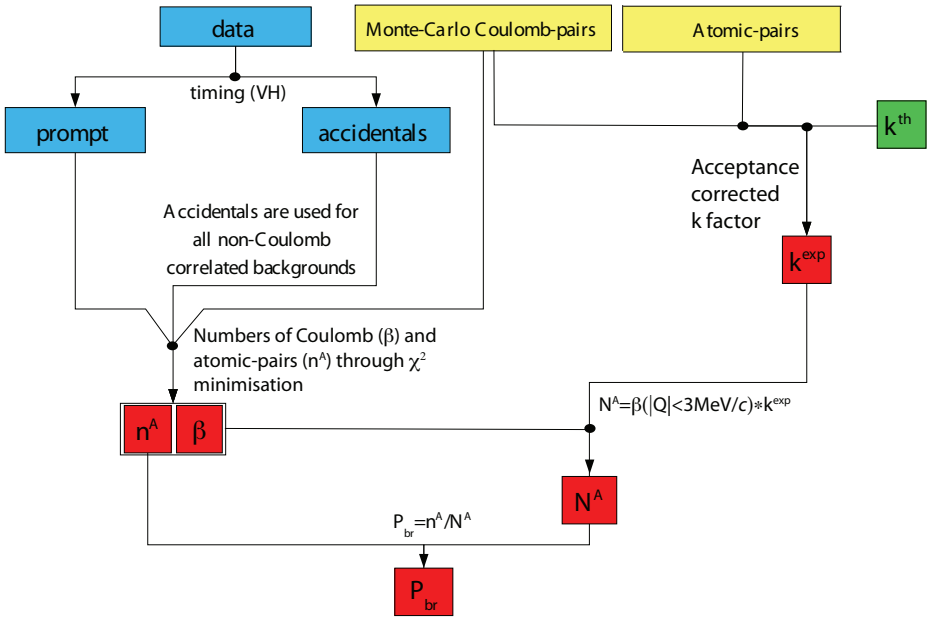

Figure 6.3: Flow diagram illustrating the different steps of the further analysis. Blue boxes are using only information from data, yellow ones from MC and green ones from theory. For the red boxes, information from all three types are needed.

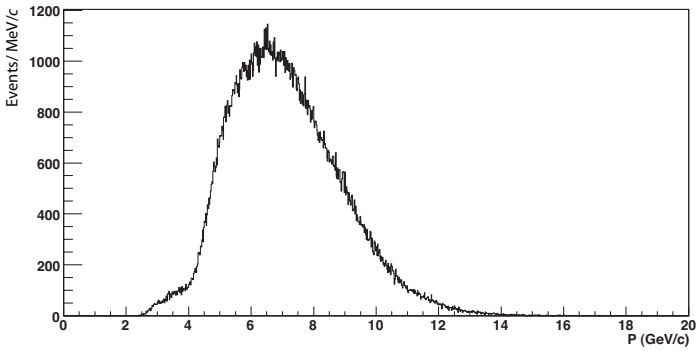

Figure 6.4: Total inclusive $\pi^- K^+$ momentum distribution at the target obtained from the measured data and corrected by the acceptance function of the setup. For background from $\pi^- p$ and $\pi^- \pi^+$ see text.

k^{exp} depends on the numbers of generated and reconstructed Coulomb and atomic-pairs, which have to be simulated. The main difference between the simulation of $\pi^-\pi^+$ and π^-K^+ Coulomb-pairs comes from the generator DIPGEN (section 2.5). This generator needs as input the total inclusive π^-K^+-momentum distribution at production (fig. 6.4), which can be obtained from the measured inclusive π^-K^+ spectrum corrected by the acceptance function of the setup. This measurement is contaminated by π^-p and $\pi^-\pi^+$-pairs, but tests demonstrated that the Q_L distribution is not sensitive to changes in the momentum distribution. Other uncertainties in the MC production compared to the previous $\pi\pi$ analysis are originating from the upgrade of the spectrometer and the implementation of these changes in GEANT-DIRAC, which are not simulated perfectly yet. Nevertheless, no significant corrections are expected and the Q_L distribution used in the further analysis is shown in fig. 6.5(a).

The MC for atomic-pairs is still missing. Nevertheless, the production mechanism for Coulomb-pairs and atoms is very similar. The main difference is the low Q distribution of atomic-pairs (fig. 1.2). Therefore, I decided to simulate Coulomb-pairs with $Q < 3$ MeV$/c$ and to treat them as atomic-pairs. Furthermore, the main effect on the distributions comes from multiple scattering in the target which affects both type of events. The reconstructed $|Q_L|$ distribution is shown in fig. 6.5(b). For the following analysis this distribution represents a good approximation of the atomic-pairs distribution.

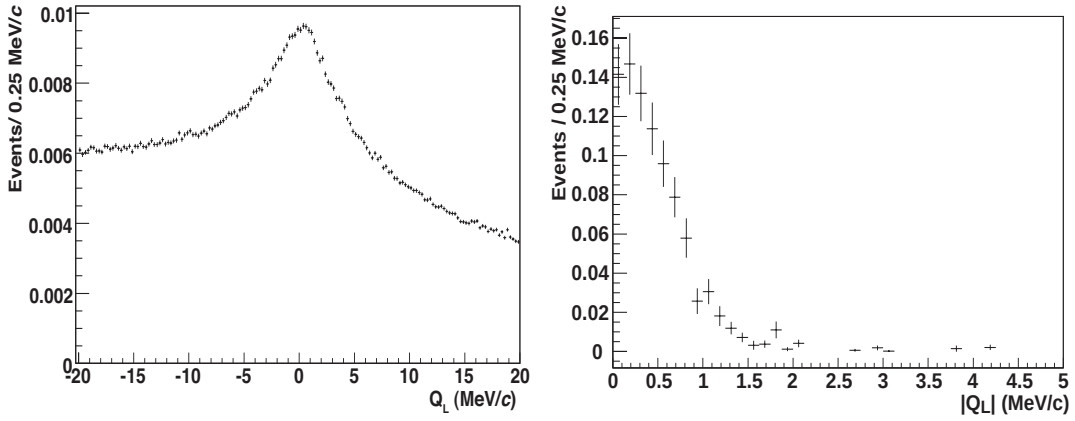

(a) (b)

Figure 6.5: (a): Simulated Q_L distribution for Coulomb-pairs normalized to one for $|Q_L| < 20$ MeV$/c$. (b): $|Q_L|$ distribution for reconstructed Coulomb-pairs which have an initial generated relative momentum below 3 MeV$/c$.

The Q_L distribution for Coulomb-pairs is determined by the MC and the fraction of Coulomb-pairs $f_C = (28.7 \pm 6.8)\%$ for prompt events with $3 < |Q_L| < 20$ MeV$/c$ is fixed from the minimization of the χ^2 defined in equ.(6.2). Prompt-pairs are either Coulomb correlated (f_C) or uncorrelated ($1 - f_C$). The latter event type can be described by accidentals (see section 6.3.3). Therefore, subtracting from

the prompt π^-K^+ momentum distribution $(1 - f_C)$ the momentum distribution of accidentals, one obtains the momentum distribution of Coulomb-pairs. This extracted distribution can then be compared with the simulated one, which provides a good test of the MC. Fig. 6.6(a) illustrates the normalized ratio MC over data for the total momentum distribution of Coulomb-pairs. This disagreement can be explained by the contamination of π^-p-pairs with higher momenta in the total inclusive π^-K^+ momentum distribution (fig. 6.4). Due to the small amount of high energy Coulomb-pairs, fluctuations in the last bins are very large and only the momentum range between 5.1 and 8 GeV/c is considered.

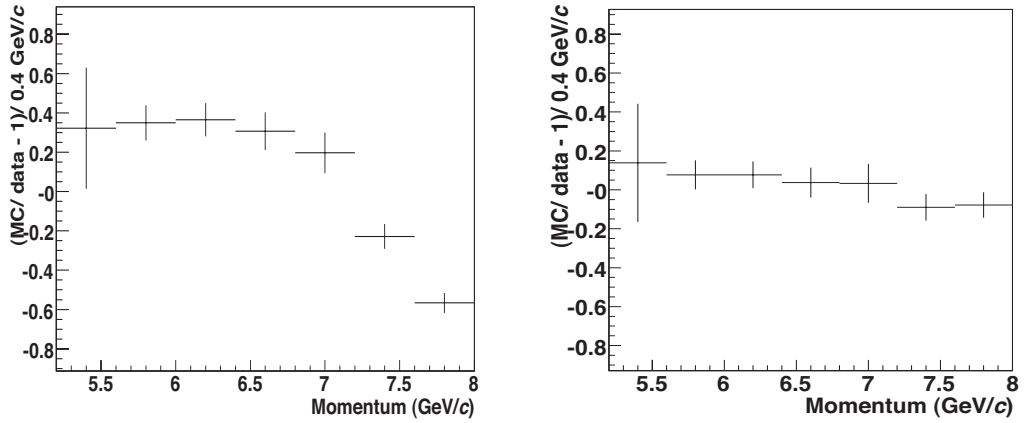

(a) (b)

Figure 6.6: Ratio (MC/data-1) for the momentum distribution of Coulomb-pairs before (a) and after corrections (b).

Using this distribution one can re-weight the πK momentum distribution for the Coulomb background to correct the MC. Fig. 6.6(b) shows the same distributions after corrections. Even if the fluctuations remains strong the systematic effect cancels out. This corrected distribution is used in further analysis. However, in the near future for a more precise generation of MC π^-K^+-events, the total inclusive π^-K^+ momentum distribution will be simulated using Fritiof 6.0.

With the MC described above, k^{exp} has been calculated using $3 \cdot 10^7$ MC events for the Coulomb-pairs and $2.3 \cdot 10^4$ atomic-pairs. Results are summarized in table 6.1.

	n^A	N^C	$k^{exp} \times 10^4$
Total prod.		30'000'000	
Prod. with $Q^{init} < 3.0$ MeV/c	23'074	222'441	
Q_L^{rec} <3MeV/c, Q_T <8 MeV/c	782 ± 5	$41'868 \pm 8$	$2'307 \pm 7$

Table 6.1: Detected and reconstructed atomic (n^A) and Coulomb-pairs (N^C) and the associated experimental k-factor.

6.3.3 Background description

Similarly to the $\pi\pi$ analysis the background consists of Coulomb (C), non-Coulomb (nC) and accidental-pairs (acc). Due to the small kaon production cross section compared to protons and pions, despite a good particle identification, we have to take into account contamination from $\pi^- p$ and $\pi^-\pi^+$-pairs, where a proton, respectively a pion, has been misidentified as a kaon. The relative momentum Q_L has been reconstructed attributing a wrong mass to one of the particles.

A $\pi^-\pi^+$ contamination occurs when a π^+ fakes a K^+ so that a signal has been registered in one of the aerogel modules but not in the heavy gas detector (ChF). This can be due to inefficiencies in ChF or missing particles which were absorbed or scattered in the magnetic shielding surrounding the aerogel modules. One way to estimate the fraction of $\pi^-\pi^+$-pairs in the $\pi^- K^+$ data sample is to generate pions by MC and to measure the number of surviving particles when ChF is used in anti-coincidence. Unfortunately, the simulation of this detector was in a very preliminary state and could not be used.

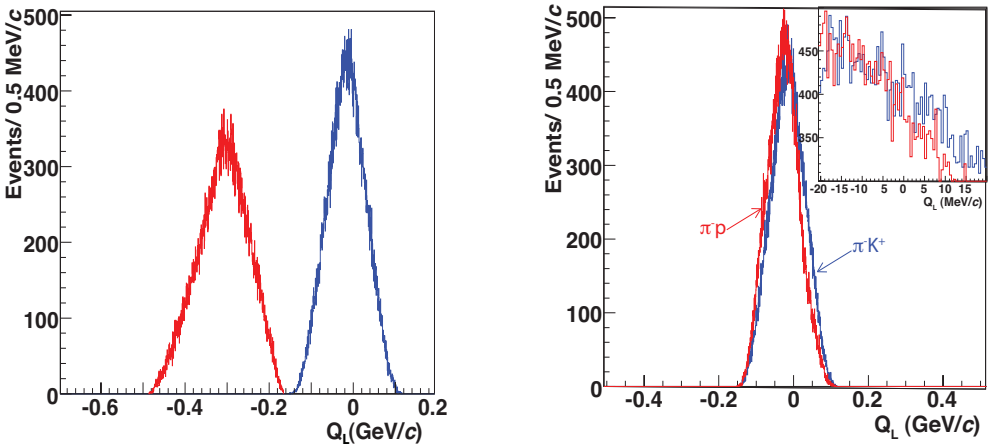

(a) (b)

Figure 6.7: Q_L distribution for accidental pairs extracted from data. (a): In red (left) is the distribution of misidentified $\pi\pi$-pairs and in blue (right) "real" $\pi^- K^+$-pairs. For the Q_L calculation, the mass of a kaon has been attributed to the positive particle and the mass of a pion to the negative one. (b): In red is the distribution of misidentified $\pi^- p$-pairs and in blue is the distribution of "real" $\pi^- K^+$-pairs. The two distributions are locally similar and can be approximated by a linear dependence.

Therefore, I selected $\pi^- K^+$-pairs using the aerogel detector in coincidence for the positive kaons, and for the negative pions I neglected contributions from kaons or antiprotons. In addition I selected $\pi^-\pi^+$-pairs by requiring ChF in the left arm in coincidence (instead of in anti-coincidence as it is the case for the normal $\pi^- K^+$-trigger, see section 2.4). For both types of pairs ($\pi^- K^+$ and $\pi^-\pi^+$), I selected accidental-pairs using the VH to ensure that they were not Coulomb correlated. Then, for both types of accidental-pairs I measured the momentum distribution of

the two particles. Following equ.(5.3) I reconstructed the Q_L distribution assigning for both event types the mass of a kaon to the positive particles and the mass of a pion to the negative ones. Fig.6.7(a) shows the Q_L distribution for the misidentified $\pi^-\pi^+$-pairs in red and the "real" $\pi^- K^+$-pairs in blue. The two distributions are not overlapping and one can conclude that the contamination from misidentified $\pi^-\pi^+$-pairs has no influence on the further analysis.

A $\pi^- p$ contamination is due to protons giving a signal in the aerogel modules. The TDC of the aerogel detector has been tuned to remove 95% of the protons (section 4.4). This can be crosschecked with events in the Λ-peak. Protons from the latter decay have a wide momentum distribution which covers the proton range of the DIRAC-II experiment. Fig. 6.8 shows the invariant $\pi^- p$ mass in the range where the Λ-peak is expected, without (a) and with (b) the use of the aerogel detector in coincidence. Counting the number of events in the peak with and without the use of the aerogel detector gives the fraction of rejected protons, $(93 \pm 3)\%$. Due to the dominance of protons over kaons [64], one obtains a contamination from protons of 25 – 30%.

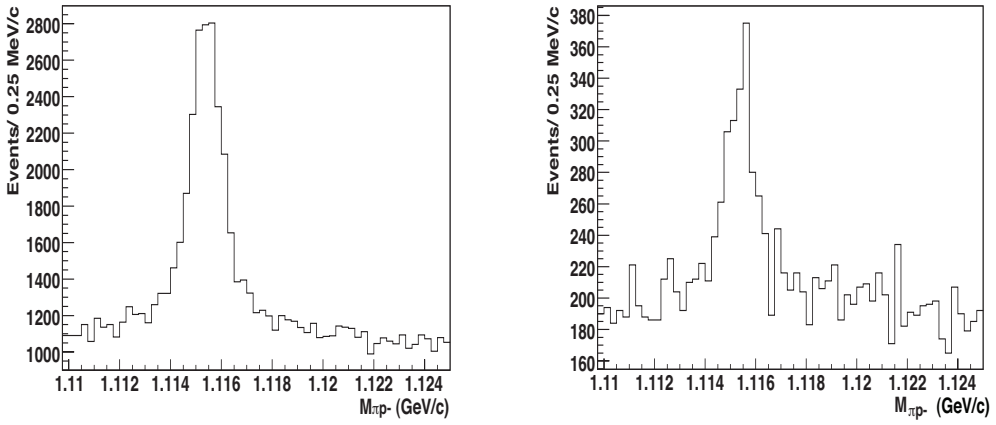

(a) (b)

Figure 6.8: Invariant $\pi^- p$ mass without (a) and with (b) the use of the aerogel detector in coincidence. The peak corresponds to the Λ-resonance.

To estimate the impact of this contamination on the further $\pi^- K^+$ analysis, I selected again $\pi^- K^+$-pairs using the aerogel detector in coincidence for the positive particles and $\pi^- p$-pairs using the aerogel detector in anti-coincidence for proton identification. For both event types I selected accidentals using the VH. The Q_L distribution was then calculated attributing to the positive particles the mass of a kaon and to the negative ones the mass of a pion. Fig. 6.7(b) shows the Q_L distribution in blue for $\pi^- K^+$-pairs and in red for misidentified $\pi^- p$-pairs. In the region of interest, i.e. for $|Q_L| < 20$ MeV$/c$ the two distributions are similar and one can treat them as one unique source of background described by a linear dependence. This assumption remains valid only for the 2007 data sample, where differences in the distributions are diluted in the statistical fluctuations.

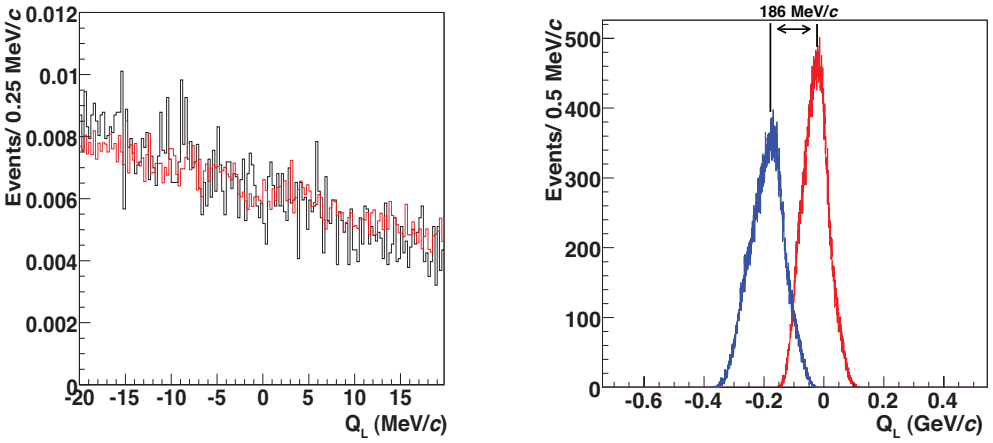

(a) (b)

Figure 6.9: (a): Q_L distribution for accidental $\pi^- K^+$-pairs extracted from data in black and for simulated non-Coulomb $\pi^- K^+$-pairs in red. (b): Q_L distribution for accidental-pairs extracted from data for "real" $\pi^- p$-pairs in blue (left) and misidentified $\pi^- p$-pairs in red (right), assigning to the proton the mass of a kaon.

Misidentified $\pi^- p$-pairs are present for accidentals, but also for prompt events, i.e. Coulomb and non-Coulomb-pairs. The latter event type should have, according to the $\pi\pi$-analysis, the same distribution than accidentals (fig. 5.10). For the $\pi^- K^+$ analysis, I reproduced the same distributions (fig. 6.9(a)) to verify this property. To do so, I simulated using the preliminary version of GEANT-DIRAC the Q_L distribution of non-Coulomb $\pi^- K^+$-pairs (red) and compared it with the accidental distribution extracted from data (black). The two distributions have the same linear dependence. Therefore one can conclude that accidentals and non-Coulomb $\pi^- p$ and $\pi^- K^+$-pairs have within the statistical fluctuations the same distribution which can be approximated by a linear shape.

Let us now consider $\pi^- p$ Coulomb-pairs. They have the same Q_L distribution as non-Coulomb-pairs apart from an enhancement at low Q_L due to the Coulomb correlation. Fig. 6.9(b) shows the Q_L distribution for accidental $\pi^- p$-pairs correctly (blue) and wrongly reconstructed (red), by assigning to the proton the mass of a kaon. The shift of the distribution is 186 ± 2 MeV/c. If an excess would occur for low Q_L due to $\pi^- p$ Coulomb-pairs, it would be shifted out of the region of interest due to the wrong mass assignment. Therefore, these events can be treated as non-Coulomb-pairs.

Hence, contamination from $\pi^- p$-pairs, non-Coulomb $\pi^- K^+$-pairs as well as accidentals (including $\pi^- p$ and $\pi^- K^+$-pairs) can be treated as one single background contribution and the distribution in Q_L can be approximated by a linear dependence. It is therefore natural to describe all these backgrounds with accidentals extracted from data.

6.3.4 Detection of Coulomb-pairs

A first exciting result is the detection of $\pi^- K^+$ Coulomb-pairs. They have never been measured so far and they are correlated to the number of atoms through k^{exp} defined in equ.(6.1). The aim of this measurement is instead of resorting to MC calculations, to obtain this event type directly from the data.

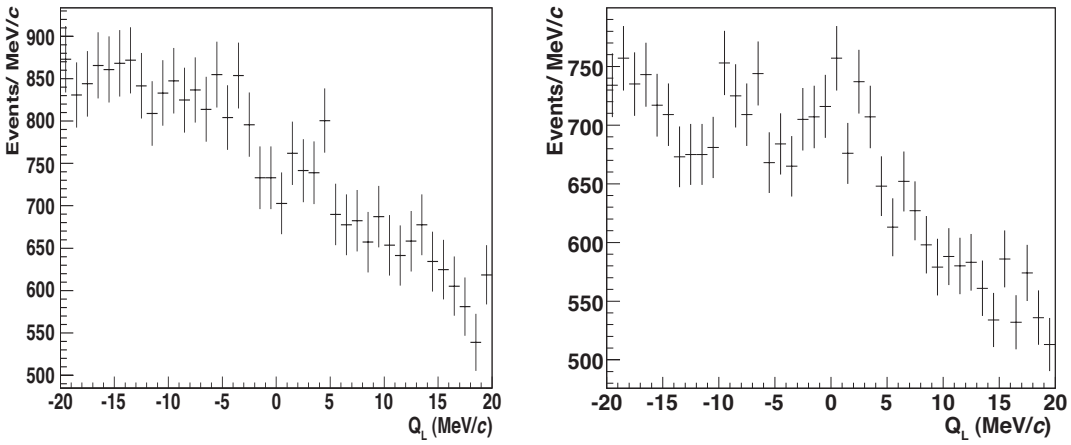

(a) (b)

Figure 6.10: Q_L distribution for normalized accidentals (a) and prompt-pairs (b).

To extract Coulomb-pairs, events are selected using the time difference between the left and right spectrometer arm measured by the VH: accidentals are between -12 and -6 ns, while prompt-pairs are between -0.5 and 0.5 ns (fig. 4.9). For both event types (accidentals and prompt-pairs) one measures their Q_L distribution (fig. 6.14(a) and (b) respectively) and divide the former by the latter. The resulting histogram is shown in fig. 6.11. Since all prompt contributions, except for Coulomb-pairs (and atomic-pairs), have the same Q_L distribution than accidentals, the non-flat distribution of the resulting histogram is the first proof of the existence of Coulomb correlated $\pi^- K^+$-pairs. In the signal region, i.e. for $|Q_L| < 3$ MeV/c, 768 ± 225 $\pi^- K^+$ Coulomb-pairs could be observed using only information from data without the use of MC.

Alternatively, for the red solid line, I used the simulated Coulomb-pairs and divided their Q_L distribution (fig. 6.5(a)) by accidental-pairs extracted from data (fig. 6.14(a)). The number of Coulomb-pairs β in the obtained distribution is then fixed by fitting the histogram in fig. 6.11. I obtained $\beta = 721 \pm 154$ $\pi^- K^+$ Coulomb-pairs in agreement with the previous measurement. Errors are smaller with this procedure, but this measurement implies the use of MC.

6.3.5 Fit function and results

As for the $\pi\pi$ analysis, I use a binning of 0.25 MeV/c in Q_L. Since the atomic Q_L distribution is not known precisely, I fit without atomic shape outside the signal

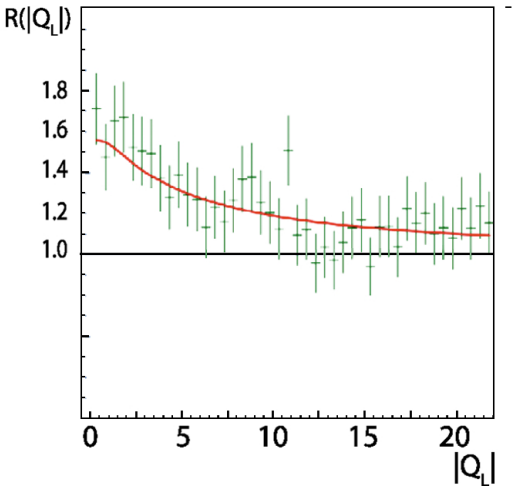

Figure 6.11: Correlation R as a function of $|Q_L|$ for $\pi^- K^+$-pairs. The deviation for low $|Q_L|$ from the horizontal line proves the existence of Coulomb correlated $\pi^- K^+$-pairs. The red (solid) line is simulated.

region, i.e. $|Q_L| > 3$ MeV/c (fig. 1.3). Taken into account the background described above, one can rewrite the χ^2 defined in last chapter (equ.(5.10)) for a fit in $|Q_L|$ as:

$$\chi^2 \equiv \sum_{i=13}^{80} \left(\frac{\frac{dN^{prompt}}{dQ_{L,i}} - \beta \cdot \frac{dN^C}{dQ_{L,i}} - (N^{prompt} - \beta) \cdot \frac{dN^{acc}}{dQ_{L,i}}}{\sigma_i^{meas}} \right)^2 , \qquad (6.2)$$

where $\frac{dN^C}{dQ_{L,i}}$ are the predicted probabilities of Coulomb-pairs (MC) to be in bin $dQ_{L,i}$, $i = 13, .., 80$. For accidentals, $\frac{dN^{acc}}{dQ_{L,i}}$ is extracted from data and normalized to one in the region of interest. $\frac{dN^{prompt}}{dQ_{L,i}}$ are the number of measured prompt-pairs per bin $dQ_{L,i}$ and are not normalized. β and $(N^{prompt} - \beta)$ are the numbers of Coulomb correlated and uncorrelated-pairs respectively, including contamination from y $\pi^- p$-pairs.

Fig. 6.12(a) shows the fit result from the minimization of the χ^2. In blue (c2) is the contribution of Coulomb-pairs and in green (c1) of all other event types. The total background is shown in turquoise (c3). The residuals between data and MC are shown in fig. 6.12(b). Outside the signal region the residuals are within the fluctuations flat proving a good understanding of the background. Even if the significance remains small, evidence for an enhancement at low $|Q_L|$ can be observed. This is the first ever observed sign for the existence of $\pi^- K^+$-atoms. The fit results are summarized in the first line of table 6.2. The first column describes the type of atoms, the second one gives the χ^2/ndof for the minimization of the χ^2 defined in equ.(6.2). The third column shows the number of detected Coulomb-

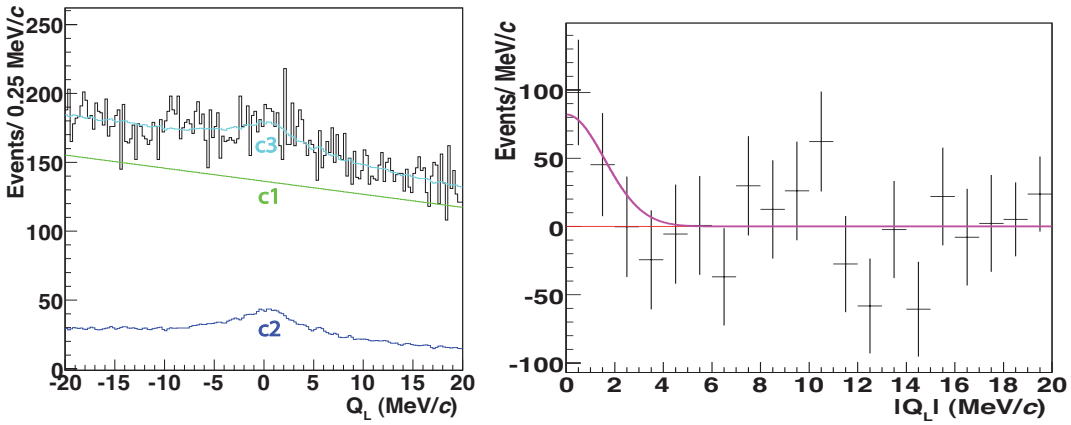

(a) (b)

Figure 6.12: (a): Q_L $\pi^- K^+$ distribution for the Pt-28 μm data (black histogram) and the fitted background for non-Coulomb in green (c1) and for Coulomb-pairs in blue (c2). The total background is plotted in turquoise (c3). The excess of data for low Q_L is the signal. (b): Residuals of the data and the fitted background contribution. A Gaussian fit has been applied in pink (solid line) to illustrate the distribution of atomic-pairs.

pairs β obtained from the fit, while the last column shows the number of measured atomic-pairs by counting the bin content of the residual Q_L distribution.

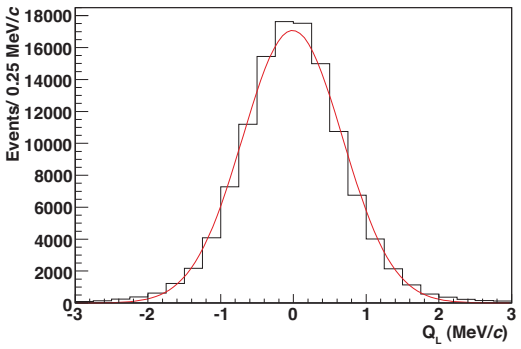

Figure 6.13: Simulated Q_L distribution for $\pi\pi$ atomic-pairs and a Gaussian fit in red (solid line). The two distributions are in perfect agreement.

For a parameterization of the Q_L distribution for $\pi^- K^+$ atomic-pairs one can rely on the $\pi\pi$-analysis. Fig. 6.13 compares the simulated Q_L distribution for $\pi^-\pi^+$ atomic-pairs to a Gaussian fit. The two distributions are in perfect agreement. Therefore, I use for the Q_L distribution of $\pi^- K^+$ atomic-pairs a Gaussian distribution with a free width. In fig. 6.12(b), a Gaussian fit has been applied in pink (solid line) to illustrate their distribution, leading to 138.5 ± 67.3 atomic-pairs. The fit parameters are fixed using only 3 – 4 bins and therefore fit results are not used

for further analysis due to large uncertainties.

atom type	χ^2/ndof	β	n^A
π^-K^+	122.0/130	$4'215 \pm 1'008$	143 ± 53
π^+K^-	164.1/130	$1'356 \pm 396$	29 ± 15

Table 6.2: Summary of the number of detected atoms and Coulomb-pairs for π^-K^+ and π^+K^-. The errors on β are calculated with MINOS, while the errors on n^A are the square root of the data.

6.4 π^+K^- analysis

For the π^+K^- data sample an additional cut is required: the time difference between the negative and the positive arm measured with the VH has to be negative in order to remove protons faking pions. Due to the good time resolution of the VH this separation is possible for pions, kaons and protons below 2.5 GeV/c using the TOF technique (fig. 4.9).

Since the Q_L distribution $\frac{N(Q_L(\pi^+K^-))}{dQ_L}$ follows, according to equ.(5.3), the symmetry relation:

$$\frac{N(Q_L(\pi^+K^-))}{dQ_L} = \frac{N(-Q_L(\pi^-K^+))}{dQ_L}, \tag{6.3}$$

one can use the features of the π^-K^+ analysis. Therefore, misidentified $\pi^+\pi^-$-pairs reconstructed as π^+K^- have a Q_L distribution which is not overlapping with "real" π^+K^--pairs and hence do not need to be taken into account. Additionally, misidentified $\pi^+\bar{p}$-pairs have in the region of interest the same distribution in Q_L than π^+K^--pairs and only their non-Coulomb contribution has to be considered. Anyway, due to the strong suppression of antiprotons [64] this contamination can be neglected. Also, accidentals and non-Coulomb-pairs have the same distribution in Q_L, described by a linear dependence and therefore, apart from Coulomb-pairs all background contributions are described by the accidental Q_L distribution extracted from data.

Before searching for π^+K^--atoms, I first extract Coulomb-pairs, as for the charge conjugated case. Dividing the Q_L distribution for prompt events (fig. 6.14(a)) by accidental ones (fig. 6.14(a)), one gets the correlation function (fig.6.15) proving the existence of π^+K^- Coulomb-pairs. In the signal region, 285 ± 134 π^+K^- Coulomb-pairs are observed without the use of MC. The red (solid) line is simulated.

For π^+K^--atoms, fig. 6.16 shows the fit results (a) using the χ^2 defined in equ.(6.2). Again in blue (c2) is the contribution of Coulomb-pairs and in green (c1) the other contributions. The total background is shown in turquoise (c3). The residuals are shown in fig. 6.16(b). A Gaussian fit has been applied in pink (solid line) leading to 21.8 ± 15.1 atomic-pairs. Results of this analysis are summarized

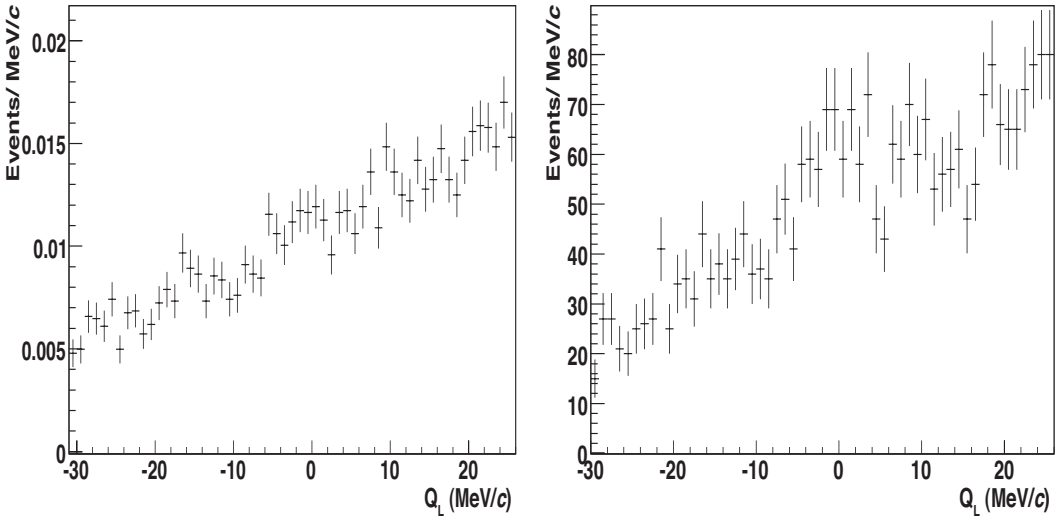

(a) (b)

Figure 6.14: Q_L distribution for normalized accidentals (a) and prompt-pairs (b).

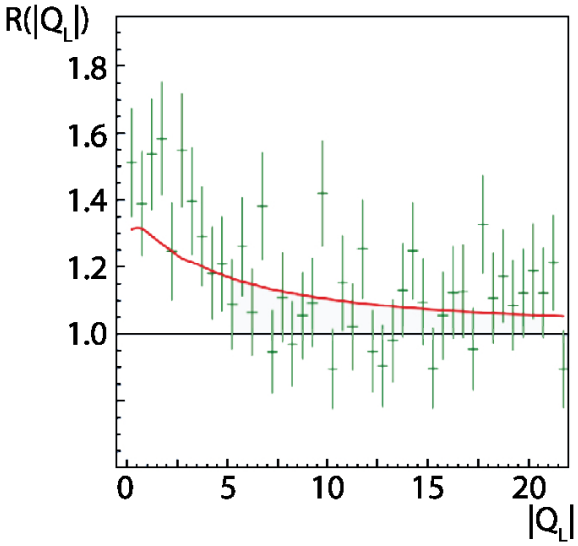

Figure 6.15: Correlation R as a function of $|Q_L|$ for π^+K^-. The deviation for low $|Q_L|$ from the horizontal line proves the existence of Coulomb correlated π^+K^--pairs. The red (solid) line is simulated.

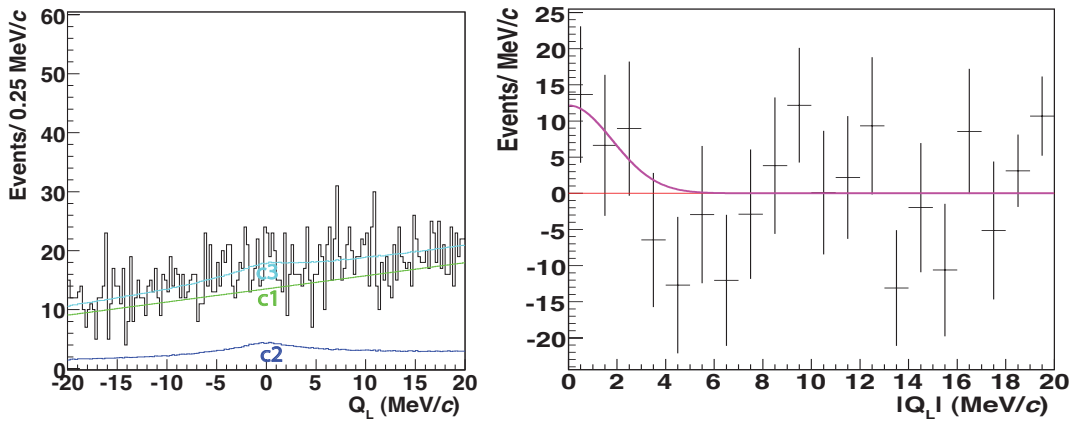

(a) (b)

Figure 6.16: (a): Q_L π^+K^- distribution for the Pt-28 μm data (black histogram) and the fitted background for non-Coulomb in green (c1) and for Coulomb-pairs in blue (c2). The total background is plotted in turquoise (c3). The excess of data for low Q_L is the signal. (b): Residuals of the data and the fitted background contribution. A Gaussian fit has been applied in pink (solid line).

in the second line of table 6.2. A difference between the number of π^-K^+ and π^+K^--atoms is expected due to different K^+ and K^- production rates.

6.5 $\pi^-K^+ + \pi^+K^-$ analysis and mean life measurement

The signal from the π^-K^+ and π^+K^- data samples are added into one histogram (fig. 6.17). From the residuals one obtains

$$A_{\pi^-K^+ + \pi^+K^-} = 173 \pm 54, \tag{6.4}$$

where $A_{\pi^-K^+ + \pi^+K^-}$ is the total number of detected πK-atoms. This gives a significance of 3.2 σ corresponding to a probability of 0.14% for no signal. One can therefore neglect the hypothesis that this excess comes from statistical fluctuations.

The aim of the 2007 run was the observation of πK-atoms. The statistics are too low to give any precise estimate on the mean life of these πK-atoms. Furthermore, the dense Pt-target was chosen to increase the production of πK atomic-pairs, but the drawback is a very low sensitivity to the mean life (fig. 1.4). Small variations in the measurement of the breakup probability lead to very large errors on the mean life measurement. Since many theoretical calculations need as input for their models the mean life measurement I will nevertheless quote a lower limit.

As for the $\pi\pi$ analysis, the simulated k^{exp} (table 6.1) relates the number of detected Coulomb-pairs in the signal region ($|Q_L| < 3$ MeV/c) to the number of

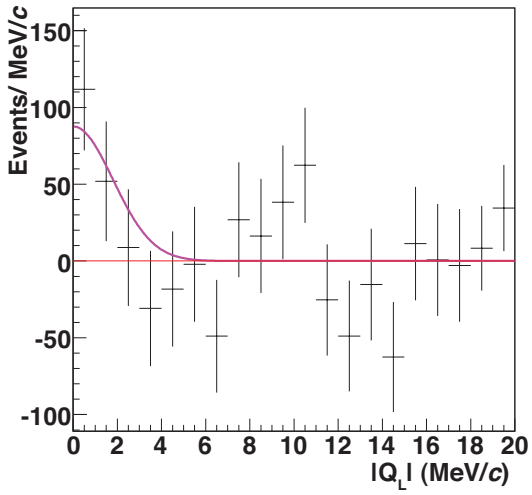

Figure 6.17: Residuals for the π^-K^+ and the π^+K^- data samples. The pink curve (solid line) shows a Gaussian fit.

produced atoms N^A through the following relation:

$$N^A = N^C(|Q_L| < 3 \text{ MeV}/c) \cdot k^{exp}. \tag{6.5}$$

This relation allows to calculate the breakup probability ($P_{br} = n^A/N^A$) for the π^-K^+-atoms and their charge conjugated case. The two measurements are afterwards merged to one using a weighted mean leading to a breakup probability of $(64.2 \pm 25.0)\%$. Results are summarized in table 6.3.

event type	n^A	N^C with $\lvert Q_L\rvert < 3$ MeV/c	P_{br}
π^-K^+	143.2 ± 53.2	972.0 ± 233.2	$(62.0 \pm 27.4)\%$
π^+K^-	29.3 ± 14.8	164.4 ± 108.2	$(75.1 \pm 61.6)\%$
$\pi^-K^+ + \pi^+K^-$	—	—	$(64.2 \pm 25.0)\%$

Table 6.3: Atomic and Coulomb-pairs for $|Q_L| < 3$ MeV/c and their associated breakup probability P_{br}. The last line gives the weighted mean of the two (independent) π^-K^+ and π^+K^- breakup probabilities.

For the πK-atoms the relation between P_{br} and their mean life has been simulated following the procedure described in section 1.3. The result is plotted in fig. 6.18 (solid black curve). The dotted vertical line shows the predicted mean life of πK-atoms [15] and the horizontal one is the corresponding breakup probability. The measured breakup probability from table 6.3 is the horizontal red (solid) line and the 1σ lower limit is the horizontal red (dashed) line, leading to a lower limit on their mean life of:

$$\tau_{1S} \geq 1.5 \text{ fs with a confidence level of } 84.1\%. \tag{6.6}$$

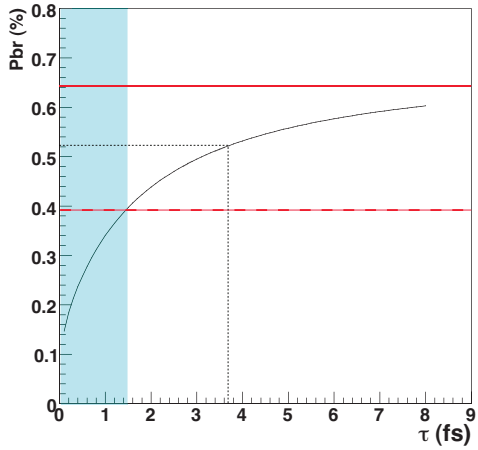

Figure 6.18: Breakup probability P_{br} for a 28 μm Pt-target as a function of the mean life of πK-atoms in 1S state. The red horizontal (solid) line is the measured breakup probability and the red dashed line the 1σ lower bound. The shaded turquoise region is excluded by this analysis. The black dotted lines stand for the theoretical predictions [15].

Let us now check the number of observed atomic-pairs (table 6.2) using theoretical predictions on the mean life. The mean life of πK-atoms has been predicted to be 3.7 ± 0.4 fs [15]. According to fig. 6.18 (dotted black lines) the corresponding breakup probability is 52.5%. Without the use of MC, I extracted 858 ± 247 (313 ± 148) Coulomb-pairs in the signal region for $\pi^- K^+$ ($\pi^+ K^-$) respectively (N^C in table 6.4). According to equ.(6.5), one can use the simulated k^{exp} from table 6.1 to calculate the number of produced atoms (N^A in table 6.4). With the predicted breakup probability of 52.5% one obtains the number of atomic-pairs (fourth column of table 6.4). They are in good agreement with the number of atomic pairs obtained from the minimization of the χ^2 (fifth column of table 6.2). This approach illustrates the consistency of the number of measured atomic-pairs.

event type	N^C with $\lvert Q_L\rvert < 3$ MeV/c	N^A	n^A	n^A (from table 6.2)
$\pi^- K^+$	858 ± 247	198 ± 57	104 ± 30	143 ± 53
$\pi^+ K^-$	313 ± 148	72 ± 34	38 ± 18	29 ± 15

Table 6.4: Number of Coulomb-pairs for $\lvert Q_L\rvert < 3$ MeV/c extracted directly from data and the corresponding number of atomic-pairs for a predicted breakup probability of 52.5%. The last column gives the obtained number of atomic-pairs from table 6.2.

Conclusions

An important upgrade has been performed for the DIRAC-II experiment in order to measure simultaneously the mean life of $\pi\pi$ and πK-atoms. Crucial for this upgrade is the aerogel Čerenkov detector responsible for the separation of kaons and protons in the momentum range between 4 and 8 GeV/c. The requirement from the DIRAC-II experiment, especially the large distance between the PMs and the low index of refraction, induced the need for a novel type of design for Čerenkov detectors. This design introduces a wavelength shifter to avoid absorption and a pyramid design to eliminate a position dependent light collection efficiency. This detector has been developed, built and installed in the DIRAC-II setup in summer 2006. Its performance has been discussed in details in this thesis using Monte-Carlo simulation, cosmic rays and the full setup of the DIRAC-II experiment. Due to the small number of kaons compared to protons, a high rejection efficiency was needed to suppress the background. H1 and H2 were tuned to reject 95% of protons while L1 rejected 90%.

During the 2007 run more than 7'000 $\pi\pi$-atoms were recorded and for the first time 173 ± 54 $\pi^- K^+$ and $\pi^+ K^-$-atoms were observed. For these atoms a lower limit of 1.5 fs has been established with a confidence level of 84.1%. This result is very encouraging for a deeper analysis: a better description by the Monte-Carlo is required and more statistics are needed. In 2008 and 2009 beam will be attributed to the DIRAC-II experiment. During these runs a Ni-target will be used for a better sensitivity to the mean life, since the existence of πK -atoms is clearly established from the results of the 2007 run. In the next years, DIRAC-II should be able to measure the mean life of πK-atoms precisely and hence their πK-scattering lengths difference. This will provide an excellent test of the three flavor ChPT.

Appendix A

Theoretical background

A.1 Theory of scattering

The Hamiltonian describing the non relativistic scattering between two particles A and B may be written as:

$$H = \frac{\vec{P}_A^2}{2m_A} + \frac{\vec{P}_B^2}{2m_B} + V_{AB}, \tag{A.1}$$

where m_A and m_B are the masses of the two particles and $\vec{P}_A = -i\nabla_A$ and $\vec{P}_B = -i\nabla_B$ the momenta operators. Hypothesizing that the potential depends only on the relative position of the two particles, one can rewrite the Hamiltonian in relative coordinates as:

$$H = -\frac{\nabla_R^2}{2M} - \frac{\nabla_r^2}{2\mu} + V(\vec{r}), \tag{A.2}$$

where $M = m_A + m_B$ is the total mass and $\mu = \frac{m_A m_B}{m_A + m_B}$ is the reduced mass. The advantage is that it permits to separate the variables. In the center of mass coordinates, the Schrödinger equation to solve is

$$H\psi(\vec{r}) = E\psi(\vec{r}), \tag{A.3}$$

where

$$H = -\frac{\nabla^2}{2\mu} + V(\vec{r}). \tag{A.4}$$

It can be shown [72], that asymptotically the eigenfunctions $\psi_k^{(+)}(\vec{r})$ have the form,

$$\psi_k^{(+)}(\vec{r}) = \exp ikz + f(\theta)\frac{\exp(ikr)}{r}, \tag{A.5}$$

where $k = \mu v_{lab}$ is the momentum in the center of mass, v_{lab} the velocity in the laboratory. The first term describes the incoming wave and the second one the scattered wave. $f(\theta)$ is the (complex) scattering amplitude.

Using the decomposition of $\exp(ikz)$ in a sum of spherical Bessel functions $j_\ell(kr)$ and Legendre polynoms $P_\ell(\cos\theta)$ it is possible to rewrite $\psi(\vec{r})$ and $f(\theta)$. Using,

$$\exp(ikz) \stackrel{\rho=kr}{=} \exp(i\rho\cos\theta) \equiv \sum_{\ell=0}^{\infty}(2\ell+1)i^\ell j_\ell(\rho)P_\ell(\cos\theta),$$

one can use the approximation for large ρ:

$$j_\ell(\rho) \longrightarrow \frac{\sin\left(\rho - \frac{1}{2}\ell\pi\right)}{\rho} = \frac{\exp(i\rho - i\frac{1}{2}\ell\pi) - \exp(-i\rho + i\frac{1}{2}\ell\pi)}{2i\rho}.$$

Finally, the wave function ψ for the potential $V(\vec{r}) = 0$ is:

$$\begin{aligned}\psi(\rho) &= \exp(ikz) \\ &= \sum_{\ell=0}^{\infty}\frac{(2\ell+1)}{2\rho}i^{\ell-1}\Big[\underbrace{\exp(i\rho - i\frac{1}{2}\ell\pi)}_{out} - \underbrace{\exp(i\frac{1}{2}\ell\pi - i\rho)}_{in}\Big]P_\ell(\cos\theta). \quad \text{(A.6)}\end{aligned}$$

For $V(\vec{r}) \neq 0$, to describe the elastic scattering, a complex function $\eta_\ell(k)$ with $|\eta_\ell(k)| = 1$ has to be introduced, the scattered solution $\psi_k^{(+)}$ becomes:

$$\psi_k^{(+)}(\rho) = \sum_{\ell=0}^{\infty}\frac{(2\ell+1)}{2\rho}i^{\ell-1}\left[\eta_\ell\exp(i\rho - i\frac{1}{2}\ell\pi) - \exp(i\frac{1}{2}\ell\pi - i\rho)\right]P_\ell(\cos\theta), \quad \text{(A.7)}$$

where $\eta_\ell(k) \equiv \exp(2i\delta_\ell(k))$ with $\delta_\ell(k)$ the corresponding phase shift. Subtracting equ.(A.6) from (A.7) one gets:

$$f(\theta)\frac{\exp(i\rho)}{r} = \psi(\rho) - \exp(ikz) = \sum_{\ell=0}^{\infty}\frac{(2\ell+1)}{2\rho}\underbrace{i^{\ell-1}}_{\exp(i\frac{\pi}{2}(\ell-1))}(\eta_\ell - 1)\exp(i\rho - i\frac{1}{2}\ell\pi)P_\ell(\cos\theta)$$

and hence

$$f(\theta) = \frac{1}{2ik}\sum_{\ell=0}^{\infty}(2\ell+1)(\exp(2i\delta_\ell) - 1)P_\ell(\cos\theta). \quad \text{(A.8)}$$

A.2 Scattering length a

The scattering length a is defined by the distance r at which the wave function describing the long distance behavior vanishes, when extrapolated into the potential region, for $k \to 0$. For large r, I showed that (equ.(A.7))

$$\psi_k^{(+)}(\rho) = \frac{1}{2\rho}\sum_{\ell=0}^{\infty}(2\ell+1)i^{\ell-1}\left[\exp(2i\delta_\ell)\exp(i\rho - i\frac{1}{2}\ell\pi) - \exp -(i\rho - i\frac{1}{2}\ell\pi)\right]P_\ell(\cos\theta).$$

For the S-wave ($\ell = 0$) one has $P_{\ell=0}(\cos\theta) \equiv 1$ and

$$\begin{aligned}\psi^{(+)}_{k,\ell=0}(\rho) &= \frac{1}{2\rho i}\exp(2i\delta_0)\left(\exp(i\rho) - \exp(-i\rho)\right) \\ &= \frac{\exp(i\delta_0)}{\rho}\frac{\exp(i\rho + i\delta_0) - \exp(-(i\rho + i\delta_0))}{2i} \\ &= \frac{\exp(i\delta_0)}{\rho}\sin(\rho + \delta_0). \end{aligned} \tag{A.9}$$

By definition, the scattering length a is defined as the distance r for which,

$$\sin(kr + \delta_0) \equiv 0 \tag{A.10}$$

While

$$\sin(kr + \delta_0) = \sin(kr)\cos(\delta_0) + \cos(kr)\sin(\delta_0) = 0,$$

the scattering length a is therefore given by

$$ka\cot\delta_0 + 1 = 0. \tag{A.11}$$

For small values of δ_0 one can use the following approximation

$$\delta_0 \simeq -ka. \tag{A.12}$$

Therefore a is the slope of $\delta_0(k)$ at $k = 0$. Furthermore, for $\ell = 0$ according to equ.(A.13), the scattering amplitude becomes

$$f(\theta) = \frac{1}{k}\left(\frac{\exp(2i\delta_0) - 1}{2i}\right) \simeq \frac{1}{k}\delta_0 = -a.^1 \tag{A.13}$$

A.3 Transition probability and cross section

The transition probability between the states k and k' is given by Fermi's Golden Rule:

$$w(\vec{k}, \vec{k'}) = 2\pi|U(k, k')|^2\frac{dN}{dE}, \tag{A.14}$$

where

$$U(k, k') = \frac{1}{\tau}\int[\exp ikr]^* V(\vec{r})\psi^{(+)}_{\vec{k'}}(\vec{r})d\tau \tag{A.15}$$

and $\tau = L^3$, the 3 dimensional space on which the wave function is normalized, and L is the periodicity of the wave function.

One can now evaluate the density of states $\frac{dN}{dE}$ between E and $E + dE$. Details are given in [73]. Basically, a free particle with plane wave function $\exp ikr$ and periodicity L requires

$$k_x = 2\pi\frac{n_x}{L} \qquad k_y = 2\pi\frac{n_y}{L} \qquad k_z = 2\pi\frac{n_z}{L} \tag{A.16}$$

[1] By convention in high energy physics $f(\theta) = +a$.

where n_x, n_y and n_z are a set of integer, which one can constrain by the relation,

$$n_x^2 + n_y^2 + n_z^2 < n^2. \tag{A.17}$$

Using the last constraint and relation (A.16) one can describe the number of states $N(n)$ as

$$N(n) = \frac{1}{3} n^3 d\Omega = \frac{1}{3} \frac{\tau}{(2\pi)^3} k^3 d\Omega, \tag{A.18}$$

where the value of k corresponds to the limit n.

For free particles with energy in the center of mass $E = k^2/2\mu$, one obtains finally the density of states:

$$\frac{dN}{dE}(E) = \frac{dN}{dk}\frac{dk}{dE} = \frac{\tau\mu}{(2\pi)^3} k d\Omega, \tag{A.19}$$

and one can rewrite the transition probability $w(k, k')$ (equ.(A.14)), as

$$w(k, k') = \frac{\tau\mu}{(2\pi)^2} k |U(k, k')|^2. \tag{A.20}$$

The differential scattering cross section can be evaluated now. By definition, the cross section is given by the relation,

$$d\sigma = \frac{w}{i_i}, \tag{A.21}$$

where i_i is the density of current or the number of incoming particles per unit of time and area. We have seen that the plane wave occupies a volume τ. Hence the incoming particle density is $\tau^{-1} |\exp ikr|^2 = \tau^{-1}$ and the density of current i_i is τ^{-1} multiplied by the velocity $v_i = k/\mu$. Together with equ.(A.21) the cross section can be written as

$$d\sigma = \left(\frac{\mu\tau}{2\pi}\right)^2 |U|^2 d\Omega, \tag{A.22}$$

or the differential scattering cross section $\frac{d\sigma}{d\Omega}$ can be written as

$$\frac{d\sigma}{d\Omega} = \left(\frac{\mu\tau}{2\pi}\right)^2 |U|^2. \tag{A.23}$$

Before calculating a relation for $|U|^2$, let us derive one of the most important equation, relating the differential cross section and the scattering amplitude $f(\theta)$. To do so, let us write an expression relating the i_i the incoming density of current and i_f the outgoing density of current:

$$i_i = v_i \frac{1}{\tau} |\exp(ikz)|^2 = \frac{v_i}{\tau} \tag{A.24}$$

$$i_f = v_f \frac{1}{\tau} \left| \frac{f(\theta)|^2}{r^2} \exp(ikr) \right| = v_f \frac{1}{\tau} |f(\theta)|^2 \frac{1}{r^2}, \tag{A.25}$$

where v_i is the velocity of the incoming particles and v_f of the outgoing particles. Since the scattering is elastic, $v_i = v_f$, and:

$$i_f = \frac{|f(\theta)|}{r^2} i_i. \tag{A.26}$$

Finally, from the definition (A.21) and equ. (A.26) one gets:

$$\begin{aligned} w &= d\Omega i_i \frac{d\sigma}{d\Omega} = i_f r^2 d\Omega = i_i |f(\theta)|^2 d\Omega \\ &\Rightarrow |f(\theta)|^2 = \frac{d\sigma}{d\Omega}. \end{aligned} \tag{A.27}$$

Using this last equation together with relation (A.13) it is possible to relate the scattering length to the total cross section:

$$\sigma_{total} = 4\pi a^2. \tag{A.28}$$

A last important property is the so called optical theorem. Based on the conservation of the current in a region without source or absorber, one can show that

$$\sigma = \frac{4\pi}{k} \mathrm{Im} f(0). \tag{A.29}$$

For a demonstration see [73], [74], [72].

A.4 $|U|^2$ and the Born approximation

The difficult task is to obtain a solution for $|U|^2$ given by equation (A.15). One way is to use the Born approximation. It assumes that if the wave function of the incident particle is weakly perturbed by the potential, one can replace the outgoing wave function (A.5) by the unperturbed plane wave function. This kind of approximation is also known as first order perturbation theory. A discussion on the validity of this approximation is given in [73], section 9.4. Using this approximation, U becomes

$$U = \frac{1}{\tau} \int [\exp ikr]^* V(\vec{r}) \exp ik'r d\tau. \tag{A.30}$$

From expression (A.27) and (A.23), one obtains

$$\begin{aligned} |f(\theta)|^2 = \frac{d\sigma}{d\Omega} &= \frac{w}{i_i} = \frac{w\tau}{v_i} \\ &= \frac{\tau^2 k^2}{4\pi^2 v_i^2} |\frac{1}{\tau} \int V(r) \exp(i \underbrace{(\vec{k} - \vec{k'})}_{\vec{q}} \vec{r})|^2 \\ &= \frac{\tau^2 k^2}{4\pi^2 v_i^2} |\frac{1}{\tau} \int_0^\infty V(r) \frac{\sin(qr)}{qr} 4\pi r^2 dr|^2, \end{aligned} \tag{A.31}$$

where the last equality has been obtained using the decomposition in Bessel functions derived in the last subsection.

An approximation is to consider the nuclear potential V constant inside a sphere of radius R_0 while vanishing outside,

$$\begin{aligned} V(r) &\equiv V_0 \quad \text{if} \quad r < R_0 \\ V(r) &\equiv 0 \quad \text{if} \quad r > R_0 \end{aligned} \tag{A.32}$$

Introducing the potential defined by (A.32) in equation (A.31), one obtains,

$$\begin{aligned} f(\theta) &= \frac{\mu}{2\pi}\int_0^{R_0} V_0 4\pi r \sin(qr) dr \overset{r \text{ small}}{\simeq} \frac{\mu}{2\pi}\int_0^{R_0} V_0 4\pi q r^2 dr \\ &\simeq -\frac{2\mu V_0}{3} R_0^3 \simeq -a. \end{aligned} \tag{A.33}$$

This leads to an expression for V_0:

$$V_0 = \frac{3a}{2\mu R_0^3}. \tag{A.34}$$

A.5 πK-atoms

Let us now consider a bound state composed of a pion and a kaon. The free plane wave function has to be replaced by the atomic wave function. Using the square potential as a perturbation to the Coulomb potential, one gets in first order

$$\Delta E = \langle 0|V|0\rangle = -\int_0^{R_0} |\overbrace{\psi(r)}^{\text{atomic wave function}}|^2 V_0 d\tau \simeq -|\psi(0)|^2 V_0 4\pi \frac{R_0^3}{3}. \tag{A.35}$$

With the approximation $|\psi(0)|^2 = \frac{\mu^2\alpha^3}{\pi}$ and equ. (A.34) one gets

$$\Delta E = -2\mu^2\alpha^3 a. \tag{A.36}$$

Since the atom decays into $K^\pm$, $\pi^\mp$, the energy shift must be complex $\Delta E = E - E_0 - i\frac{\Gamma}{2}$. The relation between the mean life τ and the scattering length is

$$\tau \equiv \frac{1}{\Gamma} = -\frac{1}{\mathrm{Im}\Delta E} = \frac{1}{2\mu^2\alpha^3}(\mathrm{Im}a)^{-1}. \tag{A.37}$$

A.6 Isospin

The interaction between the pion and the kaon conserves the isospin. The transition matrix element $\langle \pi^0 K^0|T|\pi^\pm K^\mp\rangle$ may be decomposed into the respective isospins. The pions are defined as isospin triplet,

$$\pi^+ = |1\ 1\rangle \tag{A.38}$$

$$\pi^0 = |1\ 0\rangle \tag{A.39}$$

$$\pi^- = |1\ -1\rangle. \tag{A.40}$$

The charged kaons are defined as isospin doublet,

$$K^+ = |\frac{1}{2}\ \frac{1}{2}\rangle, \tag{A.41}$$

$$K^0 = |\frac{1}{2}\ -\frac{1}{2}\rangle \tag{A.42}$$

and

$$K^- = |\frac{1}{2}\ \frac{1}{2}\rangle, \tag{A.43}$$

$$\overline{K}^0 = |\frac{1}{2}\ -\frac{1}{2}\rangle. \tag{A.44}$$

To build the combined isospin state $|\pi^0 K^0\rangle$ and $|\pi^\pm K^\mp\rangle$ one can use the Clebsch-Gordan coefficient [75],

$$|\pi^0 k^0\rangle = \sqrt{\frac{2}{3}}|\frac{3}{2}\rangle - \sqrt{\frac{1}{3}}|\frac{1}{2}\rangle, \tag{A.45}$$

$$|\pi^\pm K^\mp\rangle = \sqrt{\frac{1}{3}}|\frac{3}{2}\rangle + \sqrt{\frac{2}{3}}|\frac{1}{2}\rangle. \tag{A.46}$$

Taken in account only the isospin part of the wave-function, the transition matrix element can be written as

$$\begin{aligned}\langle\pi^0 K^0|T|\pi^\pm K^\mp\rangle &= \left(\sqrt{\frac{2}{3}}\langle\frac{3}{2}| - \sqrt{\frac{1}{3}}\langle\frac{1}{2}|\right)\cdot T\cdot\left(\sqrt{\frac{1}{3}}|\frac{3}{2}\rangle + \sqrt{\frac{2}{3}}|\frac{1}{2}\rangle\right)\\ &= \frac{\sqrt{2}}{3}\left(\langle\frac{3}{2}|T|\frac{3}{2}\rangle - \langle\frac{1}{2}|T|\frac{1}{2}\rangle\right).\end{aligned} \tag{A.47}$$

To relate the scattering length to the isospin dependent scattering length, one uses the optical theorem (A.29) and relation (A.13),

$$\sigma_{total} = \frac{4\pi}{p*}\mathrm{Im}f(0) = \frac{4\pi}{p*}\mathrm{Im}a, \tag{A.48}$$

where σ_{total} is the total cross section and $p*$ the relative momentum. Using equation (A.28) and the isospin decomposition, one obtains

$$\mathrm{Im}a = p^*\frac{2}{9}(a_3 - a_1)^2. \tag{A.49}$$

Finally, one gets DIRAC's main relation: the scattering length is related to the mean life which can be measured by the experiment,

$$\Gamma = \frac{1}{\tau} = \frac{8}{9}p^*\mu^2\alpha^3|a_3 - a_1|^2(1+\delta_\Gamma), \tag{A.50}$$

where δ_Γ is the correction term. This has been calculated [15] and is in the order of $(4\pm 2)\%$. Also, for the energy shift one gets,

$$\mathrm{Re}\Delta E = -2\mu^2\alpha^3\frac{1}{3}(a_3 + 2a_1). \tag{A.51}$$

More information on scattering theory is given in [76].

Appendix B

PM specifications

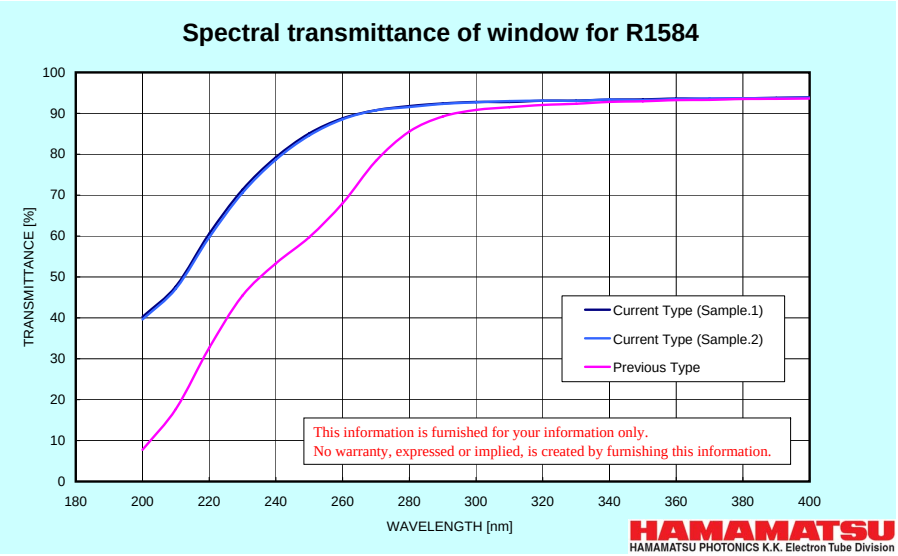

Figure B.1: Transmittance of the photocathode as a function of the wavelength for the new and the old versions of the photomultiplier R1584.

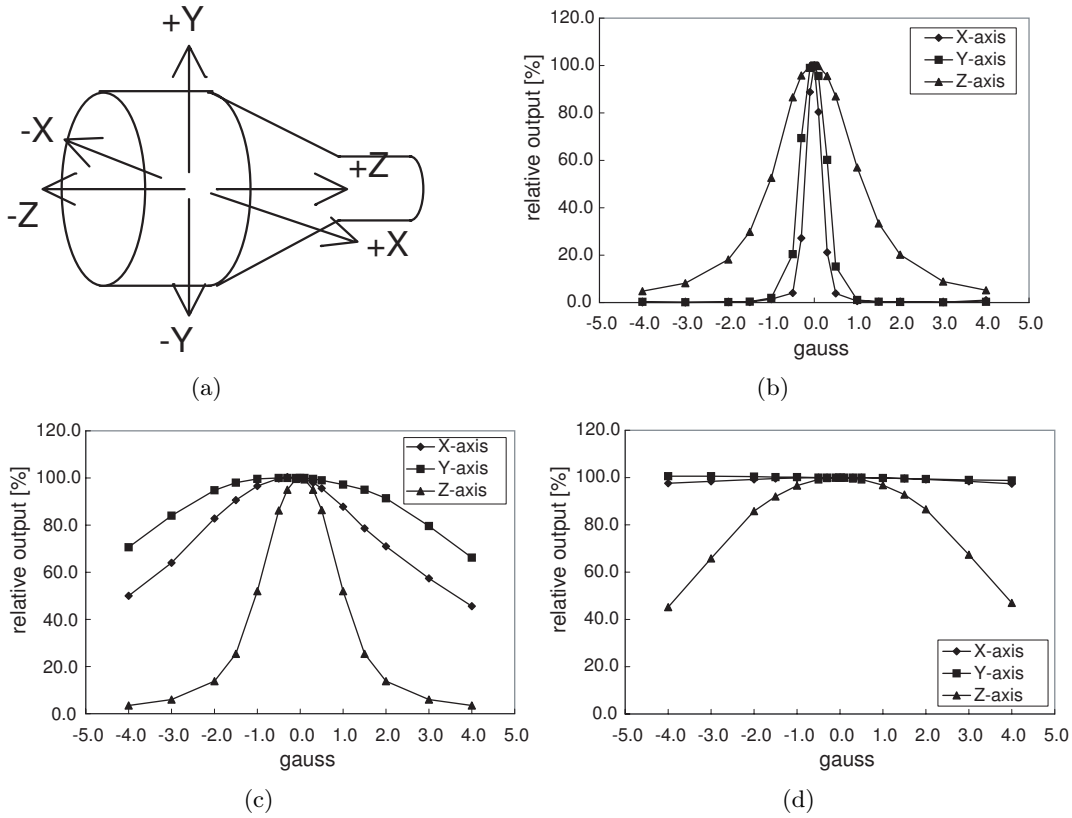

Figure B.2: (a): Influence of the external magnetic field on the output signal of the PMs for each direction of the system of coordinate defined in (a): Relative output as a function of the external magnetic field without any shielding (b), with a thin μ-metal shielding from Hamamatsu (c) and with an additional shielding also provided by Hamamatsu (d).

Appendix C

Mechanical structure of the aerogel Čerenkov counter

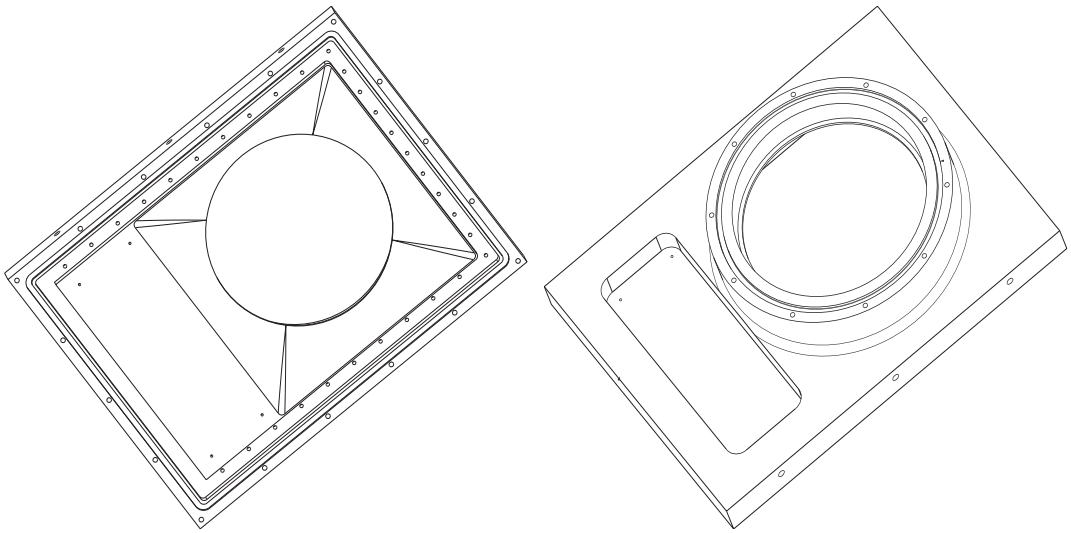

(a) (b)

Figure C.1: Inner (a) and outer (b) view of the main support for the light aerogel module.

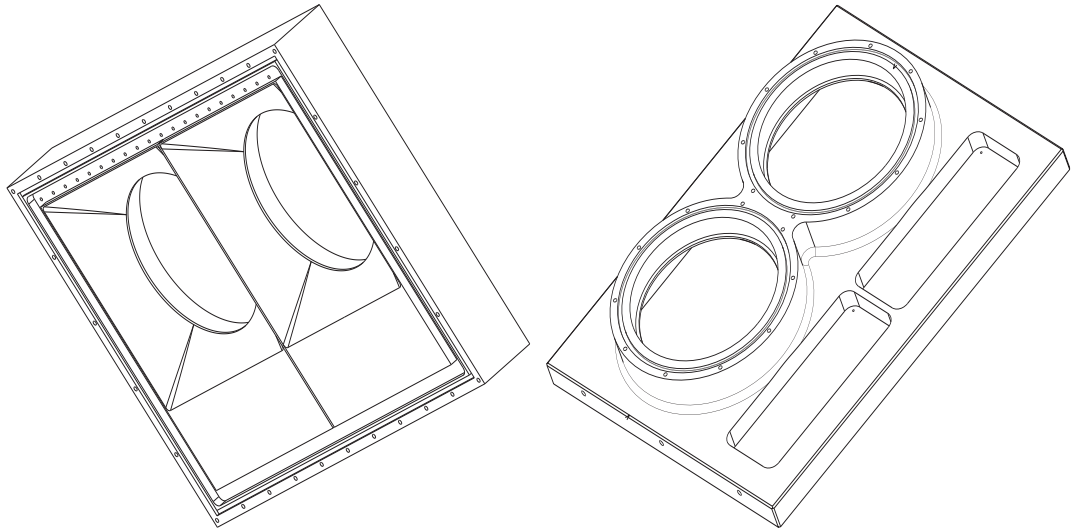

(a) (b)

Figure C.2: Inner (a) and outer view (b) of the main support for the two heavy aerogel modules H1 and H2.

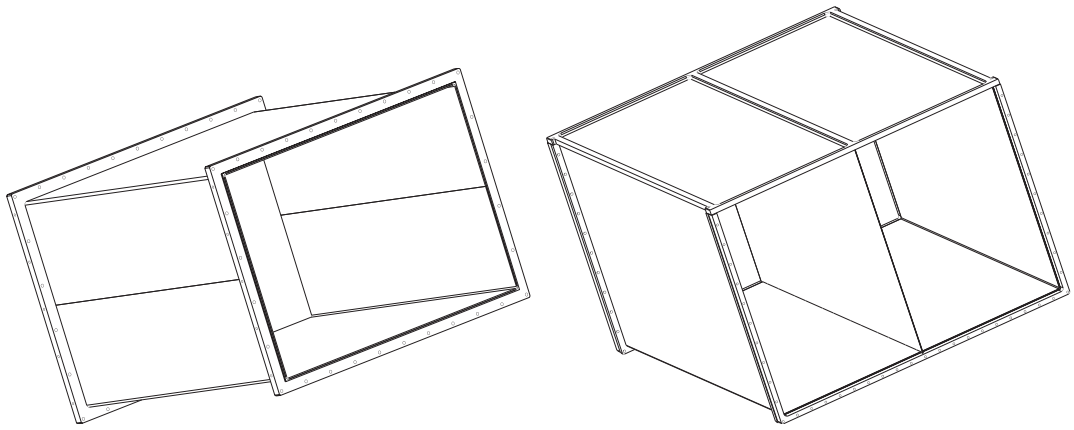

(a) (b)

Figure C.3: Isometric view of the external box (a) and the internal one (b) for the two heavy aerogel modules H1 and H2.

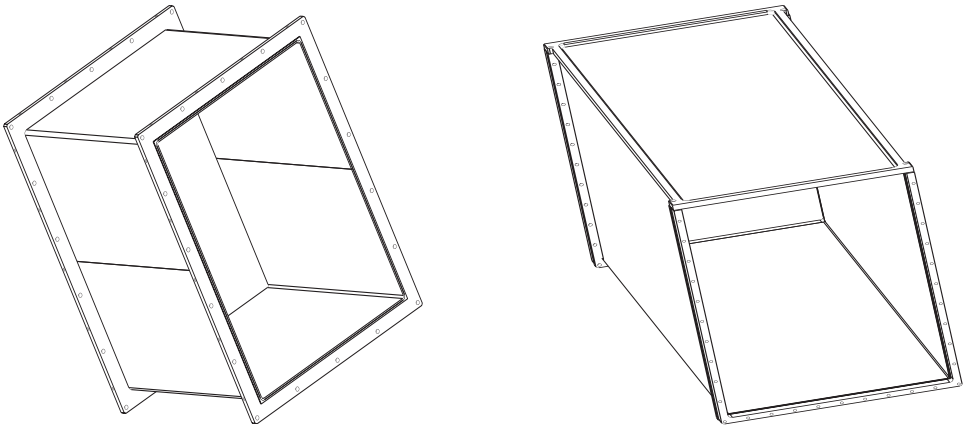

(a) (b)

Figure C.4: Isometric view of the external box (a) and the internal one (b) for the light aerogel module L1.

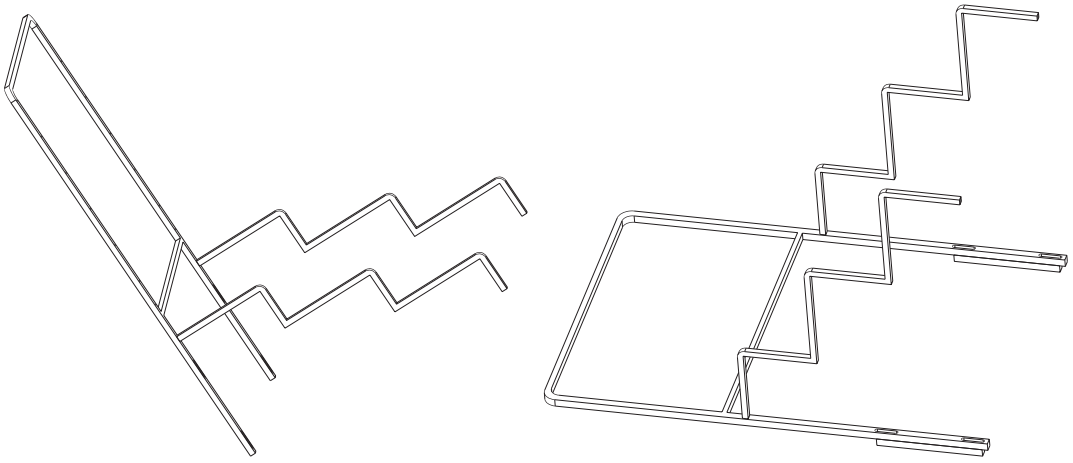

(a) (b)

Figure C.5: Isometric view of the aerogel support for light aerogel module L1 (a) and for the heavy aerogel modules H1, H2 (b).

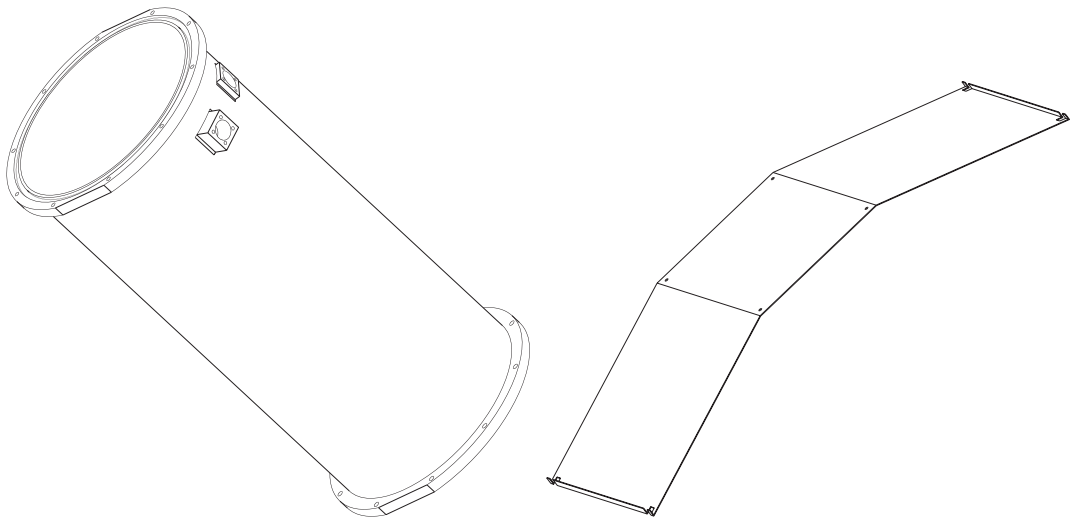

(a) (b)

Figure C.6: Isometric view of the magnetic shielding around the PMs (a) and the reflector covering the pyramid of aerogel (b).

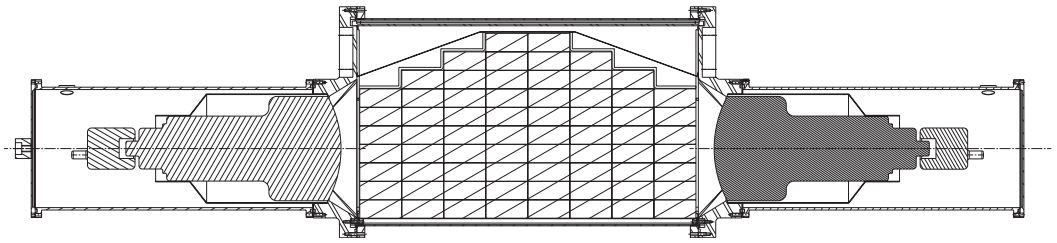

Figure C.7: Isometric view of the aerogel holder of the light aerogel module.

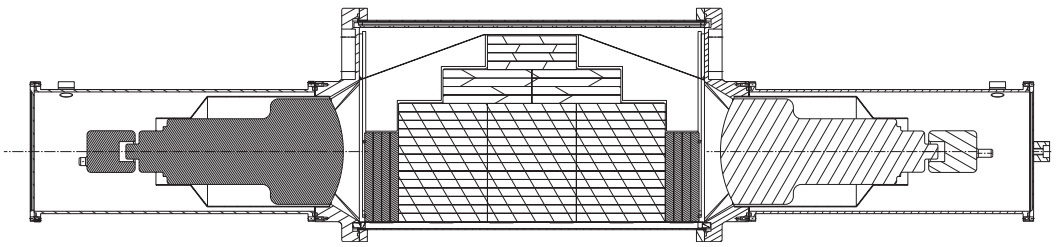

Figure C.8: Isometric view of the aerogel holder of one of the two heavy aerogel modules.

Bibliography

[1] DIRAC collaboration, Phys. Lett. **B 619** (2005) 50

[2] G. Colangelo, J. Gasser, H. Leutwyler, Nucl. Phys. **B 603** (2001)125

[3] DIRAC collaboration, "Lifetime measurement of $\pi^+\pi^-$ and $\pi^\pm K^\mp$ atoms to test low energy QCD", CERN-SPSc-2004-009 (April 2004)

[4] Christian Peter Schütz, "Measurement of the breakup probability of $\pi^+\pi^-$ atoms in a Nickel target with the DIRAC spectrometer", thesis Universität Basel (2004)

[5] Daniel Goldin, "Measurement of $\pi^+\pi^-$ Bound State Lifetime with the DIRAC Spectrometer at CERN", thesis Universität Basel (2005)

[6] Y. Allkofer *et al.*, Nucl. Instr. Meth. **A 582** (2007) 497

[7] Y. Allkofer *et al.*, Frascati Physics Series Vol. XLVI (2008) in print

[8] Y. Allkofer *et al.*, Nucl. Instr. Meth. **A 585** (2008) 84

[9] G. Colangelo and G. Isidori, hep-ph/0101264 v1, (2001)

[10] L. G. Afanasyev *et al.*, Phys. Lett. **B 308** (1993) 200

[11] H. W. Hammer *et al.*, Eur. Phys. J. **A 6** (1999) 115

[12] J. Gasser *et al.*,Phy. Rev. **D 64** (2001) 016008

[13] V. Bernard, N. Kaiser and U. Meissner, Nucl. Phys. **B 357** (1991) 129

[14] P. Buttiker, S. Descotes-Genon and B. Moussalam, Eur. Phys J. **C 33** (2004) 409

[15] J. Schweizer, Phys. Lett. **B 587** (2004) 33

[16] L. Nemenov *et al.*, Nucl. Phys. **A 710** (2002) 303

[17] H. H. Bingham *et al.*, Nucl. Phys. **B 41** (1972) 1

[18] M. J. Matison *et al.*, Phys. Rev. **D 9** (1974) 1872

[19] G. C. Fox and M. L. Griss, Nucl. Phys. **B 80** (1974) 403

[20] P. Estabrooks *et al.*Nucl. Phys. **B 133** (1978) 490

[21] A. M. Bakker *et al.*, Nucl. Phys. **B 24** (1970) 211

[22] Y. Cho *et al.*, Phys. Lett. **B 32** (1970) 237

[23] P. Antich *et al.*, Nucl. Phys. **B 29** (1971) 305

[24] A. R. Kirschbaum *et al.*, Phys. Rev. **D 4** (1971) 3254

[25] B. Jongejans *et al.*, Nucl. Phys. **B 67** (1973) 381

[26] BES collaboration, Phys. Lett. **B 633** (2006) 681

[27] L. Edera, M.R. Pennington, Phys. Lett. **B 623** (2005)55

[28] FOCUS collaboration, Phys. Lett. **B 535** (2002) 43

[29] C. Amsler *et al.* (Particle Data Group) Phys. Lett. **B 667** (2008) 1

[30] CLEO collaboration, Phys. Rev. **D 63** (2001) 092001

[31] R. L. Jaffe, Phys. Rev. **D 15** (1977) 267

[32] V. G. Grishin, "Inclusive processes in hadron interaction at high energy", Energoizdat, (1982) Moscow, 131

[33] L. Nemenov, Yad. Fiz. 41, (1985) 980; Sov. J. Nucl. Phys. **41** (1985) 629

[34] A. D. Sakharov, Zh. Eksp. Teor. Fiz. **18** (1948) 631

[35] L. G. Afanasyev *et al.*, Communication JINR P1-97-306, Dubna,1997

[36] L. G. Afanasyev and O. Voskresenskaya, Phys. Lett. **B 453** (1999) 302

[37] L. G. Afanasyev *et al.*,J. Phys. **G 25** (1999) B7

[38] L. G. Afanasyev and A. V. Tarasov, Phys. At. Nucl. **59** (1996) 2130

[39] Y. Allkofer *et al.*, Nucl. Instr. Meth. **A 585** (2008) 212

[40] M. Zhabitsky, "DIPGEN (DIRAC Pairs Generator)", DIRAC internal note 2007-11

[41] A. Lopez-Agüera and T. Nunez, "Full GEANT simulation for the DIRAC experiment: Trigger rates, detector rates and multiplicities", DIRAC internal note 1997-08

[42] http://zrelov.home.cern.ch/zrelov/dirac/montecarlo/instruction/instruct26.html

[43] http://dirac.web.cern.ch/DIRAC/offlinedocs/SimulData.html

[44] http://dirac.web.cern.ch/DIRAC/offlinedocs/Userguide.html

[45] M. S. Curie, "Radioactivité II", Hermann, page 345 (1935)

[46] P. Čerenkov, Phys. Rev. **52** (1937) 387

[47] I. M. Frank and I. J. Tamm, Dokl. Academy of Science URSS 14 (1937) 107

[48] LHCb collaboration, Nucl. Instr. Meth. **A 563** (2006) 326

[49] BELLE collaboration, Nucl. Instr. Meth. **A 408** (1998) 64

[50] HERMES collaboration, Nucl. Instr. Meth. **A 553** (2005) 205

[51] M. Ishino *et al.*, Nucl. Instr. and Meth. **A 457** (2001) 581

[52] A. Danilyuk *et al.*, Nucl. Instr. and Meth. **A 379** (1996) 465

[53] M. Yu. Barnyakov *et al.*,Nucl. Instr. Meth. **A 453** (2000) 326

[54] C. Amsler *et al.* (Particle Data Group), Phys. Lett. **B 667** (2008) 1

[55] A. Buzykaev et al, Nucl. Instr. and Meth. **A 379** (1996) 453

[56] E. A. Kravchenko *et al.*, Nucl. Instr. and Meth. **A 433** (1999) 396

[57] E. Kistenev, Nucl. Instr. and Meth. **A 518** (2004) 593

[58] S. Agostinelli *et al.*, Nucl. Instr. and Meth. **A 506** (2003) 341, http://geant4.web.cern.ch/geant4/

[59] O. Gorchakov, "Space and momentum distributions of pions and kaons from $A_{\pi^+K^-}$", DIRAC internal note, 2005-05

[60] HAMAMATSU PHOTONICS K.K., 325-6, Sunayama-cho, Hamamatsu City, Shizuoka Pref. 430-8587, Japan, http://www.hamamatsu.com/

[61] PHOTONIS SAS, Avenue Roger RONCIER, BP 520, 19106 BRIVE Cedex, France, http://www.photonis.com/

[62] Starna Brand, "Reference Materials for Molecular Fluorescence Spectroscopy", Optiglass Ltd.

[63] S. Hayakawa, Cosmic Ray Physics, (Wiley, New York, 1969), Monographs and Tests in Physics and Astronomy, Vol. XXII

[64] T. Eichten, D. Haidt, Nucl. Phys. **B 44** (1972) 333

[65] A. Deur, “Knock-on of δ-electrons in Hall A electron arm. Effect of aerogel Čerenkov.", Laboratoire de Physique corpusculaire de Clermont-Ferrand PCCF RI 9912 (1999)

[66] M. Zhabitsky, “Parametrization of single particle spectra at the DIRAC kinematic range", DIRAC internal note 2006-06

[67] Y. Allkofer,, A. Benelli, L. Tauscher, “Angular resolution and multiple scattering in downstream' tracking", DIRAC internal note 2007-09

[68] Y. Allkofer,, A. Benelli, L. Tauscher, “Tracking in DIRAC using only downstream detectors", DIRAC internal note 2007-08

[69] MINUIT, http://wwwasdoc.web.cern.ch/wwwasdoc/minuit/minmain.html

[70] O. Gortchakov, “The Lambda peak width difference of Monte Carlo and real data is the one of sources of systematic error", DIRAC internal note 2007-17

[71] C. Santamarina, C. Schuetz, “Determination of the experimental k factor", DIRAC internal note 2003-09

[72] E. Merzbacher, “Quantum mechanics", John Wiley & Sons, New York, London (1961)

[73] D. Parker, “Introduction to quantum theory", McGraw-Hill book company, New York, San Francisco, Toronto, London (1964)

[74] R. M. Thaler and L. S. Rodberg , “Introduction to the quantum theory of scattering" , Academic Press, New York, London (1967)

[75] C. Cohen-Tannoudji, B. Diu and F. Laloë, “Mécanique quantique 1", Hermann, Paris (1971)

[76] W. S. C. Williams, “An introduction to elementary particles" , Academic press 2nd edition, New York, London (1971)